TÉCNICO LISBOA

Study of Polymer-Metal Adhesion Mechanisms in Fused Filament Fabrication Process

Guilherme Alberto da Cunha Martins

Thesis to obtain the Master of Science Degree in

Mechanical Engineering

Supervisor(s): Prof. Marco Alexandre de Oliveira Leite
Prof. Carlos Miguel Santos Vicente

Examination Committee

Chairperson: Prof. Luís Filipe Galrão dos Reis
Supervisor: Prof. Marco Alexandre De Oliveira Leite
Member of the Committee: Prof. Bruno Alexandre Rodrigues Simões Soares

September 2021

Acknowledgments

Em primeiro lugar, quero agradecer ao Professor Marco Leite e ao Professor Carlos Vicente por todo o apoio e orientação ao longo desta dissertação. Aproveito também para agradecer aos restantes professores envolvidos nos projetos do Laboratório para Desenvolvimento do Produto, Lab2Prod, por toda a disponibilidade e apoio demonstrado ao longo do trabalho experimental.

Destaco o apoio dado pelos meus colegas João Ajuda, Manuel Sardinha e Samuel Magalhães, sempre disponíveis para todas as dificuldades encontradas em contexto laboratorial, para além da companhia que foram no decorrer deste trabalho.

Aos que Lisboa uniu para a vida: Afonso, Bruno, João e Luís, a vossa bonita amizade trouxe-me aqui.

Bernardo, Gonçalo, João, Leandro, Rodrigo e Simão, à vossa paciência e amizade de sempre nesta jornada longe de casa.

À minha Mónica, um profundo agradecimento. Foste quem mais me ajudou a fechar este ciclo e és quem me incentiva sempre a ser uma pessoa melhor.

Termino com uma nota de carinho aos meus pais, Graça e José, e ao meu irmão, Francisco. São as fundações da pessoa que hoje sou.

Este projeto foi apoiado pela FCT, através do IDMEC, sob LAETA, projeto UIDB/50022/2020. O autor reconhece com gratidão o financiamento do projeto BIG FDM, referência FCT PTDC/EME–EME/32103/2017.

Resumo

As técnicas de Fabrico Aditivo (AM) estabeleceram o seu papel no fabrico de estruturas complexas, suplantando os protótipos e componentes mais simples anteriormente fabricados. O desenvolvimento de produtos mais sustentáveis inclui o uso de materiais compósitos e, dentro destes, os Híbridos Metal/Polímero (PMH) lideram pela facilidade de manufatura e melhores características mecânicas. Assim, este trabalho pretende estudar os mecanismos de aderência entre componentes metálicos e poliméricos, fabricados através da Deposição de Filamento Fundido (FFF). Juntas sobrepostas simples com dois aderentes diferentes: um substrato de base metálica e outro de topo polimérico, foram fabricadas e testadas através de perfilometria óptica, Microscopia Eletrónica de Varrimento (SEM), Espectroscopia de raios X por Energia Dispersiva (EDS) e testes mecânicos. A perfilometria óptica revelou mais irregularidades nas superfícies sem tratamento e granalhadas comparativamente às desgastadas com a lixa P120, enquanto a granalhagem demonstrou níveis de abrasão superiores. Para a caracterização mecânica das juntas, cinco provetes de teste foram produzidos e tracionados para cada par metal/polímero. As curvas Tensão de Corte-Deslocamento demonstram a influência da rugosidade e a existência de fibras na força de aderência, demonstrado pelos valores mais elevados obtidos para o par Alumínio-Nylon CF15. Apesar da indefinição acerca da teoria de aderência que explica o comportamento entre estes materiais, a sua melhoria é clara após o tratamento de superfície. A importância das fibras nos mecanismos de aderência foi demonstrada e a fabricação de juntas PMH através de FFF validada.

Palavras-chave: Deposição de Filamento Fundido, Híbrido Metal/Polímero, Junta Sobreposta Simples, ABS, Nylon, Nylon CF15

Abstract

Additive Manufacturing (AM) technologies began fabricating end-use products instead of the simple parts and prototypes primary produced with it. The development of more sustainable products include the use of multi-materials and, comparing with others, Polymer/Metal Hybrid (PMH) components take the upper hand in manufacture easiness and increased strength-to-weight ratio. Then, this work intends to study the adhesion mechanisms between polymer/metal parts manufactured with Fused Filament Fabrication (FFF). Single-lap joints with two different adherends: a metallic base substrate and a polymeric top substrate were manufactured and tested by optical profilometry measurements, Scanning Electron Microscopy (SEM), Energy Dispersive Spectroscopy's (EDS) analysis and mechanical tests. Optical profilometry revealed more irregularities in non-abraded and grit blasted surfaces, comparing with those abraded by P120 sandpaper, while grit blasting technique showed higher abrasion's level. For the single-lap joints' mechanical characterization, five specimens of each pair of polymer/metal were manufactured and tensile tests were performed. The shear stress-displacement curves reflect the surface roughness and fibers' influence on adhesion strength, which translates on the higher result values obtained for Nylon CF15 polymer. Despite the phenomenon of adhesion among the list of materials used in this work not being fully elucidated, an enhanced adhesion after abrading the surface of the Aluminium adherend is evident. The importance of fibers in adhesion mechanisms was also demonstrated and the successful fabrication of several PMH joints possible.

Keywords: Fused Filament Fabrication, Polymer/Metal Hybrid Component, Single-Lap Joint, ABS, Nylon, Nylon CF15

Contents

List of Tables

List of Figures

Symbols

E	Young Modulus
f_i, f_{ij}	Tsai-Wu criteria's strength tensors
S	Shear strength
X	Longitudinal strength
Y	Transverse strength

Greek symbols

ϵ	Normal strain
γ	Shear strain
σ	Normal stress
σ_i, σ_{ij}	Stress tensors
τ	Shear stress
θ	Angle of contact

Subscripts

$1, 2, 3$	Principal material coordinates
6	Shear direction
c	Compression
lv	Liquid-vapor
sl	Solid-liquid
sv	Solid-vapor
t	Tension
UTS	Ultimate Tensile Strength
y	Yield

Acronyms

3DP 3D Printing.

ABS Acrylonitrile Butadiene Styrene.

AM Additive Manufacturing.

CAD Computer-Aided Design.

EDS Energy Dispersive Spectroscopy.

EU European Union.

FDM Fused Deposition Modeling.

FFF Fused Filament Fabrication.

IPA Isopropyl Alcohol.

PA Polyamide.

PBF Powder-Bed Fusion.

PET Polyethylene Terephthalate.

PLA Polylactic Acid.

PMH Polymer/Metal Hybrid.

PP Polypropylene.

PPS Polyphenylene Sulphide.

SDM Shaped Deposition Modeling.

SEM Scanning Electron Microscope.

SL Stereolithography.

SLS Selective Laser Sintering.

STL Stereolithography.

ULSS Ultimate Lap Shear Strength.

VH Vickers' Hardness.

Chapter 1

Introduction

1.1 Motivation

Current European policies plan to make European Union's (EU) economy sustainable, decreasing our greenhouse gas emissions by at least 55% below 1990 levels by 2030, creating a path to become climate neutral by 2050 [1]. Europe's new industrial way clearly sets a common goal for every enterprise within EU, where ecology and digital transformation come together towards an enhanced portfolio of European sustainability leading companies [2].

This ever-increasing demand for sustainable and complex components opens a window of opportunity for Additive Manufacturing (AM) technologies [3] that, after decades of improvement, began to fabricate end-use products instead of the simple parts and prototypes primary produced with it [4]. Due to its flexibility in producing different designs easily without increased costs, it arises as an interesting option for many companies worldwide, for improvement of their market share [5]. Indeed, Dumitrescu and Nase [6] stated an estimated potential of $10.8 billion for global 3D Printing (3DP) Industry by 2021. This value follows the "21.2% growth to $11.867 billion" grow in Global 3DP Industry, published in Wohlers Associates' 2020 report [7]. Such data strengthen AM technologies' socioeconomic influence.

The development of more sustainable products include the use of multi-materials, due to its weight saving potential being one of the most important factors in carbon dioxide emission's reduction [8]. However, combining dissimilar materials, such as metals and polymers, still present many challenges for each industry's sector. When these challenges are overthrown, *automotive, power production, aerospace, medical* and many other sectors, may all benefit from this improved technology [9].

Multi-material components, specifically polymer/metal ones, urge to control the new manufacturing industry that still has to come. Comparing with others, polymer/metal components take the upper hand in manufacture's easiness and increased strength-to-weight ratio [10]. Furthermore, the ability to fabricate such parts, added to industry's highly demand for such, come as a strong advantage to some AM technologies [11, 12]. In this context, Fused Filament Fabrication (FFF) is now perceived as one major AM technology platforms for the production of polymer/metal multi-materials components.

1.2 Objectives

The main goal of this thesis is the study of adhesion mechanisms between polymer/metal parts manufactured by Material Extrusion, commonly known as Fused Filament Fabrication (FFF). Our project comes in pursue of recent developments by Falck et al. [13], where a new technique called *AddJoining*,

successfully combines polymer filaments with Aluminium. To pursue this objective, the following tasks are required:

- Surface treatment of the metallic samples with abrasion techniques;
- Creation of a physical apparatus for fixing metallic samples on a 3D printer;
- Optimization of 3DP parameters for each pair of polymer/metal materials;
- Manufacturing of PMH components combined in a single-lap joint;
- Evaluation of the quasi-static mechanical behaviour of multi-materials single-lap joints;
- Assessment of surface treatment and fibers content's effect on adhesion strength;
- Correlate the fracture's surface of the joints with its mechanical behaviour;
- Discuss the applied adhesion techniques and its feasibility for future applications in the context of the FFF technologies.

1.3 Thesis Outline

The present document is structured as follows:

Chapter 1 presents the **Introduction**, which outlines the motivation and the scope of this dissertation.

Chapter 2 is the **Literature Review**, the chapter that introduces all relevant matters investigated in our work. A review of current AM technologies, specifically in the field of dissimilar materials' manufacturing is presented. Theories of adhesion are also discussed, concluding with some remarks about the type of specimens utilized.

Chapter 3 is entailed to describe the **Materials and Methods** applied and followed for the implementation of the experimental work. The methodology and the validation tests employed for the mechanical characterization of our specimens are also provided.

Chapter 4 outlines the **Results and Discussion** of our validation tests.

Chapter 5 sets out the **Conclusions** of this work. It shows the main achievements of this thesis, together with some remarks about future work.

Chapter 2

Literature Review

This section provides an overview about FFF, the AM technique used in this work, pertinent work in the field of adhesion theories and current techniques for joining dissimilar materials. Advances in this field of knowledge are also presented in here, preceding a detailed characterization of all materials employed in the experimental section.

2.1 Fused Filament Fabrication

2.1.1 Historical Remarks

In 1987, *3D Systems* introduced AM technology to the market. The first process of this revolutionary technology to be introduced was Stereolithography (SL), a technique where liquid resin is solidified by photopolymerisation, in order to obtain a 3D object [14]. During the 90's, another breaking AM technology came to life, Selective Laser Sintering (SLS), a faster prototyping process that allows the consumer to create complex 3D parts by solidifying consecutive layers of powder material on top of each other [15].

Among many others that were born during this period of time, the American company *Stratasys* created the trademark Fused Deposition Modeling (FDM), commonly known as Fused Filament Fabrication (FFF) and the technology used in this thesis. This process consists of extruding molten thermoplastic materials in filament form until creating a layer by layer 3D object and is one of the most diverse and resourced AM technologies that exists nowadays [16–19].

Apart from the mentioned above, there are many more AM techniques that were developed and improved over the years and continue to increase its global market share [16].

2.1.2 Process Overview

Similarly to every other AM technique, FFF starts by converting a file from a Computer-Aided Design (CAD) software into a Stereolithography (STL) file, a process often called slicing [20]. The slicing procedure is basically an approximation of each one of the 3D model's surfaces with many small triangular planes, or tessellation [21].

Before describing FFF's process schematic, Figure 2.1, the three main components of a FFF machine must be identified: the filament pulling system (also called the feeder), *cold end*, the heated liquifier, *hot end*, and the *build plate* [22]. This process starts with filament material being guided to the extruder, which uses torque and a pinch system to feed and retract precise amounts of it. A heater block then melts the filament to a controllable temperature, well above the glass transition temperature of amorphous polymers or the melting point of semi-crystalline ones [22, 23], and is forced out of the

heated nozzle with an increased temperature. The extruded material is laid down on the model alongside the correct positioning of the print head and/or build plate, placing the material where it is needed [24, 25].

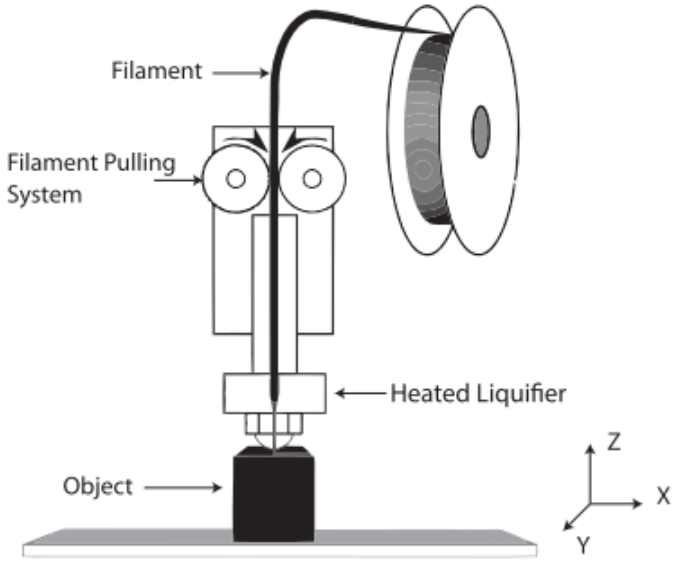

Figure 2.1: FFF process schematic. Adapted from [26].

To obtain complex geometries, a second extruder is required for the support filament material. This support filament material serves as a scaffolding for overhang layers and for complex multi-materials' components, as well [27–29].

2.1.3 Manufacturing Considerations

The utterly value of FFF techniques for rapid prototyping or end-user products is undeniable [30]. Although, it is highly dependent on the optimization of numerous parameters to achieve a high-quality surface finish [31] and a superior mechanical performance, such as, that on injection-molded parts [32]. Build orientation, deposition speed, infill orientation and number of contours are just a few of those that have a direct effect on the surface quality and dimensional accuracy [33–35], adding to the reviewed influence of air gap in the mechanical properties of 3D printed parts [36].

A schematic description of some of these parameters can be seen in Figure 2.2, in which Falck et al. [37] briefly outlines:

- **Raster Angle:** angle between the deposited raster with respect to the x-axis of the build plate;
- **Air Gap:** space between two parallel lines of deposited material;
- **Raster Width:** width of each deposited raster;
- **Raster Thickness:** height of the deposited raster.

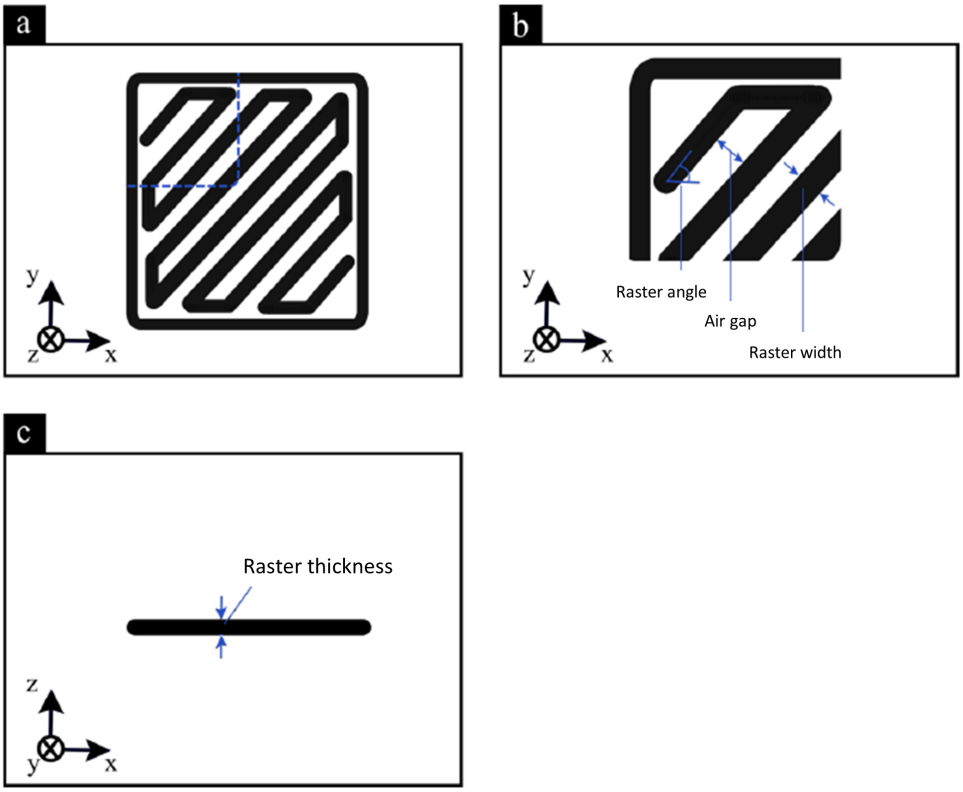

Figure 2.2: Manufacturing parameters' schematic: (a) and (b) - top view, (c) - lateral view. Adapted from [37].

Additionally, previous studies have shown a correlation between each parameter and a high-quality FFF processed part [38–41]. Among many others (some already summarized above), these next four parameters were found crucial for the adhesion promotion between layers (highly important in our study), quality and structural strength of a 3D printed component [37]:

- **Printing Temperature** showed an important relevance in bonding mechanisms between consecutive layers of extruded material. Previous studies have already shown a correlation linking temperature and viscosity of polymers [42], where an increase of temperature resulted in lower viscosity for Acrylonitrile Butadiene Styrene (ABS). Rosenzweig and Narkis [43] add that, this polymer viscous flow behaviour tends to enhance the coalescence of two separate particles of material, when heated above its glass transition temperature. Falck et al. [37] also displayed the decrease of voids in the 3D printed polymeric part with an increase of temperature, leading to stronger bonding between layers [44].

- **Raster Thickness** is the thickness of the deposited layer and depends upon the nozzle type [45]. The same author also proved the impact of raster thickness on the structural strength of the 3D printed object, a thinner raster would result in a significant increase in the strength of the ABS specimen. Wu et al. [46] also found a decline in micro-voids with a narrow layer, which appears to exhibit a preferable bonding strength.

- **Raster Angle** is defined by the direction of the raster relative to the loading vector of the part, and is one of the most important parameter influencing tensile strength of FFF parts [47]. Ahn et al.

[48] also reported an increased tensile strength for the orientation [45º/-45º] and the orientation [0º], along with a more compact part (less voids within the inner structure). Fatimatuzahraa et al. [49] also presented an interesting report comparing the influence of raster orientation in tensile and flexural strength.

- **Number of Contours** is the amount of enclosed toolpaths that create the outer wall of a 3D object [50], Figure 2.3. This parameter is even more pertinent to the structural strength when in line with an optimization of raster angle. Gebisa and Lemu [50] found a positive gradient in tensile strength with the same variation in contour number. This number was found to be highly important for parts subjected to tensile loading and a raster angle orientation [45º/-45º].

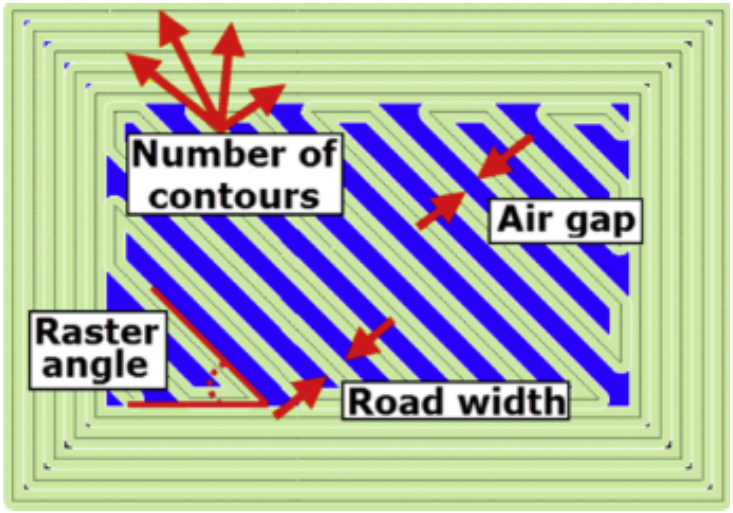

Figure 2.3: Schematic view of some FFF parameters. Adapted from [51].

There is another extremely important parameter, particularly in this thesis, which is the brim. This variable consists of an extension of the first deposited layer by a number of contours to create a large ring surrounding the part (attached to it), increasing the surface area of the first layer and enhancing its adhesion to the build plate surface. After removal of the part, this extra material is detached from it [52, 53].

2.2 Joining Dissimilar Materials

The world is asking for more optimal, lightweight and high performance components. This enhances the need for using multi-materials' components, showing the relevance of joining dissimilar materials [9, 54]. Increasing product's functionality and manufacturing's efficiency is highly demanding. However, it can be achieved with multi-materials' joining techniques [55]. This manufacturing procedure spans over multiple approaches and materials, which can increase its complexity, regarding other manufacturing techniques [56]. Regarding all that, joining of dissimilar materials has already conquered almost every industry. Automotive [57], aeronautics [58], textile [59], tooling [60], among many others [61, 62] found in this manufacturing technique their course of action to create innovative components.

Citing EU Joining Sub-Platform [54], the definition of joining is: "Creating a bond of some description

between materials or components to achieve a specific physical performance." This link can assume many forms and it is produced with one of these three main processes: mechanical, chemical and thermal.

2.3 Adhesion Theories

In this section, it is presented an outline of the theory behind adhesion techniques and an analysis of the relevant parameters when joining dissimilar materials.

Adhesive joining is the most appropriate technique for bonding metallic and non-metallic structures where strength-to-weight ratio must be maximized [63]. This technique utilizes polymeric substrates to join a large variety of material combinations, such as metal-metal, metal-plastic, metal-composite, composite-composite, plastic-plastic, metal-ceramic, among others [64]. Baldan et al. [64] provides an extensive review of adhesive bonding theory in metallic alloys, polymers and composite materials. One of the major setbacks in the polymeric use for adhesive purposes is its service temperature limitation [65], thus swiftly decreasing their mechanical properties at higher temperatures.

Brockmann [66] summarized the possibilities, advantages and disadvantages of adhesive bonding compared to other joining techniques, as illustrated in Table 2.1. For these reasons, the number of adhesive bonding applications in multiple industries continues to rise, benefiting aeronautics [67], railways [68] and automotive's [69], to state a few examples. Citing Brockmann, *"Bonding is by far the most universal joining technique. Virtually all technically useful materials can be joined with each other, and one with another, by means of this surface-to-surface and material-joining technique."*

Table 2.1: Characteristic traits of adhesive joints. Adapted from [66].

Advantages	**Disadvantages**
- The adherents are not affected by heat	- Limited stability to heat
- Uniform stress distribution	- May alter the properties of the bond-line
- Possibility to join large surfaces	- Surface preparation is prime
- Possibility to join different materials	- Specific production requirements to be met
- Possibility to join very thin adherents	- Clamping devices required
- Gas-proof and liquid tight	- Nondestructive quality testing barely nonexistent
- No crevice corrosion	
- No contact corrosion	
- No precise fits of the adherent surfaces are necessary	
- Good damping properties	
- High dynamic strength	

The phenomenon of adhesion occurs when a mechanical work is required to separate two surfaces of different chemical composition or shape [70, 71] and occurs at an interface between the adhesive and adherend, Figure 2.4. For a successful joint, an adhesive must perform two things: wet the surface spreading itself along the adherend and making a contact angle near zero [64, 72]. This combination of events will result in an intimately contact between each substrate, adhesive and adherend.

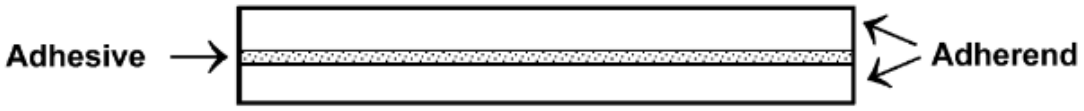

Figure 2.4: Identification of each part of an adhesive bonding. Adapted from [73].

Wetting phenomena are ruled by the intimate contact between adhesive's molecules and the surface and interfacial interations, reacting at short distance (van der Waals nano interactions) and very small scale (molecular interaction) [74]. This intimate contact is achieved across van der Waals forces, along with stronger intermolecular ones, such as primary chemical bonds. Rougher surfaces also allow low viscosity adhesives to flow through those cavities, thus increasing mechanical interlocking between the substrates [75].

Four main theories of adhesion were identified above: physical absorption, chemical bonding, mechanical interlocking and diffusion. Literature adds two more: electrostatic attraction and weak boundary layer theories [76–78], as will be further explained below. Despite the extensive utilization of adhesives, thorough researches have not yet reached a conclusion on which mechanisms best suit adhesive bonding. Hence, a mixture of theories is usually responsible for a given system [79]. Thereby, a particular theory might suit some combination of substrates better in a defined range of parameters, while other is best suited for another.

2.3.1 Absorption Theory

The absorption theory relies on the assumption that, the adhesive completely wets the substrate (creates a continuous interface between the adhesive and the adherend), which forms the adhesive joint. The outcome of this theory was the development of adhesive materials with lower surface tension than that of the adherend [80]. This theory confirms the influence of interatomic and intermolecular forces (van der Waals, dipole-dipole, hydrogen bonds, among others) in the adhesive strength, if the adhesive is perfectly spread on top of the adherend surface.

A schematic example of an adhesive properly spread onto the adherend surface is represented in the bottom of Figure 2.5 (the adhesive material completely filled the cavities of the adherend surface), characteristic of a good wetting, whereas on the top of the same figure, the presence of air voids suggests a poor wetting of the surface, in all likelihood resulting in a weak adhesive joint [81].

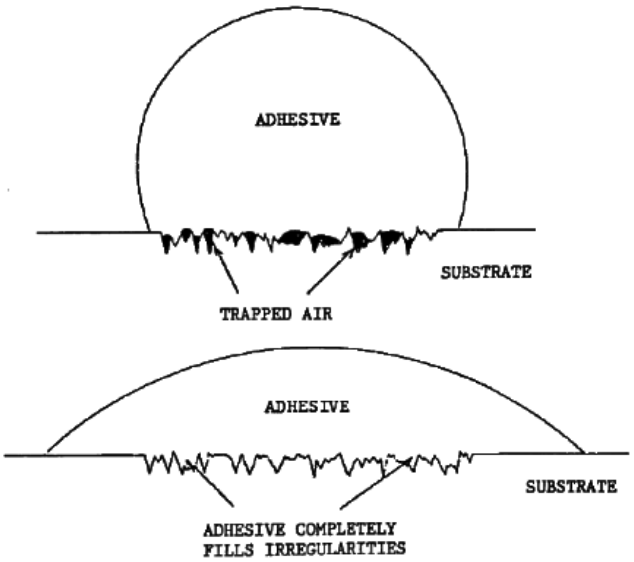

Figure 2.5: Illustration of bad wetting (top) and good wetting (bottom). Adapted from [81].

Another method to evaluate the wettability of a solid by a liquid is through contact angle measurement. Indeed, Young [82] has even demonstrated that there is a fitting angle of contact between the surface of each pair of fluid (adhesive) and solid (adherend). In fact, if we let a drop of fluid onto the top of a flat subtrate, what we will see is the following profile, Figure 2.6. From that, making use of a goniometer or establishing trigonometric relations the angle of contact might be assessed [83].

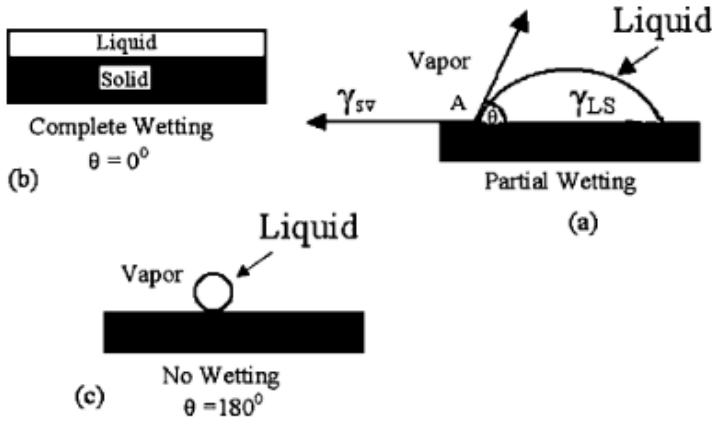

Figure 2.6: The three different possible wetting stages [64]: (a) partial wetting $0^o < \theta < 180^o$, (b) complete wetting $\theta = 0^o$ and (c) no wetting $\theta = 180^o$.

Figure 2.6 also shows the different wetting stages that may occur in any three-phase system, where θ is the angle of contact, measured through trigonometric relationships and other methods [84]. Furthermore, a relationship between the angle of contact and wetting quality may be set: smaller angles imply good wetting, whereas bigger ones the opposite. Strong cohesive force requires good wetting, but it is not solely influenced by it [64].

2.3.2 Electrostatic Attraction Theory

This hypothesis suggests the development of an electrostatically charged double layer of ions at the adhesive-adherend interface, Figure 2.7, causing the forces accountable for the resistance to detach it [85, 86]. An evidence of these attractive forces is the electrical discharges observed when peeling off an adhesive [87].

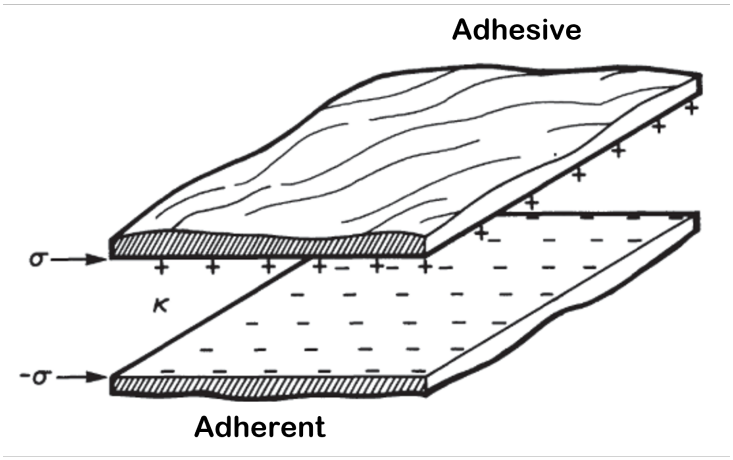

Figure 2.7: Bond formed by electrostatic attraction between oppositely charged planar materials. Adapted from [87].

The strength of the joint will depend on the electrostatic charge gradient between each constituent. However, its contribution in the work of adhesion was found to be less relevant comparing to chemical bonding [88]. The bonding of this type anticipates a possible explanation of polymer/metal adhesive joints.

2.3.3 Chemical Bonding Theory

Amongst all other theories, chemical bonding theory, or molecular bonding, comes as the one of the oldest, and yet, the most employed adhesion bond theory [64, 89]. Tack and peel tests conducted on construction sealants joined with polymer foams showed that, the main contribution to adhesion come from chemical interactions between each material [90]. Electrostatic attraction and interdiffusion mechanisms were not observed and the effect of mechanical interlocking was found to be negligible, in comparison.

Along with intermolecular forces, polar groups' presence characterize the strength of the adhesive joint between a pair of the same material or dissimilar materials [91]. Chemical bonding techniques desired prerequisite is the intimate contact between each substrate, as shown in Figure 2.8. Nevertheless, caution with this contact must always be in mind, due to the usual presence of imperfections on this interface [92].

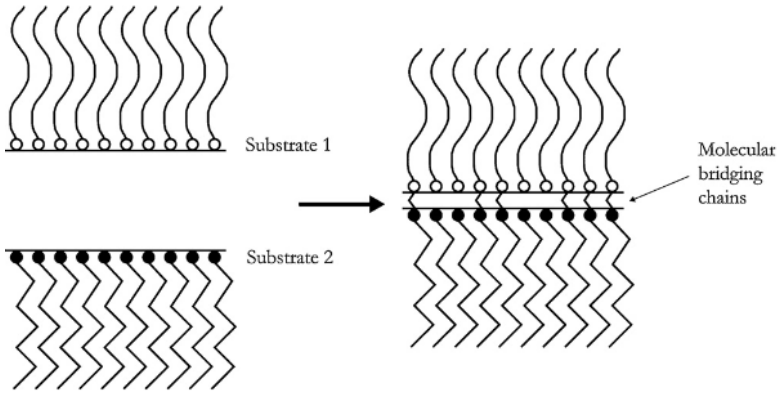

Figure 2.8: Schematic of the chemical bonding between two substrates. Adapted from [91].

Figure 2.8 also shows the composition of a molecular bond: the link between a chemical group on the adhesive surface (substrate 1) and a fitting chemical group on the adherend (substrate 2). This mechanism of adhesion is mainly appraised as primary bond in comparison with physical interactions forces, such as van der Waals, otherwise named as secondary force interactions [93].

Coupling agents are the adhesion promoter molecules used to increase the strength of the bond between the adhesive and the substrate (as well as befitting surface pretreatments) [64, 93, 94]. In fact, the mechanical performance of an adhesive joint is utterly dependent on this strength, thus the crucial importance of such instruments. These molecules are able to chemically react at each end of the interface, consequently creating a chemical bridge at the interface. Silane based molecules are the most commonly used promoter adhesion agents.

2.3.4 Mechanical Interlocking Theory

McBain and Hopkins [95] introduced this theory back in 1925. The most fascinating data retrieved from their experiments on adhesion mechanisms comes from a solely mechanical joint between wood and animal based glue. The glue flows into the surface irregularities of the wooden material, anchoring itself in those cavities, Figure 2.9, sustaining the strength of the adhesive entirely on these grips [91, 93, 96].

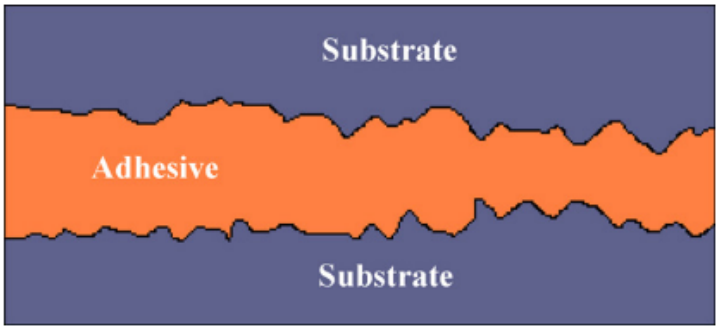

Figure 2.9: Illustration of mechanical coupling between two substrates. Adapted from [91].

Although increased surface roughness potentiates the ability of the adhesive material leaking into the adherend surface's irregularities, this mechanism of adhesion is only sufficient to enlarge the surface

area in which both substrates make contact, thus facilitating chemical bonding and wettability of this coupling. Hereby, mechanical interlocking is not a technique at the molecular scale. It is merely an engineered route to increase the absorption of the adhesive on the substrates [93, 97, 98].

As shown in Figure 2.9, this theory entails the physical interlocking of the adherend surface and the cured adhesive at the macroscopic level. Moreover, further studies suggested the possibility of three distinguished slits on the adherend surface [99], Figure 2.10, in which only one of them leads to mechanical interlocking: type *a*. Mechanical anchoring entails type *b* irregularities, whereas in type *c*, the joint strength will depend on the direction of the load applied to the adhesive interface.

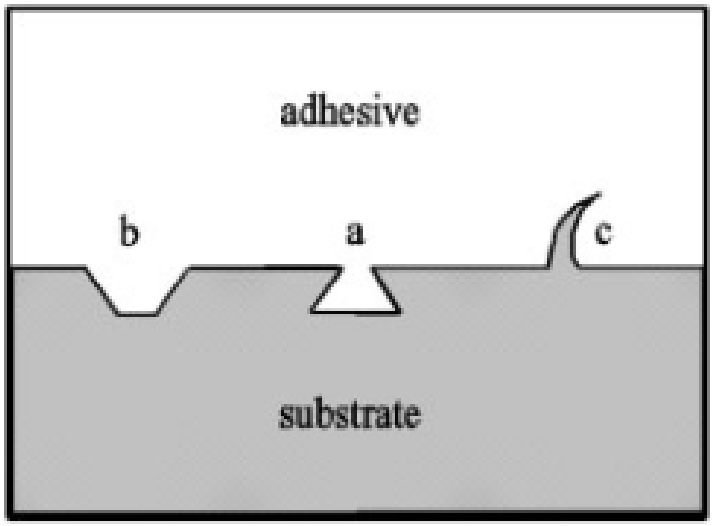

Figure 2.10: Different types of surface irregularities. Adapted from [99].

From the aforementioned discussion, mechanical interlocking is responsible for a proper adhesion only under enough wetting of the adhesive on the adherend surface. A lower viscosity adhesive must be chosen in order to fill in the cavities or pores of the substrate to be wetted. If not, a poor wetting might occur, Figure 2.11(b). Consequently, the mechanical strength of the adhesive bond will bear a weak joint.

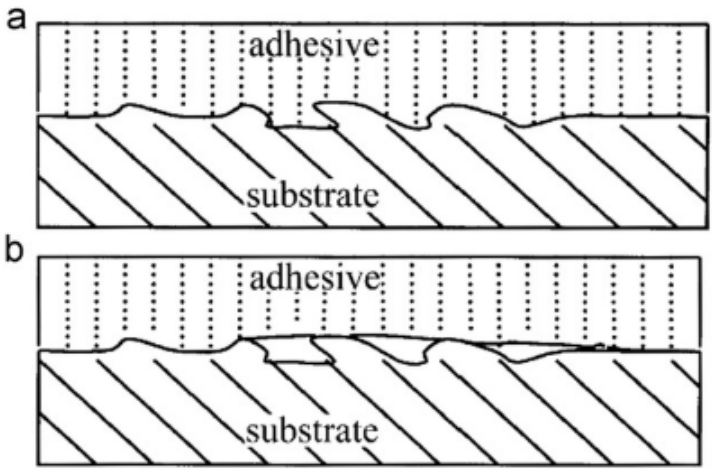

Figure 2.11: Good wetting (a) and poor wetting (b). Adapted from [100].

Amidst the others adhesion mechanisms, mechanical interlocking should only be stated as a combined attribute added to the previously mentioned theories of adhesion. For substrates that are impenetrable to the adhesive, along with those that have sufficient surface irregularities, this theory might be the best suited [100].

2.3.5 Diffusion Theory

Voyutskii and Vakula [101] concluded that no other theory besides diffusion's would be able to explain the mechanisms of adhesion that arise when a bond forms between non-polar polymers. In their opinion, the cause for a successful union between two polymeric substrates of this kind was the interdiffusion of the macromolecules at the interface, as shown in Figure 2.12.

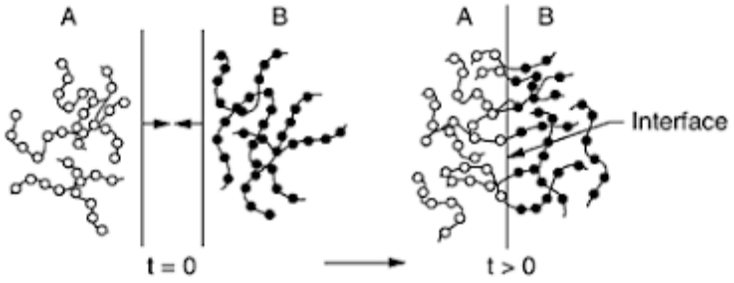

Figure 2.12: Interdiffusion of adhesive (a) and substrate molecules (b). Adapted from [96].

An important consideration within the scope of this theory is: both the adhesive and the adherend must be mutually miscible and compatible polymers with long-chain molecules [80, 93]. This theory reflects the importance of contact time, the chain length of the macromolecule, the concentration and the temperature on the effectiveness of the bond. Voyutskii and Vakula [101] also related the success of this mechanism with the solubility of each polymer. In fact, diffusion is ideal when this characteristic is identical for both materials.

2.3.6 Weak Boundary Layer Theory

First detailed by Bikerman et al. [102], this theory asserts that, in the event of failure on an adhesive joint, a cohesive break of a weak boundary layer is the most likely scenario to have caused it. This layer might occur from the adhesive, the adherend, the presence of air or other contaminants, and a combination of any of those variables. Assuming a failure at the vicinities of the interface with minor applied stresses, it is safe to conclude the weak boundary layer being responsible for the lower cohesive strength between the adhesive and the adherend [103].

Bikerman et al. [102] proposed seven classes of weak boundary layers, as illustrated in Figure 2.13, where it can be denoted various likely causes for the formation of a deficient film on the boundary of the joint.

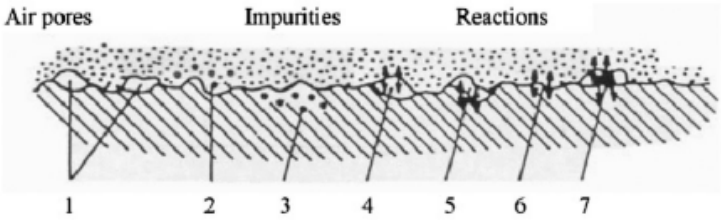

Figure 2.13: Bikerman's model of the weak boundary layer. Air pores (1), impurities in the adhesive (2) and in the adherend (3), reactions at the interface (4) to (7). Adapted from [102].

Some materials prone to suffer from this adhesive's irregularities are fluoropolymers [104] and metal oxides [80]. From the incompatibility of the first with most of available adhesives, the absorption cannot take place between the two substrates, giving place to the formation of a weak layer. Surface pretreatments have been proven to decrease the probability of weak boundaries occurrence in these materials [64].

Further studies have also shown evidence of weak boundary layer's formation and its influence in joints susceptible to failure [105].

2.4 Surface Treatments

Aforementioned theories already inferred on the importance of a proper compatibility of the interface between both substrates desired to form the adhesive joint and its structural response to external loads. Throughout this section, it is intended to focus on the effect of surface treatment to improve the referred adhesion, advancing some conclusions observed in previous researches.

Bringing back the mechanical interlocking theory, Putman and Vaidya [106] compared the influence of friction coefficient, matrix stiffness and cohesive bond on the interlocking effect between two different substrates. Their research reported a highly superior contribution of friction coefficient to mechanical interlocking in comparison with the rest. And an increase in friction coefficient correlates with an increment in surface roughness of the material [107]. Ochoa-Putman and Vaidya [108] found exactly the same behaviour when joining steel and Polypropylene (PP).

In the scope of our research, surface roughness' parameter is highly important, thus enabling an easier flow of the molten polymer into the rough surface of the metallic substrate.

Another conclusion regarding the research conducted by Ochoa-Putman and Vaidya [108] was the effect of adding polar functional groups to the surface of the polymeric substrate and its positive influence on adhesion strength with steel. This interface was also benefitted by the addition of silicon coating to the surface of the steel, which subsequently forms chemical links with the polymer. Chueh et al. [109] verified the same effect in this study. These conclusions point to an increase in wettability when combining the incorporation of polar functional groups to a polymer joined with a silicon coated steel.

In the work of Packham et al. [110], it is presented a thorough research on the influence of surface energy and surface roughness on adhesion, coming to the particular field of metal to polymer adhesion. Supporting previous researches, they extend the relation between surface free energy and surface roughness (a direct consequence enhanced by most of existing surface treatments). It is also

stated that, under the best conditions of adhesion, a polymeric substrate flows easily into the topographical features of a metallic substrate. Again, only under the ideal conditions, when contact area between each substrate is not reduced. Grit-blasting technique is referred as the ideal surface treatment on metallic mediums, as [111–113] also demonstrated. And, once more, these treatments play a major role by chemically activating polar groups on the substrate surface and increasing the fracture energy of the adhesive joint, as stated above, as well as enabling the joint to easily redistribute the stress, under loading, and increasing stress dissipation.

An important remark about the analysis of surface treatment's influence on adhesion comes by looking at the convergence of absorption theory into the mechanical interlocking one, when moving from smaller scales into bigger ones [110].

2.5 Primers

Bearing in mind the advantage of surface treatment and a careful choice of material's combination when successfully joining dissimilar materials, as described above, some substrates may still provide only negligible adhesion. Many features contribute to this fault, with low surface energy of the substrate and a cohesively weak boundary layer being the most likely ones. When this happens, primers or adhesive promoters may come to aid with further joining strength, Figure 2.14.

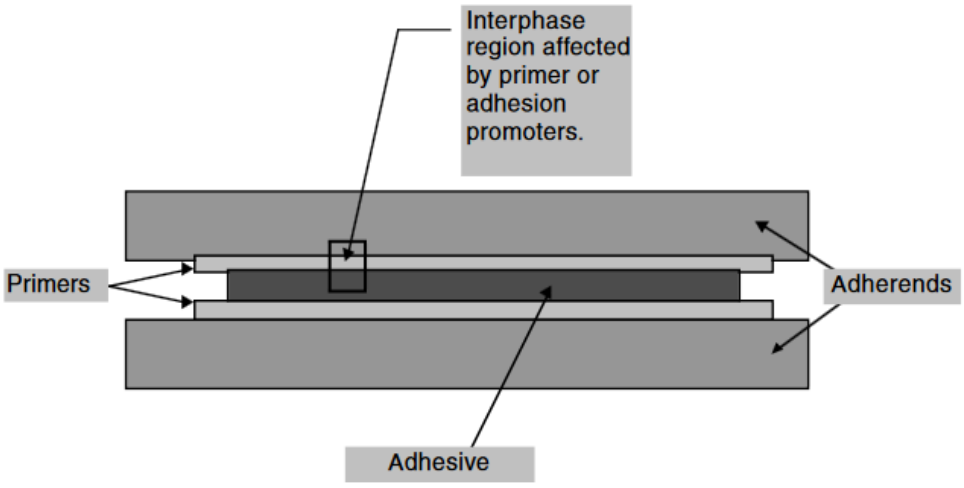

Figure 2.14: Schematic of primers and adhesive promoters. Adapted from [114].

Along this, and particularly important when referring to our work, is the importance of primers when trying to join high-temperature polymers, such as polyimides (Nylon) and ABS. These kind of plastics usually have poor wetting characteristics, thanks to its higher viscosity during the adhesion process. A solvent might help in reducing this variable, however, it must be carefully used to prevent damaging the structural strength of the joint. Taking this into account, it is preferable to use a primer, which is, fundamentally, a dissolved version of the adhesive, but now with an enhanced wetting ability [94, 113].

Within the scope of adhesion promoters, it is relevant to cite the research conducted by Objois and Gilibert [115] and its findings about the importance of adhesive thickness upon the extent of microcracks initiation, fracture propagation and, consequently, ultimate break. The optimal value of the adhesive

thickness, in which they obtained the maximum mechanical strength of the joint (scarf joint bonded structure) was found to be close to 0.1 mm, Figure 2.15.

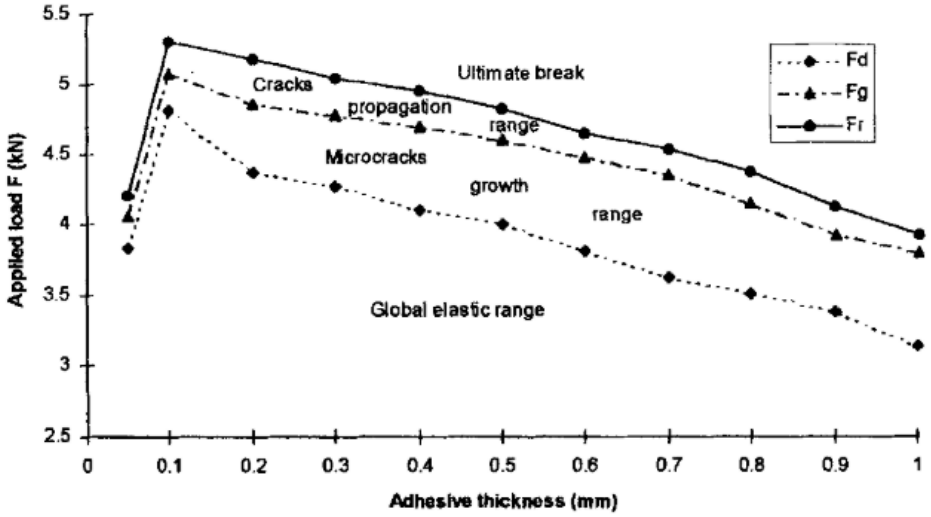

Figure 2.15: Influence of the adhesive thickness on the maximum applied load of a scarf joint bonded structure, illustrated by the threshold Fd of the first microcracks, the threshold Fg of the flaw propagation and the threshold Fr of the ultimate break. Adapted from [115].

2.6 Additive Manufacturing of Multi-Material Components

In this section, novel AM techniques of multi-material components are presented. Multiple benefits are listed, as well as ground-breaking discoveries on the influence of surface treatment and fibers in the adhesion strength of such joints.

Shaped Deposition Modeling (SDM) is introduced in [116], giving an insight of multiple applications with Polymer/Metal Hybrid (PMH) components. Here we can see the great potential of this hybrid components in industries such as automotive (PMH showed higher specific strength than common metal sheets used in most vehicles) and electrical systems (metallic components embedded in plastic matrixes, which guarantees conductivity while decreasing its structural weight). An example of a possible component manufactured with this technology is presented in Figure 2.16 (a).

Falck et al. [13] brings us the novel AddJoining technique. In here, single-lap joints of Aluminium and polymer filaments are joined with FFF only. Subsequently, mechanical tests confirmed a strong bond promoted by intermolecular diffusion between the materials.

FFF is of great interest given its common usability in most domestic 3D printers. However, its use with a hybrid polymer/metal filament is not yet thoroughly studied for large scale production of components [117]. In this study, hybrid filaments are used to fabricate PMH components (illustrated in Figure 2.16 (b)), after which, mechanical tests are performed and the influence of printing temperature, nozzle's diameter and composition of mixture are evaluated.

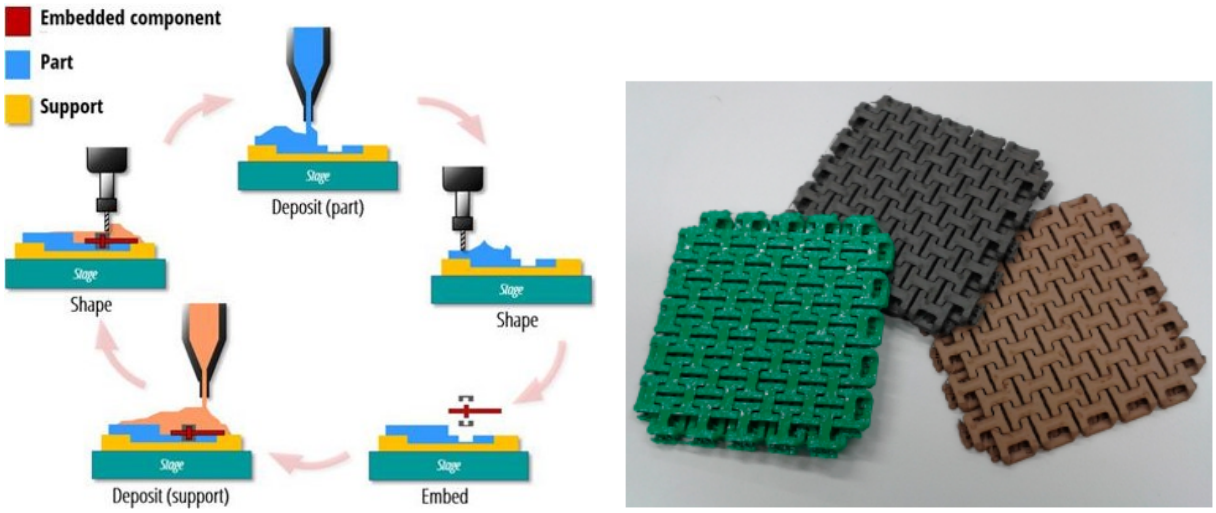

Figure 2.16: FFF of polymer-metal hybrid components: (a) Link and Bearings being embedded between shaping and deposition operations [116]. (b) 3D printed objects with hybrid filaments [117].

Micromechanics of amorphous PMH structures was evaluated in [118], particularly the adhesion strength of electroless deposition of an amorphous layer of nickel-boron (NiB) on top of 3D printed plastic parts' surface, Figure 2.17. Micrometre-scale pores in plastic's surface improve the anchor effect of metallic coating once its deposited on top of polymers.

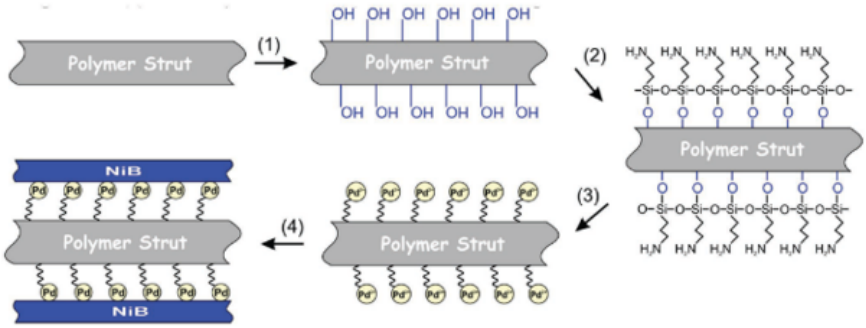

Figure 2.17: Electroless metallization of a polymer template: (1) a surface activation of the polymer template, (2) functionalization with a monolayer of amino-modified silane compounds, (3) Pd catalyzation, and (4) NiB electroless deposition. Adapted from [118].

An experimental apparatus composed of an integrated laser-based Powder-Bed Fusion (PBF) and FFF is used for 3D printed PMH components, [109]. The inter-locking structures created with PBF enable an easier flow of the polymer melt into the metal surface, creating "anchors" responsible for strengthening the bond between both materials. This adhesion mechanism starts by metal powder's (316L stainless steel) solidification, creating these inter-locking structures with the PBF extruder. After that, FFF extruder takes the wheel, depositing melted polymer filament (Polylactic Acid (PLA) and Polyethylene Terephthalate (PET) were both independently used) on top of metal substrate, at the same time as this metallic base is heated, decreasing the polymer viscosity and facilitating its flow into those metal cavities. This melted plastic material is compressed, and laser scanned, boosting the inter-molecular adhesion between metal and polymer.

Lucchetta et al. [119] introduced the Aluminium (Al) sheet surface correlation with adhesion in PMH overmolding. Surface treatment of Aluminium sheets was previously held (shot peening with granular corundum) increasing surface roughness' values, easing the flow of Polypropylene (PP) and Polyphenylene Sulphide (PPS) into metal surface. Besides roughness correlation with adhesion between metal and polymer in PMH components, the presence of reinforcement glass fibers, metal sheet pre-heating and injection speed were also analysed. It was then concluded that fiber's reinforcement plays a bigger role in adhesion strength than roughness itself. Their findings are graphically shown in Figure 2.18.

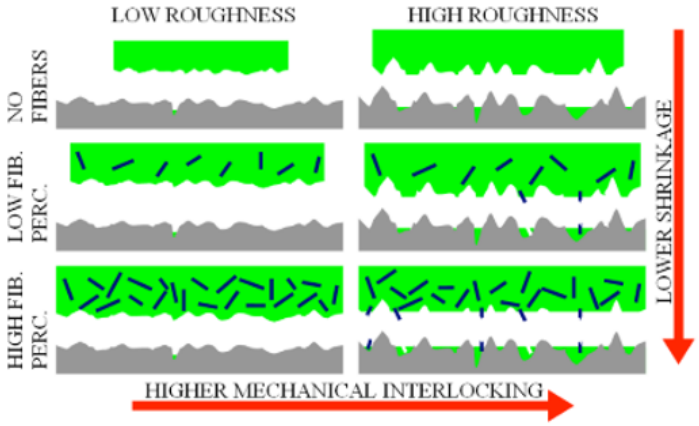

Figure 2.18: Concurring phenomena in polymer to metal interlocking. Adapted from [119].

2.7 Adhesively Bonded Joints

Thorough discussion about the desirability of adhesively bonded joints regarding other traditional ones was already made above. Furthermore, there are other aspects that influence the strength of the bond: type of adhesive and joint geometry. Giving the particularities of our work, the geometry of the joint was the only one we could focus on. Tracing back the literature on which are the most common ones, single-lap joints (SLJ), double-sided joints (DSJ), stepped-lap joints and scarf joints [120, 121], as illustrated in Figure 2.19, were the most cited.

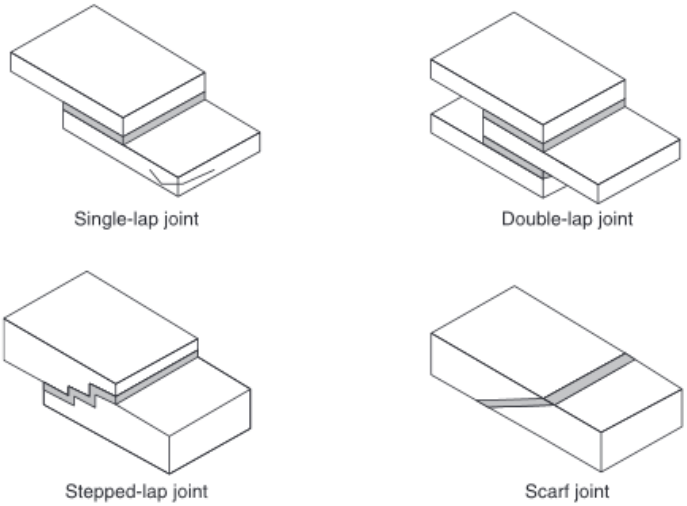

Figure 2.19: Most usual types of bonded joints. Adapted from [122].

Due to the popularity and widely use of single-lap joints, we found in this type of joint an ideal choice for this thesis. Some features regarding this joint and an explanation about different common failures in adhesive bonding are briefly discussed in the following sections.

2.7.1 The Single-Lap Joint

The single-lap joint geometry, Figure 2.20, has been extensively studied [123, 124]. On that account, multiple joint analysis have surged in order to better predict the joint strength. Hence, it is essential to possess enough data regarding the stress distribution and the failure criteria.

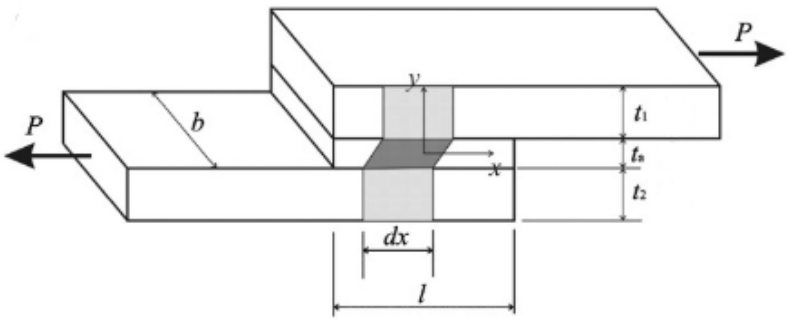

Figure 2.20: Single-Lap Joint Geometry's illustration. Adapted from [124].

Literature points out to multiple ways of analysing the stress distribution of a single-lap joint. Lucas et al. [124] made a summary of both linear and nonlinear 2D analytical models already studied; however, it is not the scope of this chapter to extensively describe each one of them. Accordingly, we will just resume some classical analyses. In the simplest one, the adhesive is able to deform in shear only and the adherends are rigid, Figure 2.21 (a); whereas if we need to consider the elasticity of the adherends,

Volkersen's analysis [125] is preferred, Figure 2.21 (b).

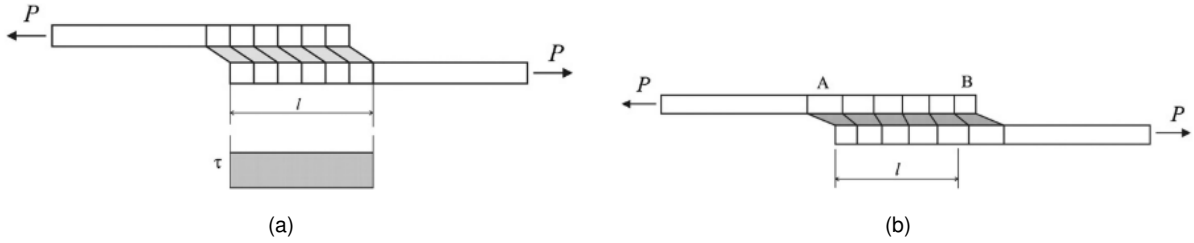

Figure 2.21: SLJ linear behaviour under stress: (a) adhesive deformation with rigid adherends and (b) with elastic ones. Adapted from [124].

In Figure 2.21(a), it is also denoted the shear stress distribution for the simplest classical analysis, which can be translated into the average shear stress, τ, that is performing on the overlap area of the joint and is carried out by:

$$\tau = \frac{P}{bl} \tag{2.1}$$

where P is the applied load, b is the joint width and l is the overlap length.

Volkersen proposed an alternative analysis, in which the adhesive remained deforming in shear only, but the adherends were considered elastic (an improved estimation for polymeric adherends, for instance), therefore, deforming in tension, as illustrated in Figure 2.21 (b). This figure shows a maximum tensile stress at location A, whereas in B it decreases to zero. Further analysing the whole joint, the shear stress distribution increases until the end of the overlap and is much lower at the middle, as seen in the first plot of Figure 2.22. Although a great improvement in adhesively bonded joints' stress analysis, these classical theories do not take into consideration the stress-free condition that takes place at the end of the overlap, as can be seen in the second plot of Figure 2.22; which translates into greater errors when estimating the stress at these particular locations.

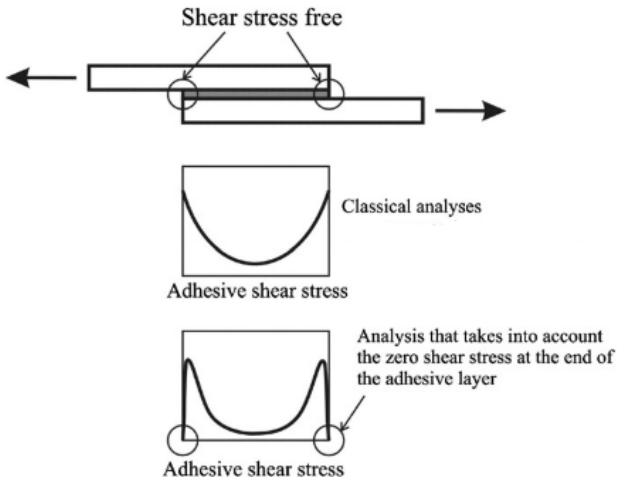

Figure 2.22: Adhesive shear stress distribution. Adapted from [124].

However great for introducing some degree of complexity to shear stress distribution of single-lap joints, Volkersen's analysis fails to consider the bending effect resulted from the eccentric load path of

this type of joints subjected to an axial loading [125], as shown in Figure 2.23.

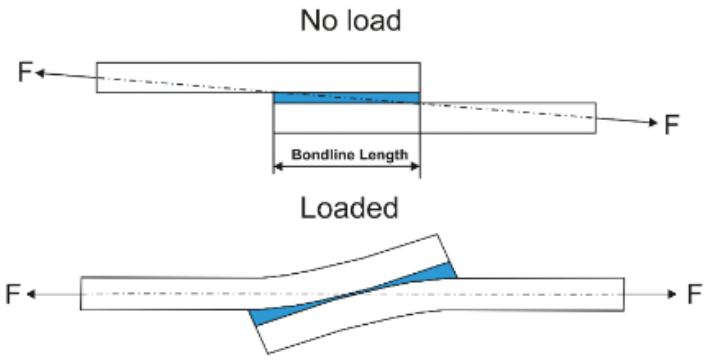

Figure 2.23: Deformed shape of a SLJ when subjected to an axial loading. Adapted from [123].

As a consequence of the aforementioned bending moment, a transverse normal stress will be created in the adhesive layer, which is also called peel stress. The first ones to take this bending effect into consideration on the stress analysis' formulation were Goland and Reissner [126]. Figure 2.24 illustrates the result in the stress distribution of this joint, when considering a bending effect, a more correct analysis of a SLJ subjected to an axial loading.

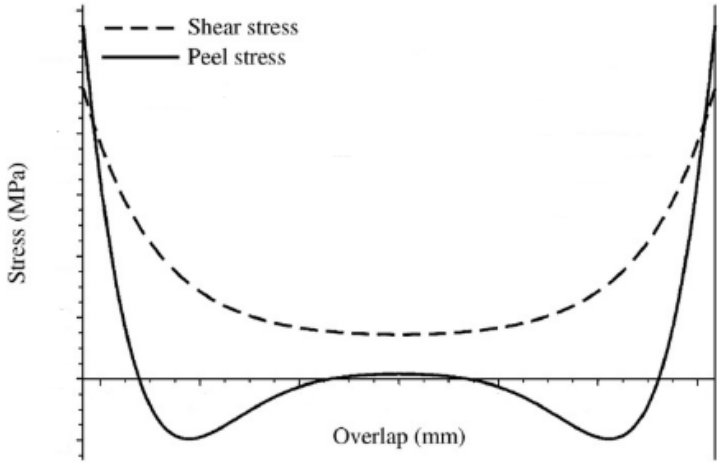

Figure 2.24: Shear and peel stress distribution accordingly to Goland and Reissner's formulation. Adapted from [124].

2.7.2 Failure Criteria

Maximum normal stress theory, maximum shear stress theory, maximum distortion energy theory, and many others, are already firmly in place failure criteria for homogeneous isotropic materials. In order to better understand the macromechanical failure behaviour of composites, taking into account its anisotropy, homogeneity and linear stress-strain performance to failure, many theories were established to do so. The most known ones are the maximum stress theory, the maximum strain theory, Tsai-Hill theory and the Tsai-Wu theory [127, 128].

Maximum Stress Criteria

According to the maximum stress theory, failure occurs when either one stress component along the principal material coordinates exceeds the respective strength. Being σ_1, σ_2 and τ_6 the stresses aligned with the principal material axes, for tensile ones, the failure criteria may be displayed in the form of the following equations [127],

$$\sigma_1 < X_t \qquad \sigma_2 < Y_t \tag{2.2}$$

and for compressive stresses,

$$\sigma_1 > X_c \qquad \sigma_2 > Y_c \tag{2.3}$$

Moreover,

$$|\tau_6| < S \tag{2.4}$$

where,

$X_t =$ longitudinal strength in tension, along direction 1;

$Y_t =$ transverse strength in tension, along direction 2;

$X_c =$ longitudinal strength in compression, along direction 1;

$Y_c =$ transverse strength in compression, along direction 2;

$S =$ shear strength along direction 12.

If any of these inequalities are not satisfied, one of five failure mechanisms took place in the composite.

Maximum Strain Criteria

Similarly with the maximum stress failure criteria, the composite material fails when the strains aligned with the principal material axes (ϵ_1, ϵ_2 and γ_6) fail to meet the following sub-criteria,

$$\epsilon_1 < X_{\epsilon_t} \qquad \epsilon_2 < Y_{\epsilon_t} \tag{2.5}$$

$$\epsilon_1 > X_{\epsilon_c} \qquad \epsilon_2 > Y_{\epsilon_c} \tag{2.6}$$

$$|\gamma_6| < S_\epsilon \tag{2.7}$$

Where,

$X_{\epsilon_t} =$ maximum tensile normal strain along direction 1;

$Y_{\epsilon_t} =$ maximum tensile normal strain along direction 2;

$X_{\epsilon_c} =$ maximum compressive normal strain along direction 1;

$Y_{\epsilon_c} =$ maximum compressive normal strain along direction 2;

$S_\epsilon =$ maximum shear strain along direction 12.

Tsai-Hill Criteria

This theory arose as an extension of von Mises's yield theory, but for orthotropic materials [127]. Contrary to the previous criterions, Tsai-Hill's dismisses the independence of each stress along principal material coordinates. In this way,

$$\frac{\sigma_1^2}{X^2} - \frac{\sigma_1\sigma_2}{X^2} + \frac{\sigma_2^2}{Y^2} + \frac{\tau_6^2}{S^2} = 1 \tag{2.8}$$

is the ruling failure criteria for an orthotropic composite material in function of X, Y and S, which are the maximum longitudinal strength, the maximum transverse strength and the maximum shear strength, respectively.

Also, it is worth noting the contrast between tension and compression failure behaviour depends solely on the sign of the principal material coordinate's stresses, σ_1, σ_2 and τ_6.

Tsai-Wu Criteria

Following initial experiments to formulate a general failure theory for anisotropic materials capable of predicting strength under general states of stress and, most significant, being able to reckon the difference between tensile and compressive stresses, Tsai and Wu proposed the following tensor polynomial theory (contracted formulation),

$$f_i\sigma_i + f_{ij}\sigma_i\sigma_j = 1 \tag{2.9}$$

wherein f_i and f_{ij} are strength tensors of the second and fourth rank, respectively, and $i, j = 1, 2, ..., 6$ [128].

Expanding Equation 2.9 into a two-dimensional state of stress, we get the most common formulation for this theory,

$$f_1\sigma_1 + f_2\sigma_2 + f_{11}\sigma_1^2 + f_{22}\sigma_2^2 + f_{66}\tau_6^2 + 2f_{12}\sigma_1\sigma_2 = 1. \tag{2.10}$$

2.7.3 Adherence and Types of Failure

When referring to adhesive bonded joints, there are several types of stresses that commonly show up in the literature [94], being the most common, the ones illustrated in Figure 2.25.

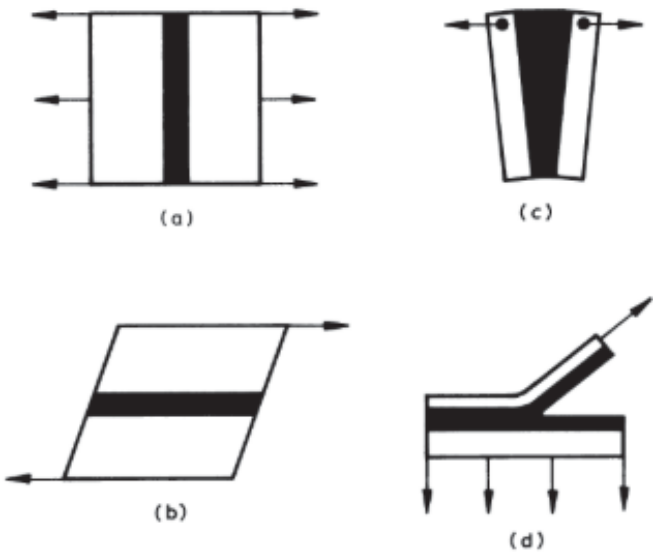

Figure 2.25: Types of stresses: normal stress (a), shear stress (b), cleavage stress (c) and peel stress (d). Adapted from [94].

Within every type of failure in an adhesively bonded joint, Figure 2.26 shows the most usual kind when subjected by preceding loading types [129].

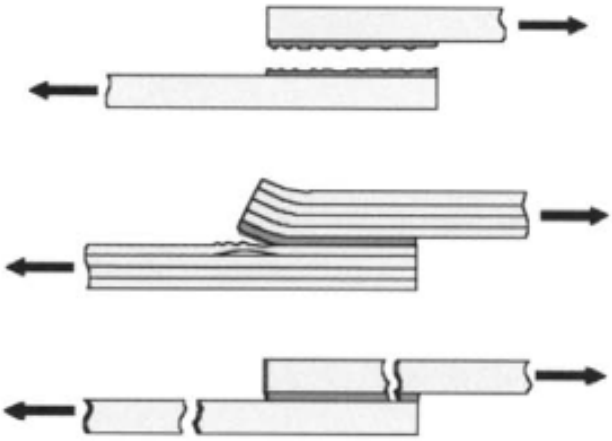

Figure 2.26: Common types of adhesive failures. From top to bottom: cohesive failure of adhesive; adhesive failure and substrate failure. Adapted from [129].

Above mentioned types of failures may be described as:

- **Cohesive failure -** failure of the adhesive itself, which signals a proper surface preparation and adhesive installation.
- **Adhesive failure -** adhesive/adherend's interface failure, an indication of an inadequate surface preparation.
- **Substrate failure -** adhesive's bond stronger than the substrate, so the adherend will eventually fail prior to the adhesion interface.

Chapter 3

Materials and Methods

In this chapter, the design of specimens, materials and methods required for the implementation and validation of this work will be further explained.

3.1 Design of Specimens

The specimens used in our work were adapted from the ASTM D3163 – 01 [130]. The base material was made from Aluminium material and machined in the mechanical engineering department's workshop. Top rectangular piece was priory designed in NX SIEMENS software and later on manufactured in Lab2Prod laboratory's facilities, using a FFF machine (Section 3.3.1). Five samples were tested for each configuration of materials and surface preparation techniques, giving a total of sixty single-lap joint specimens.

As previously stated, the final specimen's geometry was a single-lap joint with two different adherends: an Aluminium base substrate and a polymeric top substrate. The position of the base material in the customized build plate's slot was crucial for the alignment of the final single-lap joint specimen and it was determined by empirical observation of printed samples, as further detailed in Section 3.3.4. The dimensions of the specimens are shown in Figure 3.1.

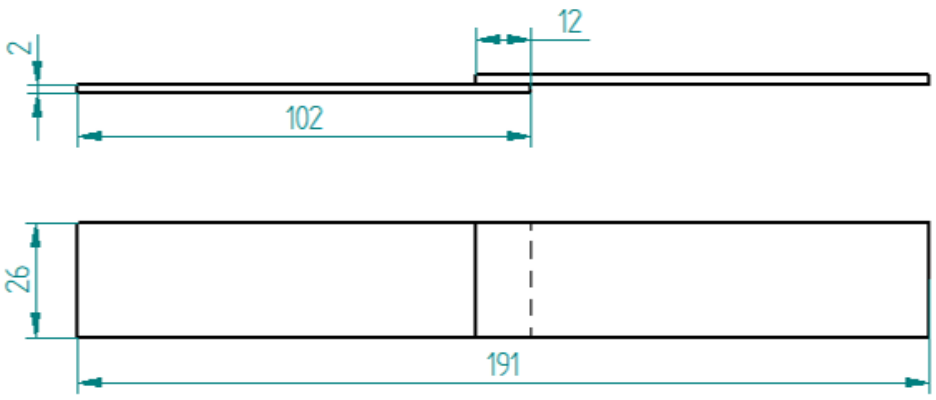

Figure 3.1: Specimen's geometry. Adapted from [130].

3.2 Materials

3.2.1 Aluminium

One of the main variables in this work was the choice of our metallic base material. Aluminium has already been identified as the most common material when joining dissimilar ones, as detailed in

Section 2.6. Adding to its excellent mechanical properties and large amount of applications in multiple industries, its previous use in a similar work makes Aluminium the best choice for our base material (from now on, the Aluminium substrate will be identified as so) [13]. However, due to COVID-19 constraints, the acquisition of an Aluminium sheet was conditioned. In this way, a metallic substrate sheet with a thickness of $2\ mm$ was chosen from a laboratory sample and later on characterized (Section 3.3.7).

3.2.2 ABS

ABS plastic comes a long way in materials' science history. Its application can be traced back to World War II, when bulletproof polymer sheets were made with it, because of its large impact strength. Later, it spread on to make part of toys, domestic appliances, textiles and more, primarily due to the development of injection molding manufacturing technique [131]. The advent of FFF introduced the ABS filament, which increased even more the market share of this plastic [38].

Studies were conducted about the potential of ABS on being successfully plated by metal coatings, evidencing the prospective of using this polymer when joining dissimilar materials [131, 132]. Thus, ABS arises as an ideal choice for engineering applications: high toughness, mechanical strength, good thermal stability and cheapness, to name a few advantages of it [132]. Additionally, Falck et al. [37] had already validated joining ABS polymer to an Aluminium substrate, confirming our initial assumptions when reviewing state-of-the-art articles about metal to polymer adhesion mechanisms. Accordingly, for our first experiment, the chosen material was an ABS blue filament with $1.75mm$ diameter from *MakerBot* brand.

It must be pointed out a few constraints when using this polymer in FFF applications. The most inconvenient one for the conduction of this experiment was the warping effect, already extensively described in numerous researches and highly frequent when printing with ABS filament [133, 134]. This common FFF problem can be explained as a non-wanted distortion on the surfaces of a 3D printed part, a critical point of this thesis, as it will be further explained.

Table 3.1 presents the general properties of ABS plastic, bearing in mind a decrease in these values when evaluating 3D printed ABS components [135–137].

Table 3.1: General properties of ABS plastic. Adapted from [135–137].

Physical	**ABS**
Density	$1.01 - 1.21\ g/cm^3$
Mechanical	
Yield Strength	$18.5 - 51.0\ MPa$
Tensile Strength	$27.6 - 55.2\ MPa$
Elongation at break	$0.015 - 1\ \%$
Hardness	$5.6 - 15.3\ HV$
Young's Modulus	$1.19 - 2.90\ GPa$
Thermal	
Max Service Temperature	$61.9 - 76.9\ ^\circ C$
Melting Temperature	$200^\circ C$
Thermal Expansion Coefficient	$8.46 * 10^{-5} - 2.34 * 10^{-4}\ strain/^\circ C$

3.2.3 Nylon

Polyamides (PA) are a class of high performance engineering thermoplastics, commercially known as Nylon. Likewise other thermoplastics, such as ABS, PA is an interesting alternative to traditionally used thermosets, specifically in composite applications, for its recyclability and an increased fabrication's flexibility [138].

Inside PA class, we can differentiate two groups: aliphatic and aromatic polyamides. Aliphatic polyamides occur much more frequently than aromatic. Within these, there are polyamide 6, polyamide 66 and polyamide 10, among others. Oppositely, within aromatic polyamides' group arises the polymer with one of the highest impact strengths, such as Kevlar [139].

Closely to semicrystalline plastics, PA retain a brittle behaviour up until its glass transition temperature of, approximately, $50\ ^{\circ}C$. Above that value, there is evidence of a decrease in yield and tensile strengths, parallel to an increase in its elongation at break. However, this only happens with dried samples. In fact, PA are highly influenced by moisture (they absorb up to 3.6% of water at ambient temperature and a relative humidity of 50%), which considerably decreases its mechanical properties when in contact with water. The presence of fillers within a PA matrix enhance its mechanical properties and decrease humidity's influence [139].

In our experimental work, a $1.75\ mm$ Nylon (PA6) filament from *Markforged* was used. Its general properties are presented in Table 3.2.

Table 3.2: General properties of Nylon filament. Adapted from [140].

Physical	**Nylon**
Density	$1.1\ g/cm^3$
Mechanical	
Yield Strength	$51\ MPa$
Tensile Strength	$36\ MPa$
Elongation at break	$150\ \%$
Young's Modulus	$1.7\ GPa$
Thermal	
Melting Temperature	$210 - 220^{\circ}C$
Heat Deflection Temperature	$41\ ^{\circ}C$

3.2.4 Nylon CF15 Carbon

When compared with metals, most thermoplastics fall behind in a set of properties, such as tensile strength, maximum service temperature, hardness, moisture absorption and temperature coefficient of expansion (highly characteristic of PA). To defy this, fillers might be impregnated in a polymeric matrix, increasing many properties of the original material, without disputing its mass advantage over metals [139]. Glass, aramides and carbon's fillers are the most popular ones. Falck et al. [13] has already studied the influence of a continuous carbon fiber filament in adhesion strength between PA6 and Aluminium. In here, it was found interesting to study the effect of this fiber in the same type of joint; however, with a slightly different parameter, due to machine's compatibility: milled carbon fibers of

$100\ \mu m$, instead of a continuous one. This filament was manufactured by *Fillamentum* and is characterized by the following properties:

Table 3.3: General properties of Nylon CF15 filament. Adapted from [141].

Physical	**Nylon CF15**
Density	$1.08\ g/cm^3$
Mechanical	
Yield Strength	$54.5\ MPa$
Tensile Strength	$36\ MPa$
Elongation at break	$103\ \%$
Young's Modulus	$500\ MPa$
Thermal	
Melting Temperature	$160\ ^\circ C$

3.3 Methods

3.3.1 3D Printing Process

The 3D printer employed in this thesis was a Raise3D Pro2, which makes part of Lab2Prod 3D printers' portfolio, Figure 3.2 (a). This is a dual extruder machine with direct feed, a large build volume (305 x 305 x $300\ mm^3$), an integrated camera, a HEPA air filter, a wireless controller and a heated bed/build plate. This machine was selected for its diverse filament compatibility (melting temperature up to $300\ ^\circ C$), due to our various types of filaments needed, its big build volume and heated build plate, required when printing ABS and Nylon. The original build plate was replaced by ours, a customized Aluminium one made from the same batch of the specimens, with a slot to insert them.

Raise has its own slicer software, *Ideamaker*, illustrated in Figure 3.2 (b). Although less advanced than *Cura*, from Ultimaker brand, the learning curve was faster due to a higher compatibility to the machine itself, adding to extra features exclusive for Raise3D machines. When connected to the wireless controller (our laptop must be linked to the same network as the printer, via physical location or VPN connection), this software enables to control the print and watch it live using the integrated camera.

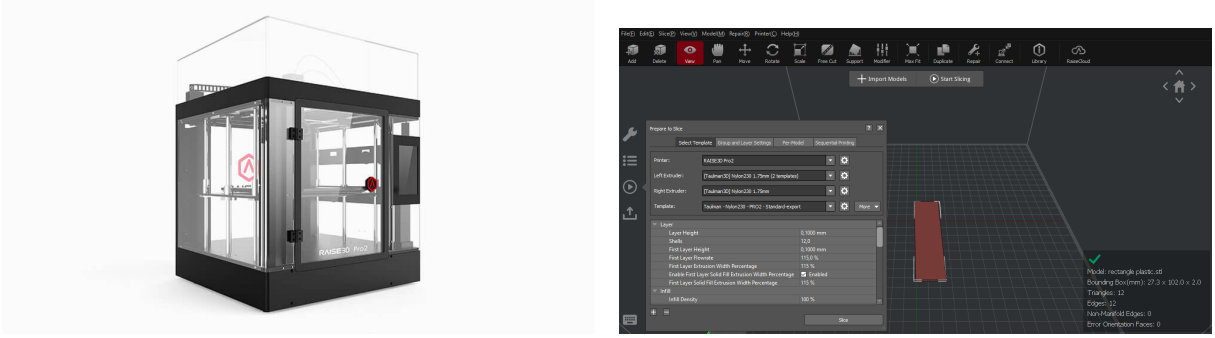

(a) (b)

Figure 3.2: (a) Raise3D Pro2 and (b) Ideamaker software.

In order to fix our specimens on top of the build plate and make sure our base material (Section 3.1) was at the same high as the build plate itself, it was required to create a slot in it, Figure 3.3 (a). Given

this, a customized build plate was manufactured and later on fixed on the machine with binder clips, very usual within 3D printing context.

To start with, a $2mm$ thickness Aluminium sheet was chosen from one of Lab2Prod material samples and machined to fit original Raise3D build plate's area: 305.0 x $305.0\ mm^2$ (Appendix A). Then, a slot was opened and its corners were rectified to accommodate our specimen's base material, as illustrated in Figure 3.3 (b).

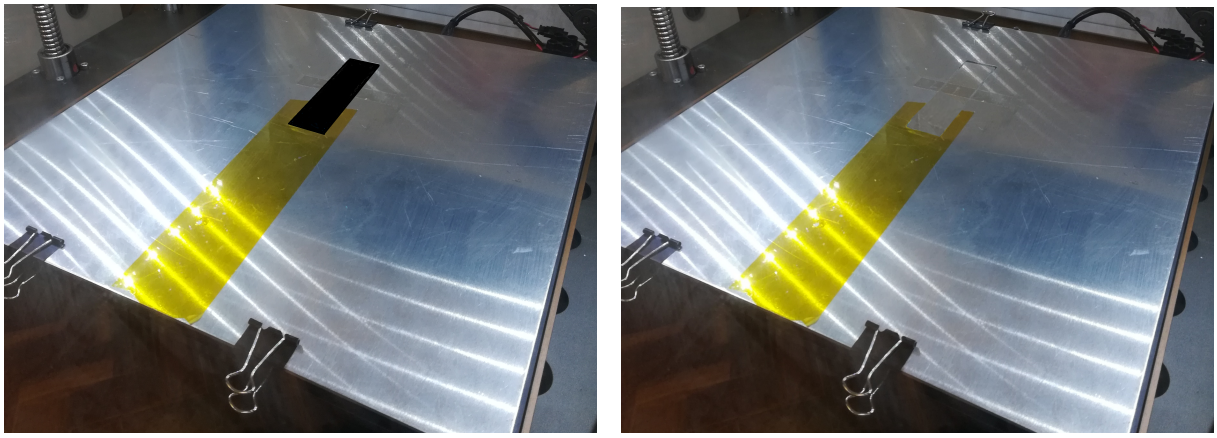

(a) (b)

Figure 3.3: Customized build plate mounted on the original bed slot (a) without the base material substrate and (b) with it.

3.3.2 Calibration and Optimization

FFF started by determining optimum printing parameters for the polymeric top adherend's manufacturing. Given the extent of every printing parameters, time availability and main goal of this work, we have only focused in build plate's temperature (BT), brim loop lines (BLL) and adhesion promoter between the polymeric top adherend and the build plate. The optimization of these variables assured us a top adherend without warping and an optimum autohesion between each printed raster [142]. Other important variables such as printing temperature, deposition speed and flow rate were fixed for each polymer, as specified in manufacturer's printing guides and previous researches with same materials [37, 141].

To assure lower discrepancies in results, build plate was leveled every time a print was about to start. Raise3D Pro 2 machine has a levelling screw on the left side of the front door, which was used to guarantee a nozzle height in relation to the build plate constant and equal to $0.15\ mm$, at every point on the bed. A schematic of this process is illustrated in Figure 3.4.

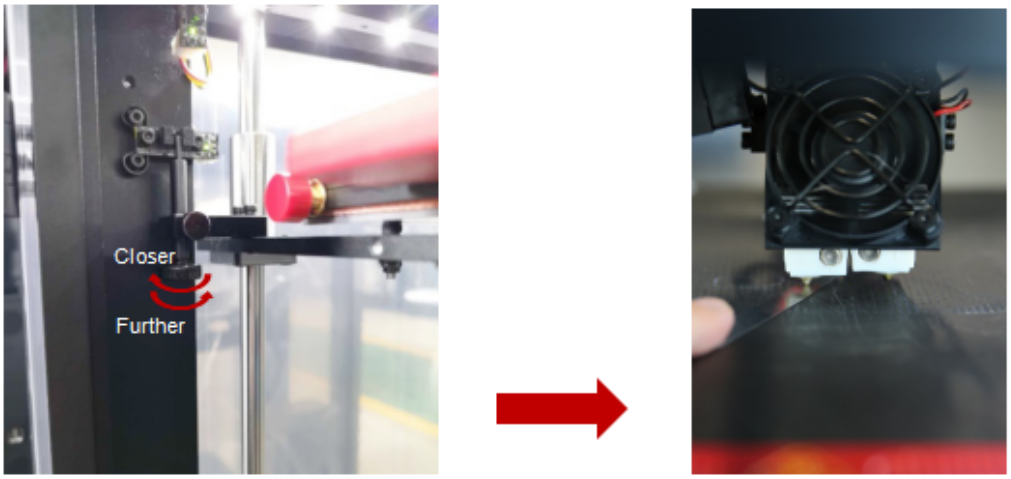

Figure 3.4: Nozzle height calibration on Raise3D Pro 2 FFF machine. Adapted from Raise3D online technical documentation.

In order to quantify the optimum parameters, each polymer's sample was printed out of position.

An ABS type specimen was printed with BT = $100°C$ and without any BLL or masking tape's application. The result was a smooth lined ABS specimen with curved edges, demonstrating warping effect. Then, BT was increased to $110°C$, resulting in an improved printed specimen with warping also. Reaching the maximum allowable build plate's temperature for this machine, it was required another tool to achieve a specimen without signs of warping. Kapton tape was then used to mask the build plate [143]. This polyimide tape assured a proper adhesion of ABS during printing and an easier removal after it, a requirement knowing top adherend's future application. An optimized printing setup was then found for ABS type samples without the need of BLL, as illustrated in Figure 3.5 (a).

Nylon test followed the same procedure without a satisfactory result at BT = $110°C$, with and without Kapton tape's application. Another tape was then introduced to postpone the use of BLL, a higher time consuming technique than just changing the masking tape. Blue masking tape (BMT) was used on top of the build plate and the following Nylon specimens were printed on top of it. A notorious improvement was visible, but still with warping signs. So, BLL was introduced. We started with BLL = 10 and followed with BLL = 25, due to poor performance of the first one. An ideal Nylon specimen was assured with the last, as illustrated in Figure 3.5 (b). Brim was removed with a box cutting blade.

(a) (b)

Figure 3.5: (a) ABS and (b) Nylon top adherend printing's calibration.

Nylon CF15 print was the most demanding to calibrate. BT was increased until its maximum allowable. No tape, Kapton tape and BMT's application was tried and BLL was increased up until 45, in order to achieve a perfect print without signs of warping.

In Table 3.4, an outline of the ideal printing parameters for each polymer is shown.

Table 3.4: Outline of printing's setup for each polymer's type.

Polymer	Tape	BT [$^{\circ}C$]	BLL
ABS	Kapton	110	N/A
Nylon	BMT	110	25
Nylon CF15	BMT	110	45

Already knowing the printing's setup for each polymer type, it was then required to adjust top adherend's final position, in order to print it directly on top of the base material's overlap area. Assuring that the customized build plate was firmly in place, the position of the top adherend was identical for every hybrid joint. From the customized build plate and top adherend's dimensions, its final printing position was identified and settled in *Ideamaker* with the following coordinates: $(x, y, \theta) = (10.4, -22.4, 91^{\circ})$.

These coordinates represent the centroid of the top adherend and were determined knowing the right extruder's offset in relation to the left one: $30\ mm$. This happened because *Ideamaker* makes the left extruder the primary one and position the 3D printed object relative to its coordinates.

After top adherend's manufacturing was succeeded, it was interesting to study the influence of further base material's setups; other than previous researches did [13, 37]. As mentioned before, two surface abrasion techniques were performed on top of base material's overlap area, along the setup without any kind of abrasion. Besides, primer's influence on adhesion was also studied for every PMH specimen. Primer's application is utterly described in the following subsections. In here, the relevance remains with the existence of a primer itself and its influence in PMH specimens' manufacturing.

Without any primer's application, every polymer's type was printed on top of a non-abraded base material. The first printed layer of each polymeric material failed to adhere to the base material, removing

this setup from the process applicability. The following setup, P120 sandpaper's abrasion, followed the same procedure, succeeding with Nylon and Nylon CF15 only. Grit blasting technique worked with every polymer's type, a result already expected due to its greater applicability on metal-to-polymer specimens' manufacturing (Section 2.4).

This test was followed by primer's influence one. Thus, each PMH's primer was applied on top of every base material's surface setup. For every polymer, the primer only adhered to the grit blasted surfaces. For Nylon and Nylon CF15, primer adhered to P120 sandpaper's treated base materials. ABS primer failed to adhere to the former treated surface. An outline of the aforementioned work and their results are presented in Table 3.5. As shown, primer's application was indispensable for continuing the experimental work.

Table 3.5: Outline of base material's different setups.

Polymer's Type	Surface Treatment's Type	Primer's Application	Result
ABS	N/A	No	Fail
ABS	N/A	Yes	Fail
ABS	SP	No	Fail
ABS	SP	Yes	Fail
ABS	SB	No	Fail
ABS	**SB**	**Yes**	**Success**
Nylon	N/A	No	Fail
Nylon	N/A	Yes	Fail
Nylon	SP	No	Fail
Nylon	**SP**	**Yes**	**Success**
Nylon	SB	No	Fail
Nylon	**SB**	**Yes**	**Success**
Nylon CF15	N/A	No	Fail
Nylon CF15	N/A	Yes	Fail
Nylon CF15	SP	No	Fail
Nylon CF15	**SP**	**Yes**	**Success**
Nylon CF15	SB	No	Fail
Nylon CF15	**SB**	**Yes**	**Success**

Legend: *N/A* for non abraded specimens, *SP* for abrasion with sandpaper and *SB* for abrasion with sandblasting/grit blasting technique.

3.3.3 Base Material's Surface Pretreatment

Surface roughness' influence in adhesion between dissimilar materials has already been thoroughly reviewed above in Section 2.2. In here, the overlap area of the base material (25.5 x $20.0\ mm^2$) was mechanically changed to study its influence on adherence strength with three different polymers fabricated by FFF.

For each fabricated specimen, the surface's treatment always started by cleaning the overlap area from any type of grease or impurity, with Isopropyl Alcohol (IPA). After this, there were three possible configurations, as shown in Figure 3.6: non abraded, abraded by sandpaper or abraded by grit blasting.

The base material was abraded with brown corundum particles, Al_2O_3 mostly, with an average granulate size of $256\ \mu m$ and a pressure of $6\ bar$ (for the sandpaper abrasion technique, the size of the

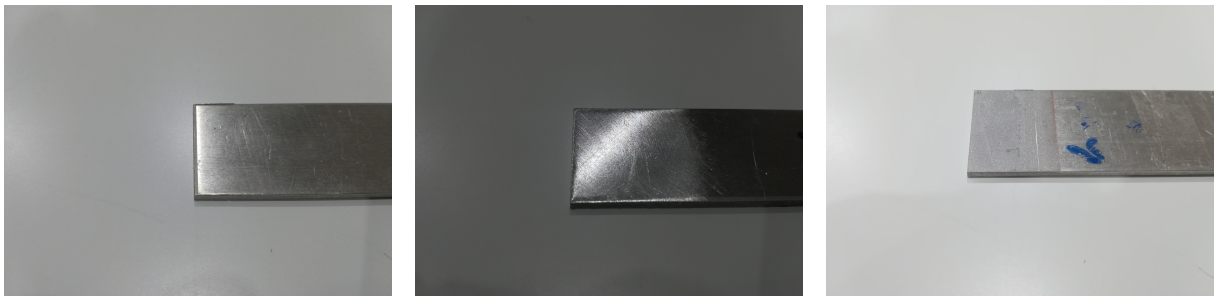

(a) (b) (c)

Figure 3.6: Detail of the base material overlap area: (a) non abraded, (b) mechanically abraded by sandpaper and (c) by grit blasting technique.

same particles was, on average, $125\ \mu m$). The uniformity in every variable of the experimental work was crucial to minimize the disparity in the results. Surface treatment was no exception; each sample was inclined at an angle of 45^{o} relative to the blasting nozzle, as well as a working distance of $200\ mm$, during $20\ s$. Along this, the path followed by the nozzle gun and the sandpaper was controlled and done accordingly to the one illustrated in Figure 3.7, a result of a previous research [144]. However, this last process was much less consistent than grit blasting technique, due to a reduced pressure control (a direct consequence of being made by hand).

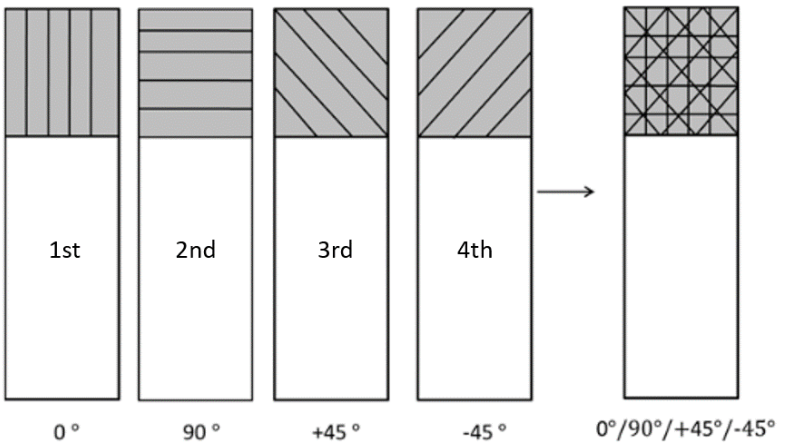

Figure 3.7: Path followed by the abrasion tool: 0^{o}, 90^{o}, $+45^{o}$, -45^{o}. Adapted from [144].

After each one of these mechanical abrasion processes, the specimen was cleaned with IPA, and compressed air was directed onto the overlap area to remove any loose material and excess of the solvent previously applied. This surface preparation was carefully performed with latex gloves, in order to avoid any recontamination of the specimens. For grit blasting, the machine utilized in this work was a RP-TOOLS 350L with extraction, as illustrated in Figure 3.8.

(a) (b)

Figure 3.8: Sandblast machine utilized in this work.

3.3.4 Polymer/Metal Specimens' Fabrication Processes

In here, the following methodology was pursued: the metallic substrate's surface started by being abraded, followed by the creation of an experimental apparatus and FFF of a polymeric substrate onto the metallic base material. Besides this, it will be described every existing difficulties and optimization process when trying to join dissimilar materials with FFF. Detailed methodology will be explained for each set of materials: Aluminium-ABS, Aluminium-Nylon and Aluminium-Nylon CF15, respectively.

Aluminium-ABS

As previously described, the base material had three types of surface treatment configurations. Inside these, we had another two types of manufacturing procedures: with and without primer's application.

Primer's importance in adhesion between two joints was already thoroughly emphasized before (Section 2.5) and validated above (Section 3.3.2). In here, the application and type of primer followed some manufacturing considerations from the study conducted by Falck et al. [13], a $25\ wt\%$ ABS solution, being:

$$wt\% = \frac{mass\ of\ solute}{mass\ of\ solution} \tag{3.1}$$

And acetone as the solvent. The preparation of this solution is detailed below:

- **Determination of the solvent's mass:**
  - $V_{acetone} = 50\ mL$
  - $\rho_{acetone} = 789.2\ \frac{kg}{m^3}\ (T = 21°C)$

$$\rho = \frac{m}{V} \tag{3.2}$$

$$m_{acetone} = \rho * V = 789.2\,\frac{kg}{m^3} * 5.0 * 10^{-5}\,m^3 \Leftrightarrow m_{acetone} = 39.46\,g \tag{3.3}$$

- **Determination of the solute's mass:**
  - $m_{acetone} = 39.46\,g$
  - $25\,wt\%$
  - $\rho_{ABS} = 1010.0\,\frac{kg}{m^3}\,(T = 21°C)$

$$0.25 = \frac{m_{ABS}}{m_{ABS} + 39.46} \Leftrightarrow m_{ABS} = 13.15\,g \tag{3.4}$$

- **Determination of the length of polymer's filament needed**
  - $m_{ABS} = 13.15\,g$
  - $\rho_{ABS} = 1010.0\,\frac{kg}{m^3}\,(T = 21°C)$
  - $1.75\,mm$ filament's diameter
  - $h =$ filament's length

$$V_{ABS} = \frac{m_{ABS}}{\rho_{ABS}} \Leftrightarrow V_{ABS} = 13022.77\,mm^3 \tag{3.5}$$

$$V_{ABS} = \pi * \frac{d^2}{4} * h \Leftrightarrow \textbf{h = 5.26 m} \tag{3.6}$$

- **ABS Mix**
  1. Cut the determined filament's length in smaller portions ($5\,mm$ each), Figure 3.9 (a);
  2. Mix it with $50\,mL$ of acetone in a glass container;
  3. Rest for $24\,hours$, Figure 3.9 (b).

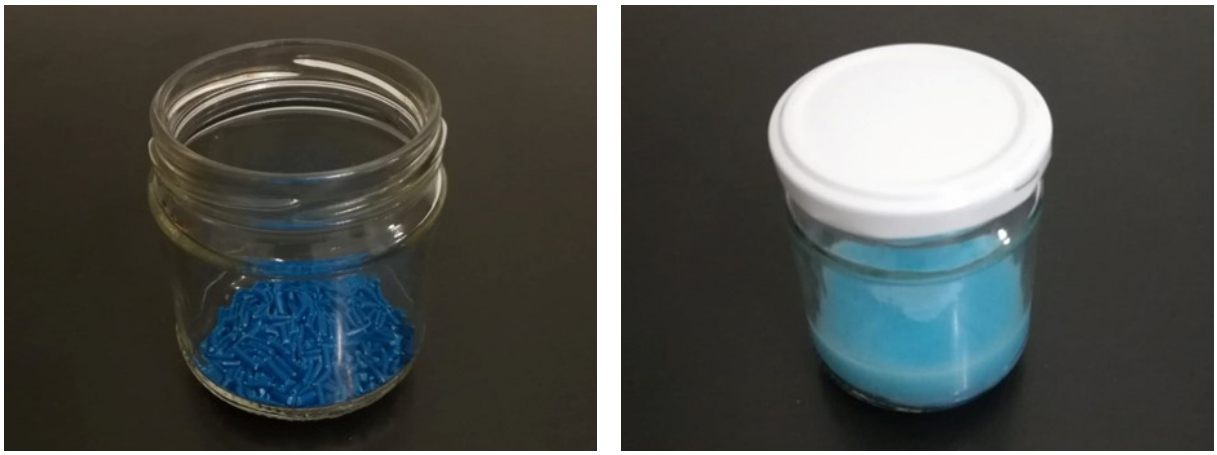

(a) (b)

Figure 3.9: Illustration of ABS solution preparation. (a) Small portions of ABS filament cutted and (b) mixed with acetone.

Regarding other variables, Falck et al. [37] had already determined the optimized manufacturing parameters for ABS and Aluminium 2024-T3 single-lap joints. In here, the same procedure was followed with differences in base material's surface treatments and primer's fabrication. Original article only studied the adherence of surface treated Aluminium with grit blasting technique and primer application. This thesis studied the adhesion of the same materials without surface abrasion, abraded by sandpaper and without primer's application, as previously mentioned. In here, the standard procedure is described at length.

- **Manufacturing procedure:**

  1. Base material's surface preparation;
  2. ABS primer solution's application, as illustrated in Figure 3.10:
     - $0.25\,mL$ applied on top of the overlap area with a syringe;
     - Carefully spread all over the surface using a brush;
     - Dried at horizontal position for $5\,min$, at ambient temperature.

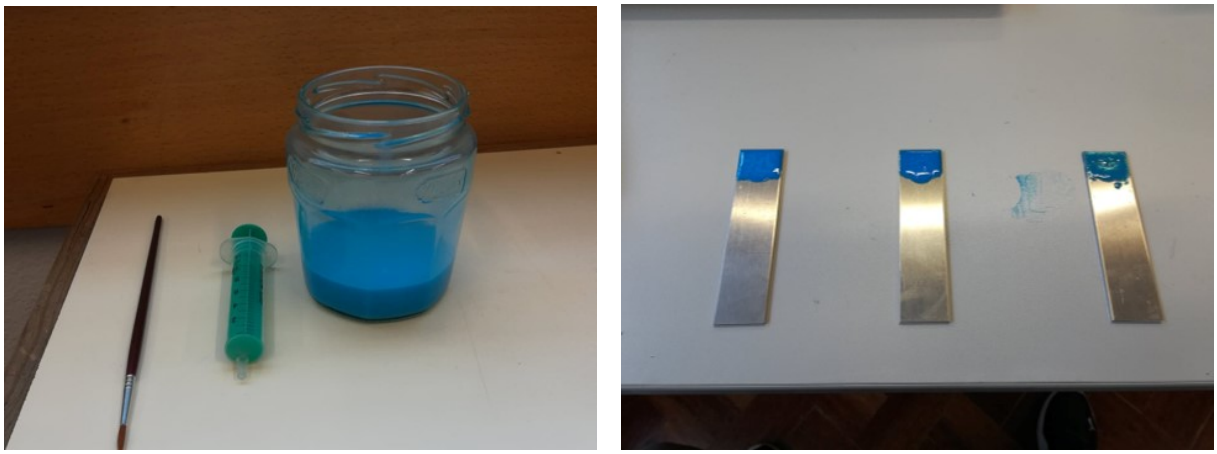

(a) (b)

Figure 3.10: (a) ABS primer's application tools and (b) three examples of base material with primer applied.

3. Build plate masked with Kapton tape;
4. Attachment of the base material to the build plate's slot, as illustrated in Figure 3.11 (a);
5. Selection of the *.stl* file with following parameters:
   - Printing temperature = $280°C$
   - Bed temperature = $110°C$
   - Deposition speed = $50\ mm/s$
   - Raster thickness = $0,1\ mm$
   - Number of contours = 12
6. Start of the FFF;
7. Time span = $54\ minutes$ and $17\ seconds$;
8. End of the FFF;
9. Waiting time before the build plate reaches the ambient temperature;
10. Carefully removal of the hybrid joint from the build plate;
11. Identification and storage of the specimen inside a low-humidity cabinet, as illustrated in Figure 3.11 (b).

- **Notes:**
  - To validate the theory of a maximum adhesion strength for a coating/primer's thickness of $0.1\ mm$, it was required to assure this measure for ABS primer's application. Although imprecise, the quantity of $0.25\ mL$ was obtained from trial and error experimentation and validated by caliper gauge's measurements.
  - At the time of the experiment, the ambient temperature inside the laboratory was $22°C$.

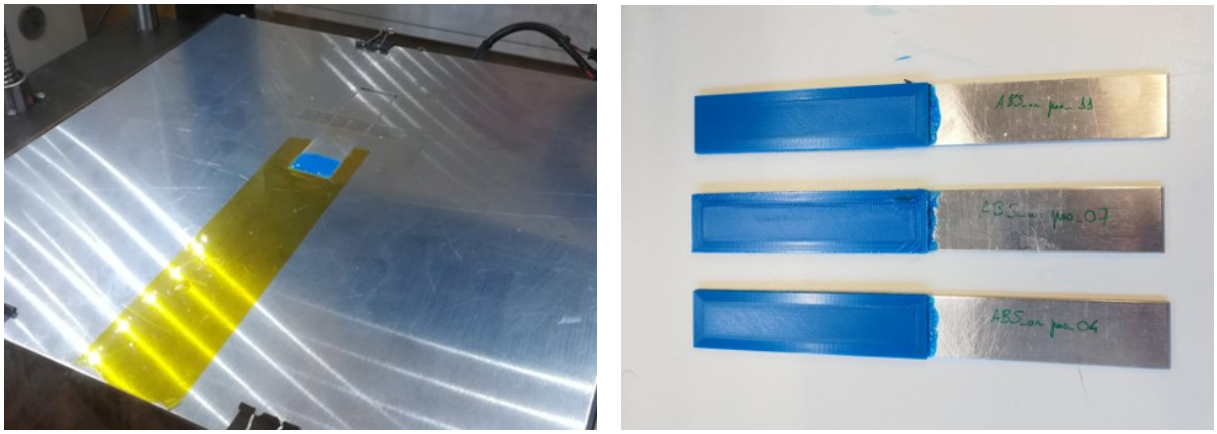

(a) (b)

Figure 3.11: (a) Attachment of ABS specimen's base material and (b) final specimen.

Aluminium-Nylon

The previous experience with ABS showed us the importance of a primer in guaranteeing adhesion between a polymer and a metallic substrate in FFF. At this point, this knowledge was already cemented, but it was required another technique for it, since Nylon does not dissolve in acetone as ABS does. Also, Falck et al. [13] had already done the experiment with Nylon and continuous carbon fiber on top of a metallic substrate and successfully validated the technique of printing a $0.2\ mm$ primer layer on top of base material's overlap area (13 x $26\ mm^2$), before printing the entire top adherend.

Giving so, it was interesting to experiment the same technique with Nylon only. Later, the results of these specimens' validation tests are compared with Nylon CF15's. To denote that, contrarily to Falck et al.'s article [13], the primer's thickness used in this work was equal to $0.1\ mm$, due to evidence of this measure with a stronger adhesion bond (Section 2.5).

Nylon's filament used in this work was from *Markforged* manufacturer. Contrarily to manufacturer's machines, non-open source 3D printers, Raise3D and *Ideamaker* software enable us to change fabric's printing parameters: printing temperature = $270°C$, deposition speed = $40\ mm/s$ and raster thickness = $0.125\ mm$. The manufacturing procedure for these specimens is thoroughly described below, with some detailed aspects given after.

- **Manufacturing procedure:**

  1. Base material's surface preparation;
  2. Nylon primer's printing, as illustrated in Figure 3.12 (a):
     - Printing temperature = $270°C$
     - Bed temperature = $110°C$
     - Deposition speed = $45\ mm/s$
     - Raster thickness = $0.1\ mm$
     - Number of contours = 12
  3. After printed, rest until ambient temperature;

4. Base material's removal;
5. Primer's remelting (identical to Nylon CF15's):
   - Placement of the base material on top of an electric hot plate;
   - Heating of the specimen until it reaches $270°C$;
   - Heating time of $1\ min$;
   - Removal of the base material and resting time of $2\ min$.
6. Attachment of the base material to the build plate's slot;
7. Build plate masked with BMT;
8. Selection of the *.stl* file with following parameters:
   - Printing temperature = $270°C$
   - Bed temperature = $110°C$
   - Deposition speed = $45\ mm/s$
   - Raster thickness = $0.1\ mm$
   - Number of contours = 12
   - Brim loop lines = 25
9. Start of the FFF;
10. Time span = $1\ hour,\ 4\ minutes$ and $43\ seconds$;
11. End of the FFF;
12. Waiting time before the build plate reaches ambient temperature;
13. Careful removal of the hybrid joint from the build plate, as illustrated in Figure 3.12;
14. Removal of the brim with a box cutter;
15. Identification and storage of the specimen inside a low-humidity cabinet.

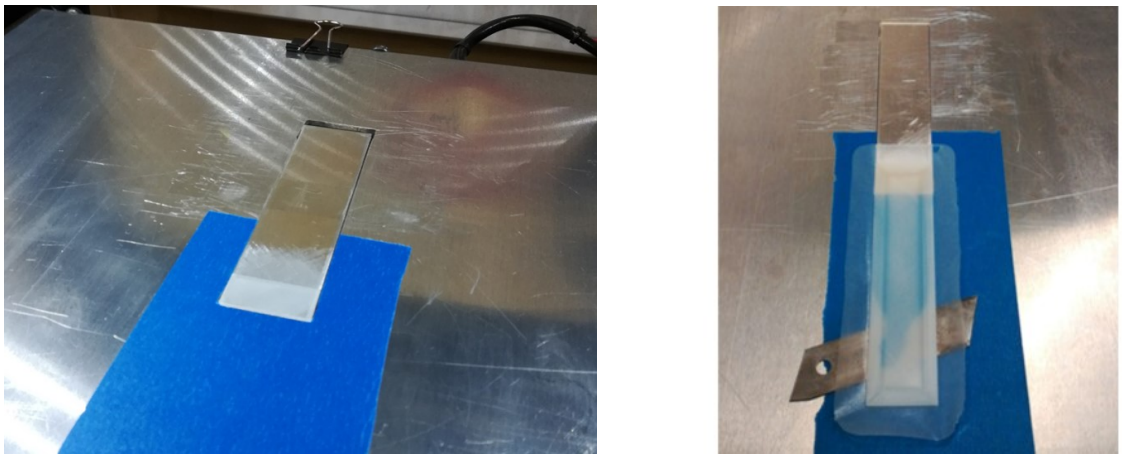

(a) (b)

Figure 3.12: (a) Nylon specimen's coating printing and (b) removal from the build plate.

- **Notes:**
  - Before turning on the machine, Nylon's spool filament is stored inside a dehumidifier heated cabinet for $45\ minutes$, given its moisture absorption's rate.
  - When remelting the base material's primer, the polymer flows easier into the metallic substrate surface irregularities. Then, it enhances the adhesion strength between primer and base material.
  - Similarly to ABS setup, it was necessary to assure a minimal adhesion of the printed polymer to the customized build plate, along an easier removal after its temperature reached ambient levels. So, it was helpful to use a blue masking tape on top of the build plate [145], as illustrated in Figure 3.12. This tape has a rough surface, which increases the surface area with the molten area and, consequently, adhesion between both.

Aluminium-Nylon CF15

Besides surface roughness' influence in adhesion between two dissimilar materials, literature review had already found evidence on fiber's relevance too (Section 2.2). In order to test the relevance of both parameters, Nylon CF15 filament was used and compared with Nylon's test specimens.

As previously stated, Falck et al. [13] had already concluded about the influence of continuous carbon fibers in the increase in strength of single-lap joints fabricated from a similar process. Nylon CF15 is not made from continuous carbon fibers. Instead, there are milled ones within the polyamide matrix. This was interesting because, not only it increased FFF component's mechanical properties, there was previous evidence of its adhesion enhance with surface roughness' changed base material.

The manufacturing procedure was in many ways similar to Nylon's (including primer's printing and remelting technique). Although, its printing parameters were slightly different, given manufacturer's recommendations [141]. Also, the presence of carbon fibers increases nozzle's wear, so the original component was changed by a hardened steel one. In here, the whole process is extensively described.

- **Manufacturing procedure:**
  1. Base material's surface preparation;
  2. Nylon CF15 primer's printing, as illustrated in Figure 3.13 (a):
     - Printing temperature = $260°C$
     - Bed temperature = $110°C$
     - Deposition speed = $30\ mm/s$
     - Raster thickness = $0.1\ mm$
     - Number of contours = 12
  3. After printed, rest until ambient temperature;
  4. Base material's removal;
  5. Primer's remelting, as illustrated in Figure 3.13 (b);

- Placement of the base material on top of an electric hot plate;
- Heating of the specimen until it reaches $260°C$;
- Heating time of $1\ min$;
- Removal of the base material and resting time of $2\ min$.

(a) (b)

Figure 3.13: (a) Nylon CF15 specimen's coating printing and (b) remelting on top of a hot plate.

6. Build plate masked with BMT;
7. Attachment of the base material to the build plate's slot;
8. Selection of the *.stl* file with following parameters:
   - Printing temperature = $260°C$
   - Bed temperature = $110°C$
   - Deposition speed = $30\ mm/s$
   - Raster thickness = $0.1\ mm$
   - Number of contours = 12
   - Brim loop lines = 45
9. Start of the FFF;
10. Time span = $1\ hour, 29\ minutes$ and $17\ seconds$;
11. End of the FFF;
12. Waiting time before the build plate reaches ambient temperature, as illustrated in Figure 3.14 (a);
13. Careful removal of the hybrid joint from the build plate;
14. Removal of the brim with a box cutter;
15. Identification and storage of the specimen inside a low-humidity cabinet; final specimen illustrated in Figure 3.14 (b).

(a) (b)

Figure 3.14: (a) Nylon CF15 specimen's resting time after printing and (b) after removal of the brim.

- **Notes:**
  - Before turning on the machine, Nylon CF15's spool filament is stored inside a dehumidifier heated cabinet for $45\ minutes$, given its moisture absorption's rate.
  - When remelting the base material's primer, the polymer flows easier into the metallic substrate surface irregularities and increases the probability of fibers' infiltration in it. Then, it enhances the adhesion strength between the primer and the base material.

Table 3.6 identifies each specimen, given its combination of materials, abrasion type and primer's fabrication processes.

Table 3.6: Review of every manufactured joint.

ID	Materials	Abrasion Type	Primer's Fabrication Process
1a	Al-Nylon	Sandpaper	FFF
1b	Al-Nylon	Sandpaper	FFF
1c	Al-Nylon	Sandpaper	FFF
1d	Al-Nylon	Sandpaper	FFF
1e	Al-Nylon	Sandpaper	FFF
2a	Al-Nylon CF15	Sandpaper	FFF
2b	Al-Nylon CF15	Sandpaper	FFF
2c	Al-Nylon CF15	Sandpaper	FFF
2d	Al-Nylon CF15	Sandpaper	FFF
2e	Al-Nylon CF15	Sandpaper	FFF
3a	Al-ABS	Sandblasting	Manual
3b	Al-ABS	Sandblasting	Manual
3c	Al-ABS	Sandblasting	Manual
3d	Al-ABS	Sandblasting	Manual
3e	Al-ABS	Sandblasting	Manual
4a	Al-Nylon	Sandblasting	FFF
4b	Al-Nylon	Sandblasting	FFF
4c	Al-Nylon	Sandblasting	FFF
4d	Al-Nylon	Sandblasting	FFF
4e	Al-Nylon	Sandblasting	FFF
5a	Al-Nylon CF15	Sandblasting	FFF
5b	Al-Nylon CF15	Sandblasting	FFF
5c	Al-Nylon CF15	Sandblasting	FFF
5d	Al-Nylon CF15	Sandblasting	FFF
5e	Al-Nylon CF15	Sandblasting	FFF

3.3.5 Optical Profilometry

In the wake of comparing the different surface treatments and its effects on the lap-shear strength of the PMH joints, an optical profilometry measurement was done on the top surface of the base material. The profilometry measurements based on the white light interferometry method were performed on the profilometer Profilm 3D with a 20X objective. The surface scanned area was 1.0 x $0.85\ mm^2$. The raw data was acquired using the envelope peak analysis. The raw data files were exported and post–processed with the software *Profilm Online*. The average surface roughness (R_a) and the maximum surface roughness (R_z) of the base material's top surface were determined considering the entire scanned area for both abraded and non abraded samples. For each experimental condition, three coordinates representative of the Aluminium surface were considered and its values determined, as shown in Section 4.1.

Profilm Online software was utilized for post-processing of optical profilometry's raw data. For each coordinate, surface roughness' analysis was performed along three different directions: vertical, horizontal and diagonal. Then, for each direction, roughness' values, R_a and R_c, were measured from three different positions and averaged afterwards. In here, R_a is the arithmetic mean deviation $[\mu m]$ and R_c the average peak to valley height $[\mu m]$, which is calculated from every peak to valley heights within the sample length, R_{z_i} $[\mu m]$.

3.3.6 Optical and Scanning Electron Microscopy

A Scanning Electron Microscope (SEM) and an Energy Dispersive Spectroscopy (EDS) analysis were conducted to characterize the base material. A slice of the material was cut and fixed in a resin structure. After it had cured, the base material's surface was polished with traditional sandpapers and silicon carbide sandpapers for final finishing. Then, the surface was etched with a solution of ferric chloride to expose its microstructure and analysed by SEM.

Considering PMH specimens, a microscopy test was performed to evaluate primer's thickness for each type. Three specimens were chosen from sandpaper's abraded batch, one for each polymer used. For ABS test, primer's was manufactured by hand, whereas for Nylon and Nylon CF15, its corresponding primers were manufactured by FFF and its thickness determined by the *.stl* file. Then, it was expected higher discrepancies from the ideal primer's thickness of $0,1\ mm$ coming from ABS than the other two.

The setup of the specimens in a resin matrix was previously explained when evaluating Aluminium base material by SEM. Then, it was fixed to a laboratory magnifying glass linked to a digital camera and each primer's thickness evaluated. The camera took a picture of each sample and measured the distance between two points on top of primer's borderlines.

3.3.7 Mechanical Tests

The mechanical properties of the base material: ultimate tensile strength (σ_{UTS}), yield stress (σ_y), Young's Modulus (E) and elongation at break (ε_F) were determined by uniaxial tensile tests. An INSTRON 3369 universal testing machine with a $50\ kN$ load cell and a crosshead speed of $1.0\ mm/min$ was used. Three specimens were machined and tested following the ASTM E8/E8M $-$ 13a standard [146].

Along this, a microindentation hardness test conducted on a Shimadzu HMV$-$2 microhardness tester (illustrated in Figure 3.15 (a)) was performed to evaluate base material's Vickers Hardness (VH) according to the ASTM E384$-$17 standard [147]. The top surface of the base material was polished by a P120 Bosch sandpaper and any existing loose particles were removed by compressed air. The indenter applied a force of $1.961\ N$, during $10\ s$, at 10 different locations of each sample. The distance between each indentation was, at least, $2.5\ dV$, in which dV stands for the length of an indentation's diagonal, as represented in Figure 3.15 (b).

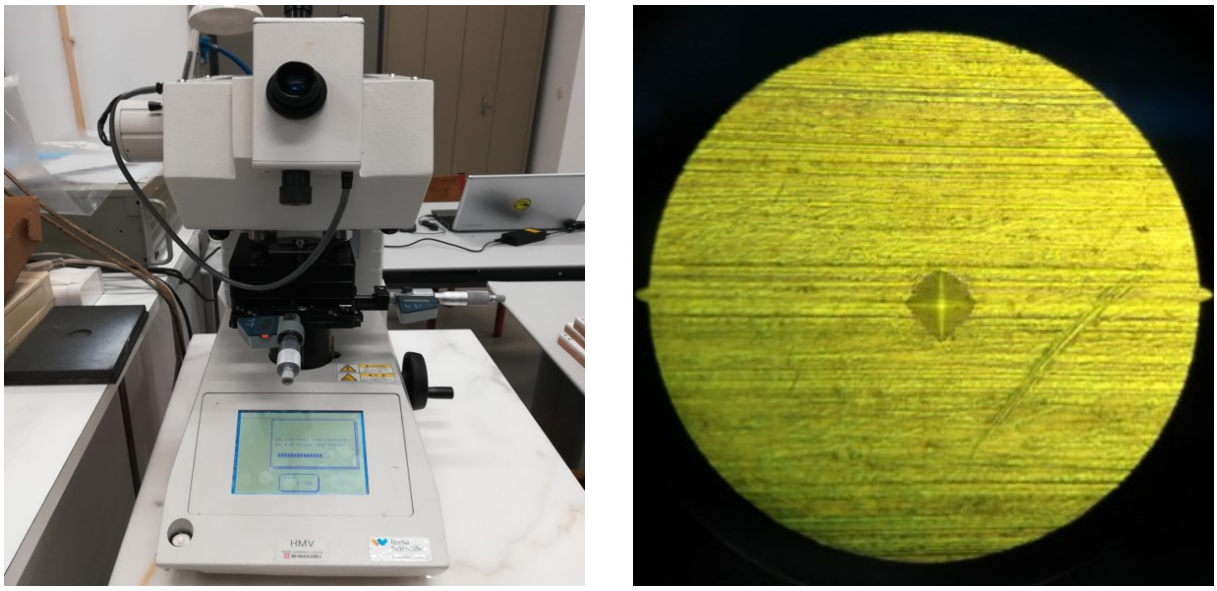

(a) (b)

Figure 3.15: (a) Microhardness testing machine Shimadzu HMV$-$2 and (b) Vickers indentation's illustration taken from the performed test.

Additionally, to quantify the strength of these FFF hybrid joints, a single-lap tension loading test was performed in an INSTRON 3369 tensile test machine with a $50\ kN$ load cell and a crosshead speed equal to $1.27\ mm/min$, as illustrated in Figure 3.16. It was adapted from ASTM D3163 standard test method for determining strength of adhesively bonded rigid plastic lap-shear joints in shear by tension loading [130].

(a) (b)

Figure 3.16: Tensile loading test of a Nylon CF15 sample.

Given the design of such specimens (Section 3.1), it was important to prevent the characteristic bending effect of single-lap joints subjected to tension loading. For this, two pieces of the same Aluminium sheet as the base material were placed between the testing machine's grips and specimen's adherends. Thus, the line of action of the force applied was aligned with both surfaces of the adherends.

Chapter 4

Results and Discussion

In this chapter, the following is described: an optical profilometry's analysis for each abrasion mode, the mechanical characterization of the base material, the mechanical characterization of the PMH single-lap joints with some remarks regarding surface's roughness and fibers' influence on them, ending with the fracture's surface observation and analysis. The obtained results in this work will be compared with the previous reported results in literature for PMH single lap joints produced by FFF.

4.1 Optical Profilometry's Analysis

Figures 4.1 (a), 4.2 (a) and 4.3 (a) show the optical profilometry's top view for each surface condition, whereas Figures 4.1 (b), 4.2 (b) and 4.3 (b) present a 3D view of the same scan.

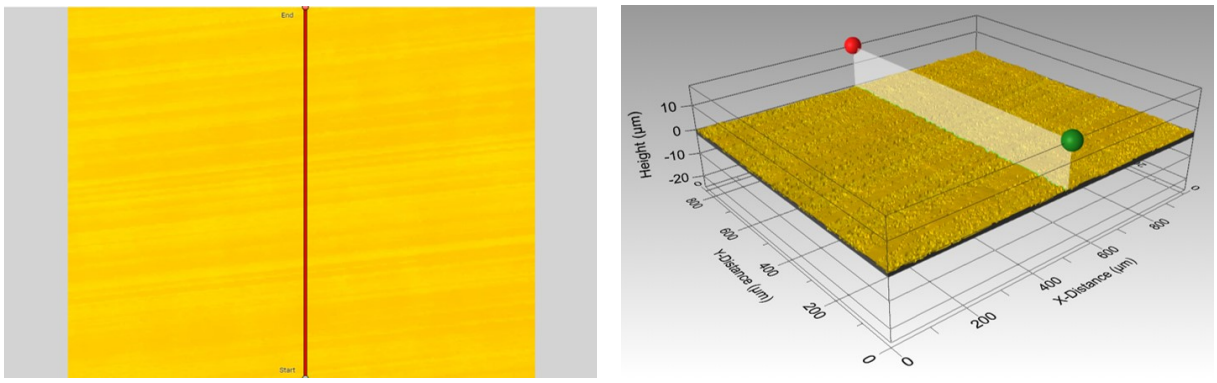

(a) (b)

Figure 4.1: Optical profilometry's analysis of a non-abraded base material's overlap area, (a) top view and (b) 3D view.

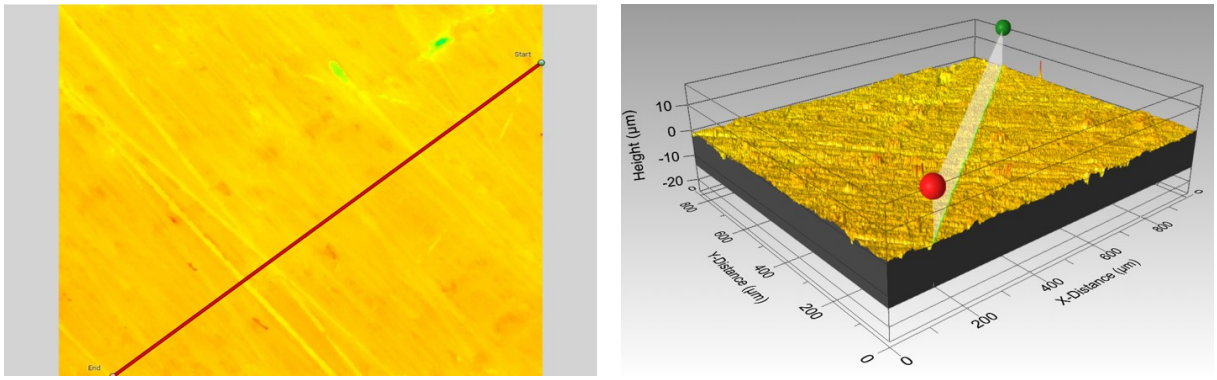

(a) (b)

Figure 4.2: Optical profilometry's analysis of a base material abraded by P120 sandpaper, (a) top view and (b) 3D view.

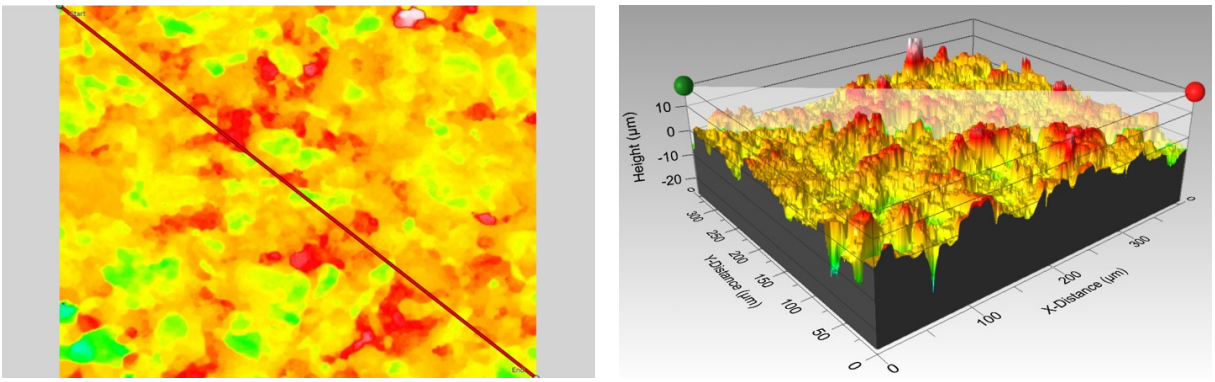

(a) (b)

Figure 4.3: Optical profilometry's analysis of a base material abraded by grit blasting, (a) top view and (b) 3D view.

When analysing previously mentioned figures, it can be drawn a visual surface's treatment comparison. In fact, optical profilometry revealed more irregularities in non-abraded and grit blasted surfaces, comparing with that abraded by P120 sandpaper. Sandpaper's utilization contributed to a homogenization of the non-abraded surface, however increasing its surface's roughness. Visually sharp peaks were turned into rounded shaped ones with deeper valleys, as illustrated in Figures 4.1 (b) and 4.2 (b). Also, in Figure 4.2 (a), it can be noted the lack of noticeable valleys in every direction followed by sandpaper's abrasion method, as shown in Section 3.3.3. As foreseen before, the poor pressure control of that procedure revealed a higher disparity in valley's distribution along analysed surface, in comparison with the resultant amorphous distribution in grit blasted surface, as shown in Figures 4.2 and 4.3.

The same figure shows an exceptionally degree of abrasion for grit blasting technique, when compared with non-abraded and P120 sandpaper's treatment. It is also noticeable the rounded shapes of its valleys and, as seen in the non-abraded surface, an unequally distributed roughness' profile, as illustrated in Figure 4.3 (b). 3D view provides a greater look into the vast material's removal in here, resultant from the shock of corundum particles onto the base material's surface.

Adding to this qualitative analysis, *Profilm Online* also presents a 2D surface roughness profile, a quantitative view of roughness' values along the sampling length, as illustrated in Figures 4.4, 4.5 and 4.6, for the non-abraded specimen, the one abraded by P120 sandpaper and the one abraded by grit blasting technique, respectively. In here, the conclusions stated above can also be drawn regarding the effect of each surface's treatment in its roughness. The specimen abraded by sandpaper reveals a clear homogenization of its surface profile when comparing with the non-abraded specimen. Again, this result does combine with higher roughness' height, comparing the values presented in Figures 4.4 and 4.5.

When moving to Figure 4.6, a 2D surface roughness profile of the grit blasted specimen, there is a noticeable increase in profile's height, adding to a return of the disorganized peaks and valleys also found in non-abraded specimens. In all diagrams, both R_a and R_{z_i}, the height of a i^{th} element within the sampling length, are illustrated.

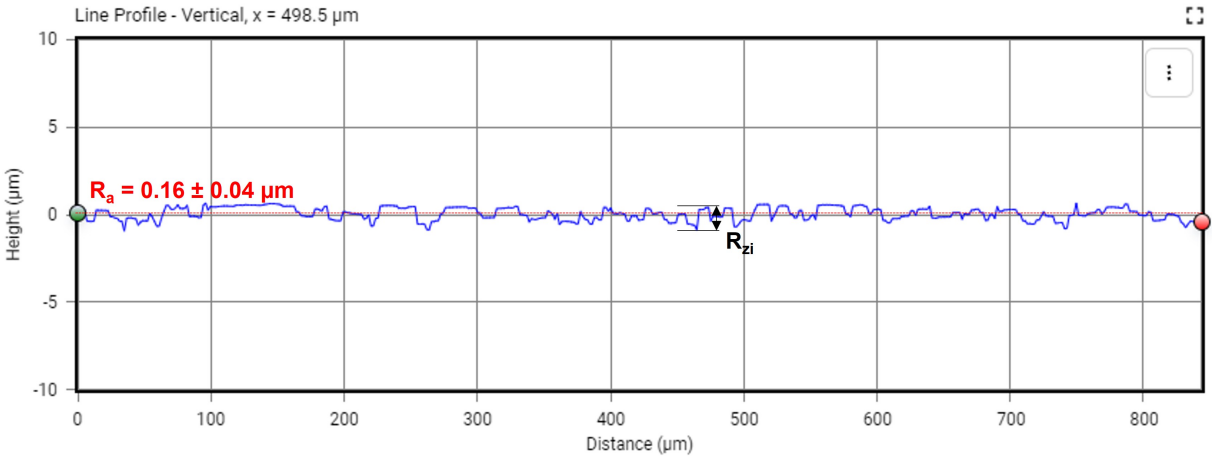

Figure 4.4: 2D surface roughness profile of a non-abraded base material's overlap area.

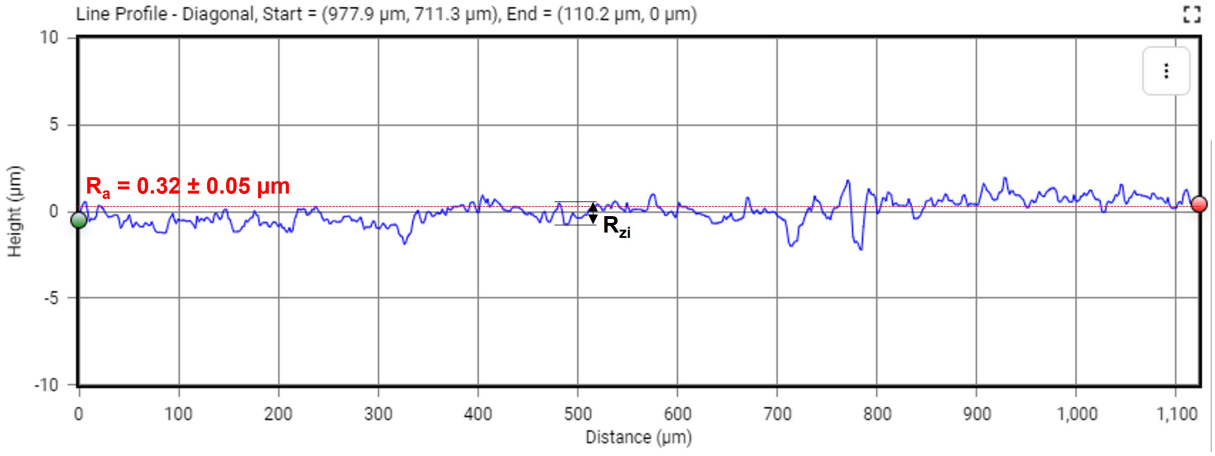

Figure 4.5: 2D surface roughness profile of a base material abraded by P120 sandpaper.

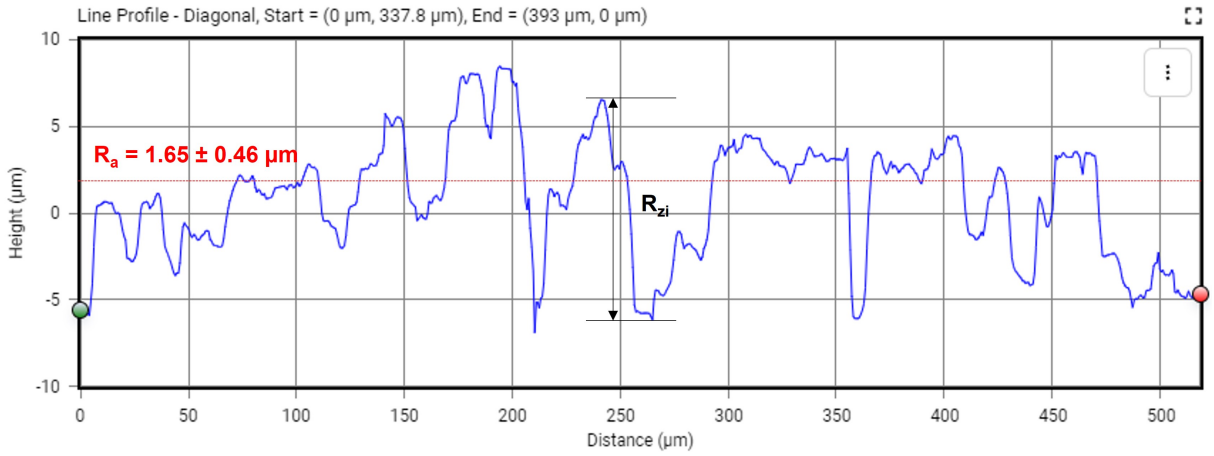

Figure 4.6: 2D surface roughness profile of a base material abraded by grit blasting.

Finally, for each base material's surface condition, the measured surface roughness values, R_a and R_c are given in Table 4.1. It is noteworthy the increase for both roughness' parameters when going from sandpaper's abrasion to grit blasting, a conclusion already done by previous studies (Section 2.4).

Table 4.1: Surface roughness measurements R_a and R_c values of Aluminium adherend after surface treatment.

Surface Treatment	$\mathbf{R_a}[\mu\mathbf{m}]$	$\mathbf{R_c}[\mu\mathbf{m}]$
Non-abraded	0.16 ± 0.04	0.58 ± 0.12
Abraded by P120	0.32 ± 0.05	1.12 ± 0.22
Abraded by grit-blasting	1.65 ± 0.46	6.20 ± 1.67

4.2 Optical and Scanning Electron Microscopy's Analysis

In here, the results of the tests described in Section 3.3.6 for the primer's thickness validation and the characterization of base material are presented and illustrated in Figures 4.7 and 4.8.

From optical microscopy's, a distance of $0,125\ mm$ was measured from Nylon and Nylon CF15's primer, a 25% variance from the programmed $0,1\,mm$. Although high, previous research did not find this thickness problematic for adhesion purposes. ABS primer's thickness was impossible to measure.

(a) (b) (c)

Figure 4.7: Primer's optical microscopy of (a) ABS, (b) Nylon and (c) Nylon CF15 specimens.

An insufficient etching of the exposed surface might be the cause of the poor contrast observed in Figure 4.8 (a), revealing it impossible to distinguish between each element's domain, as explained by the laboratory's technician. The EDS spectra shown in Figure 4.8 (b) shows a proximity between each element energy levels, making it very hard to properly identify the microstructure of the base material. It only shows a probable existence of magnesium inclusions ($1.12\ wt\%$) within the Aluminium domain.

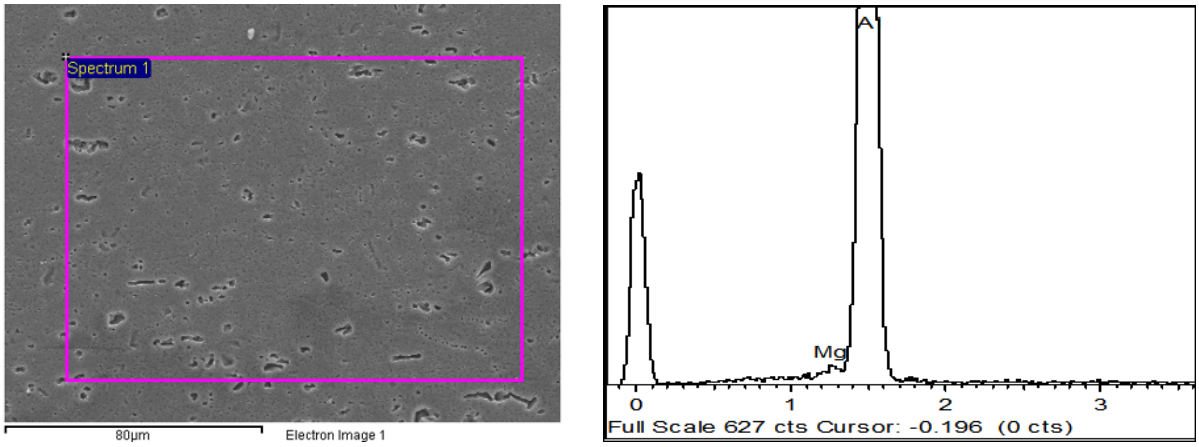

(a) (b)

Figure 4.8: (a) SEM micrography analysis and (b) EDS spectra of the base material.

Furthermore, SEM's analysis was also conducted in the same specimens, trying to measure fibers' infiltration in base material surface's irregularities and primer's thickness, Figure 4.9, but its results were inconclusive.

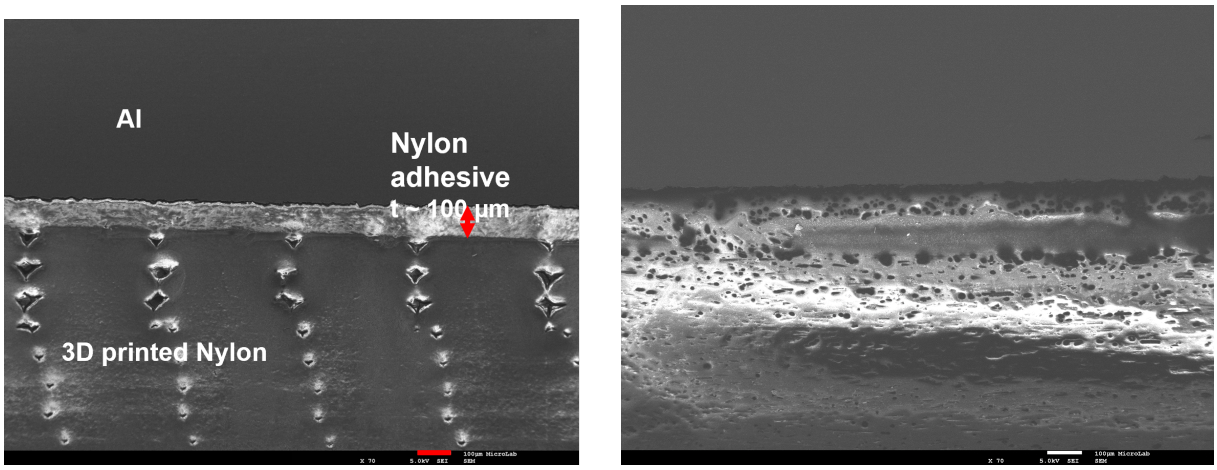

(a) (b)

Figure 4.9: SEM's analysis of (a) Nylon specimens, in which it may be observed the air gaps between printed rasters and (b) Nylon CF15 inconclusive observation.

4.3 Mechanical Test's Analysis

4.3.1 Base Material's Mechanical Characterization

Section 3.3.7 described the mechanical tests performed to the base material's characterization specimens: tensile loading tests and VH test, respectively. Following above mentioned tests, average hardness value of the base material was found to be equal to 127 (VH) and its remaining mechanical properties are presented in Table 4.2. These results, with SEM and EDS' analysis, suggest that the base material is part of the 5000 Aluminium alloy's series [148].

Table 4.2: Mechanical properties of our base material.

Specimen Nr.	$\sigma_{\mathbf{UTS}}$ [MPa]	$\sigma_{\mathbf{y}}$ [MPa]	E [GPa]	$\varepsilon_{\mathbf{F}}$ [%]
1	308.57	270.57	76.49	6.10
2	249.51	226.50	79.47	2.83
3	238.08	210.88	80.44	2.83
Average	265.38 $\pm$ 30.89	235.98 $\pm$ 25.27	78.8 $\pm$ 1.68	3.92 $\pm$ 1.54

4.3.2 Polymer/Metal Specimen's Mechanical Characterization

For the single-lap joints' mechanical characterization, five specimens were manufactured for each condition and tensile tests were performed to all. In Section 3.3.2, it was already demonstrated the impossibility of manufacturing Aluminium-ABS joints, previously abraded by sandpaper. Thus, this experiment's results do not appear in the following curves: Figures 4.10 to 4.14.

The shear stress-displacement curves are shown below, whereas the Ultimate Lap Shear Strength (ULSS) are shown further ahead in Table B.1, for sandpaper and grit blasting's abrasion techniques.

Figure 4.10 illustrates the behaviour of Aluminium-Nylon specimens previously abraded by sandpaper. Excluding Specimen 1e, there is a clear similarity between each curve's slope. The maximum shear stress achieved in here was $3.02\,MPa$. As stated before, the removal of the specimen from the build plate was not optimized. Given so, some specimens required a higher removal force than others. A result of that can be observed in Specimens 1a and 1d, in which a higher removal force translated in a lower ULSS of the joint. A higher temperature was applied to Specimen 1b when on top of the hot plate $(280°C)$ and it can be observed a decrease in elasticity's modulus, comparing with Specimens 1a, 1c and 1d. An opposite result was found for Specimen 1e, which was subjected to a lower temperature in the remelting phase.

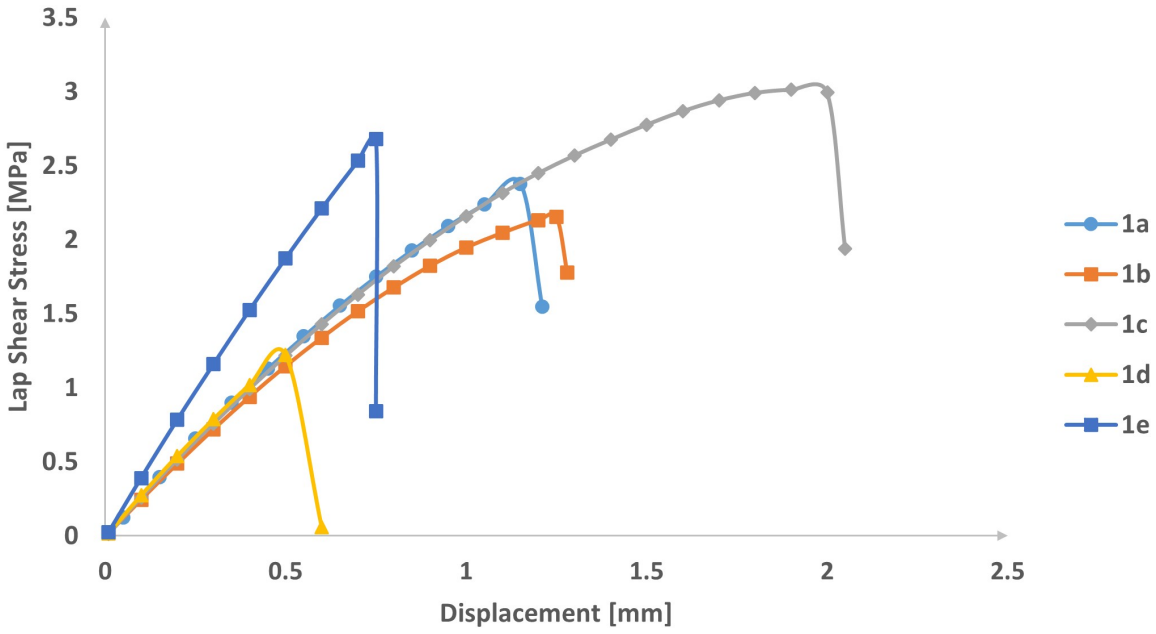

Figure 4.10: Aluminium-Nylon joints, previously abraded by sandpaper.

When analysing Aluminium-Nylon CF15 stress-displacement curves for sandpaper's abraded specimens, illustrated in Figure 4.11, it is obvious an increase of the maximum ULSS, comparing with Aluminium-Nylon specimens. Given so, Specimen 2b failed at a ULSS of $3.51\ MPa$. However, a higher disparity in results can be observed - a consequence of higher peeling stresses when removing the specimen from the build plate. In fact, an explanation for this might be an increased adherence of this polymer to the blue masking tape, possibly due to the presence of milled carbon fibers. The curves shown for Specimens 2a and 2d are the outcome of this.

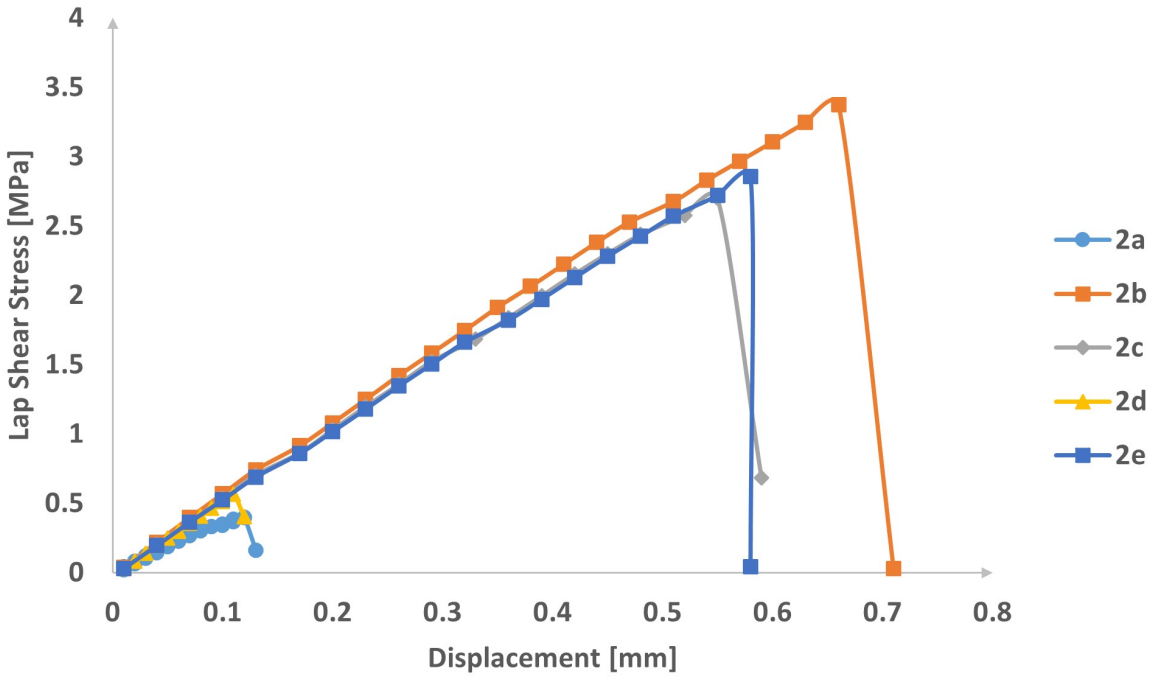

Figure 4.11: Aluminium-Nylon CF15 joints, previously abraded by sandpaper.

Figure 4.12 illustrates the results for Aluminium-ABS specimens treated with grit-blasting technique. Specimens 3a to 3d show similar results with an average ULSS of $0.99 \pm 0.08\ MPa$. To denote that these specimens were easier to remove from the build plate than those from previous experiments. Another conclusion for this type of hybrid joint was the outcome of Specimen 3e. It reached an ULSS of $1.92\ MPa$. A possible explanation is the longer resting time of this specimen after the conclusion of the print: it stayed on top of the build plate all night, instead of the usual one and a half hours of resting time until the build plate reached the ambient temperature. The longer time interval would increase the contraction of the polymer and an auto-separation from the build plate.

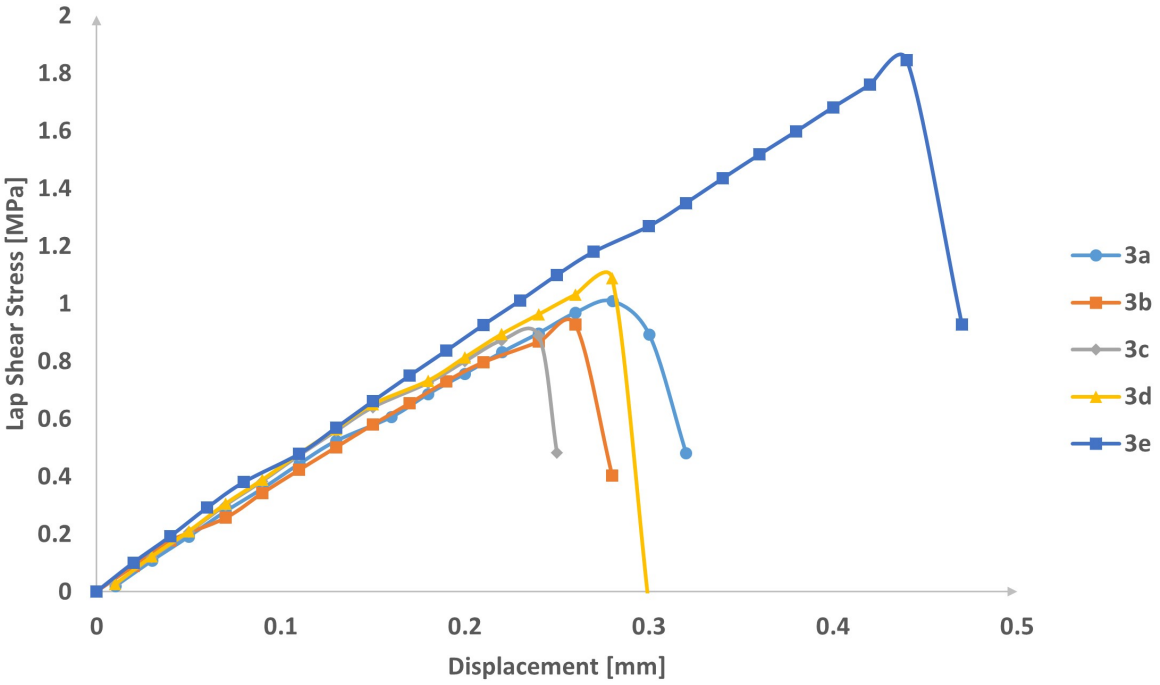

Figure 4.12: Aluminium-ABS joints, previously abraded by grit blasting.

This results contrast with the ones obtained by Falck et al. [13] for the same pair of materials, a maximum ULSS $= 5.3 \pm 0.3\ MPa$ for Aluminium-ABS joints. However, their study obtained an average peak to valley roughness, $R_c = 89.0 \pm 0.3\ \mu m$, contrasting with our $R_c = 6.20 \pm 1.67\ \mu m$. This variance might explain the greater ULSS achieved by them.

When examining the curves for Aluminium-Nylon specimens abraded with grit-blasting, Figure 4.13, one can conclude about the influence of Kapton tape's state in the removal force applied to the final specimens. A maximum value was reached by Specimen 4c, an ULSS of $4.34 MPa$. For this specimen, a new tape was previously applied on top of the build plate and the removal of the final piece was relatively easy. The same for Specimen 4a and 4e. Although, it can not be said the same for Specimens 4b and 4d, where an used tape cleaned with isopropyl alchohol was present. This tape has a polyimide film backing with a release agent that helps the removal of the specimen after it cools down. An explanation for the deterioration of the results is the elimination of the release agent by the isopropyl alcohol, which will harden the removal of the final piece.

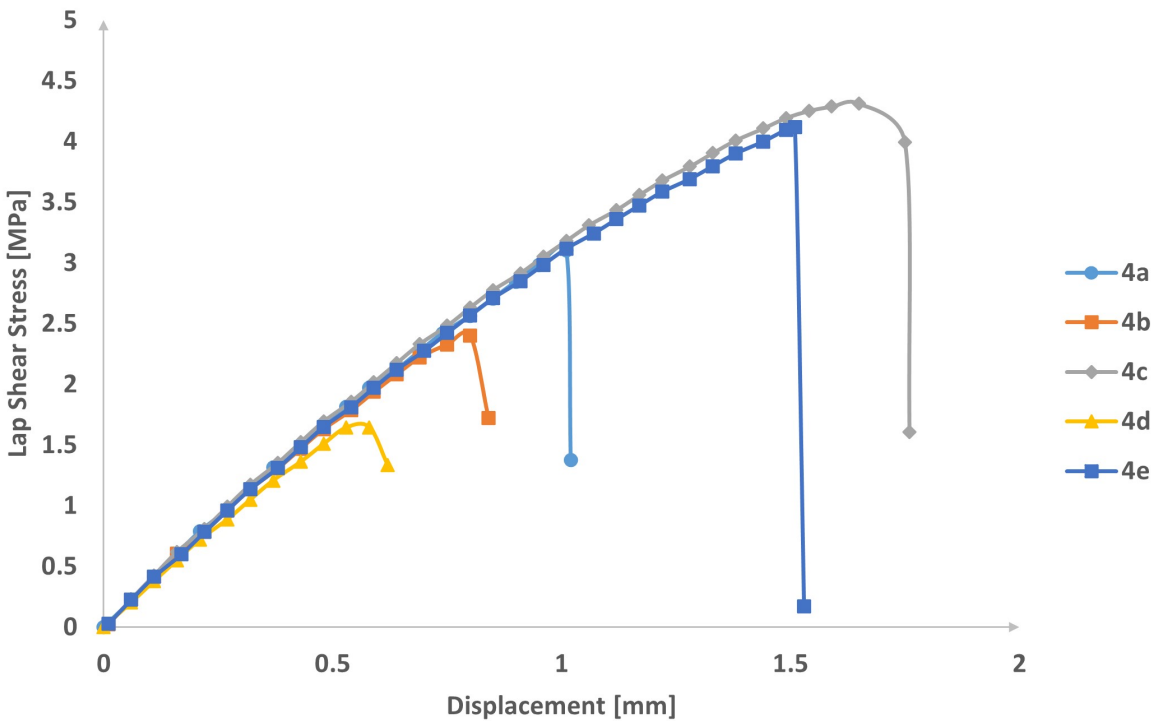

Figure 4.13: Aluminium-Nylon joints, previously abraded by grit blasting.

The final experiment reveals a maximum ULSS equal to $7.10\ MPa$, as illustrated in Figure 4.14, the maximum value obtained in this thesis. This test was the most consistent of them all, except for Specimen 5a, in which a damaged hot-end allowed the heat block to lower itself during printing, damaging the print and decreasing the thickness of the final part, possibly explaining the difference in the slope from the rest of the tested specimens. Poor performance of Specimen 5d was mainly due to the utilization of an used blue masking tape. Similarly to Kapton tape, this one has a wax-based release agent that allows to unroll the tape, but highly sensitive to chemical solvents such as isopropyl alcohol, which, again, was used to clean the surface of the build plate plus the masking tape. The elimination of this agent might have increased the required strength to remove the final printed specimen, affecting the stress resistance of the joint.

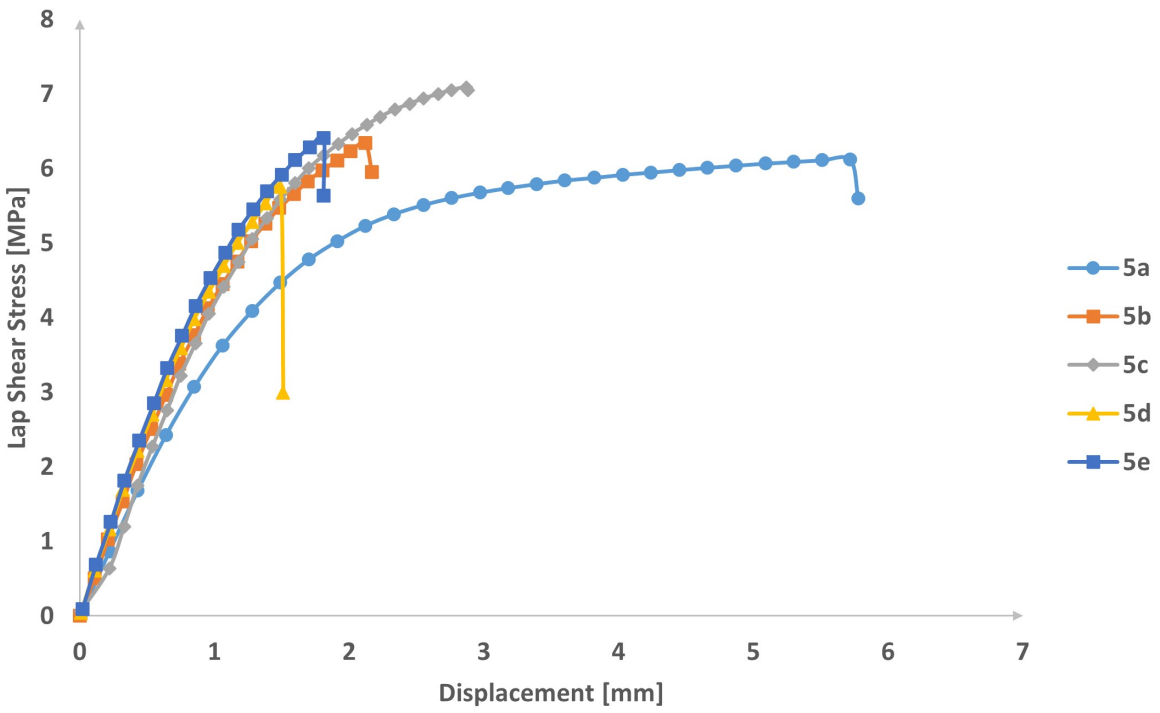

Figure 4.14: Aluminium-Nylon CF15 joints, previously abraded by grit blasting.

Aluminium-Nylon CF15's tensile loading results may be compared with others found by Falck et al. [13] for Aluminium with alternate layers of Nylon and Continuous Carbon Fibers. With an average peak to valley roughness $R_c = 89.0 \pm 0.3\ \mu m$, the tests conducted to these joints previously abraded by grit blasting resulted in an ULSS $= 21.9 \pm 1.1\ MPa$. The discrepancy found in these results may be explained by multiple factors: a larger surface profile was already mentioned has a vehicle for good adhesion among polymer/metal joints. The resource for continuous carbon fibers can also enhance the rigidity of the joint and elevate its ULSS.

Also, Boutar et al. [149] studied the effect of surface treatment on the shear strength of Aluminium adhesive single-lap joints for automotive applications [149]. For the non-abraded specimens, they measured similar roughness values to our sandpaper's abraded ones, in which we achieved an ULSS equal to $2.33 \pm 0.57\ MPa$ for Aluminium-Nylon specimens and $2.05 \pm 1.29\ MPa$ for Aluminium-Nylon CF15's ones, which are in line with Boutar's (an average ULSS equal to $2.92\ MPa$). Further along, the results found in this thesis for grit-blasting specimens can be compared with the ones found in theirs for P180 abraded specimens (an average ULSS equal to $3.52\ MPa$), where Aluminium-ABS specimens performed well below (ULSS $= 1.18 \pm 0.38\ MPa$), contrasting with similar values for Aluminium-Nylon's (ULSS $= 3.14 \pm 1.00\ MPa$) and better results for Aluminium-Nylon CF15 specimens (ULSS $= 6.36 \pm 0.43\ MPa$). Boutar's P180 specimens showed a $R_a = 1.5 \pm 0.14\ \mu m$. For Aluminium-ABS specimens, a lower result might be due to primer's application process and the nonexistence of a thermal post-processing of the metallic adherend prior to adhesion with ABS's top adherend.

In Appendix B, Table B.1 presents the ULSS (in MPa) for each tested specimen previously abraded by sandpaper ($R_a = 0.32 \pm 0.05\ \mu m$) and by grit-blasting ($R_a = 1.65 \pm 0.46\ \mu m$).

4.3.3 Surface's Roughness and Fibers Content Effect on ULSS

Table 4.3 show the correlation between shear strength and Aluminium's surface roughness when joining it with Nylon and Nylon CF15, respectively. For comparison purposes, only the maximum shear values obtained for each polymer are shown.

Table 4.3: Shear strength with respect to surface roughness value of Nylon and Nylon CF15 joints.

Surface Treatment	**Roughness**, $\mathbf{R_a}$ $[\mu\mathbf{m}]$	**ULSS** $[\mathbf{MPa}]$
Nylon		
Non abraded	0.16 $\pm$ 0.04	-
Abraded by sandpaper P120	0.32 $\pm$ 0.05	3.02
Abraded by grit-blasting	1.65 $\pm$ 0.46	4.34
Nylon CF15		
Non abraded	0.16 $\pm$ 0.04	-
Abraded by sandpaper P120	0.32 $\pm$ 0.05	3.51
Abraded by grit-blasting	1.65 $\pm$ 0.46	7.10

From Table 4.3, the Nylon's type specimen abraded by grit-blasting increased its single-lap shear strength by 43.71% with respect to the one abraded by sandpaper. Obviously, non-abraded specimens' shear strength was not considered due to the impossibility on successfully manufacture and test it.

In Table 4.3, Nylon CF15's shear strength results are shown with respect to its base material's surface roughness. In here, a 102.28% shear strength's increase was achieved for the specimen abraded by grit-blasting, in comparison with the one abraded by sandpaper.

These results come in agreement with the literature review previously done and shown in Section 3.3.3, which confirmed that an increase in surface roughness, particularly when resulting from grit-blasting technique, might enhance the mechanical interlocking effect between metallic mediums and polymeric materials, which contributed to higher adhesion strength.

Looking at fiber's content influence, other conclusions may be drawn. In fact, when comparing the same value for surface's roughness in Nylon and Nylon CF15, the last one prevails. As illustrated in Figure 4.15, however pertinent fibers' content might be, its full potential is only showed when some degree of surface's roughness exists. For specimens previously abraded by sandpaper, with an average surface's roughness, R_a equal to $0.32 \ \pm 0.05 \ \mu m$, Nylon CF15 specimens' single lap-shear maximum result was $3.51 \ MPa$, 16% more than the maximum value obtained for Nylon specimens. Moreover, when surface's roughness increases to a R_a equal to $1.65 \ \pm 0.46 \ \mu m$, after a grit-blasting treatment, the maximum ULSS of Nylon CF15 specimens overcome Nylon ones by 64%, with an ULSS equal to $7.10 \ MPa$ against $4.34 \ MPa$, respectively.

Comparing both variables, fibers' content appears to have a strong effect on adhesion strength between Aluminium and 3D printed polyamides, whereas Aluminium's surface roughness effect is only secondary. Along this, fibers' content also visually improved the quality of the print. Smoother surfaces were achieved when 3D printing with Nylon CF15, adding to less shrinkage on the final specimen once it cooled down. This shrinkage's decrease could also result in an increase on shear strength, as previous researches concluded that this shrinkage could lead to delamination of the polymer from the

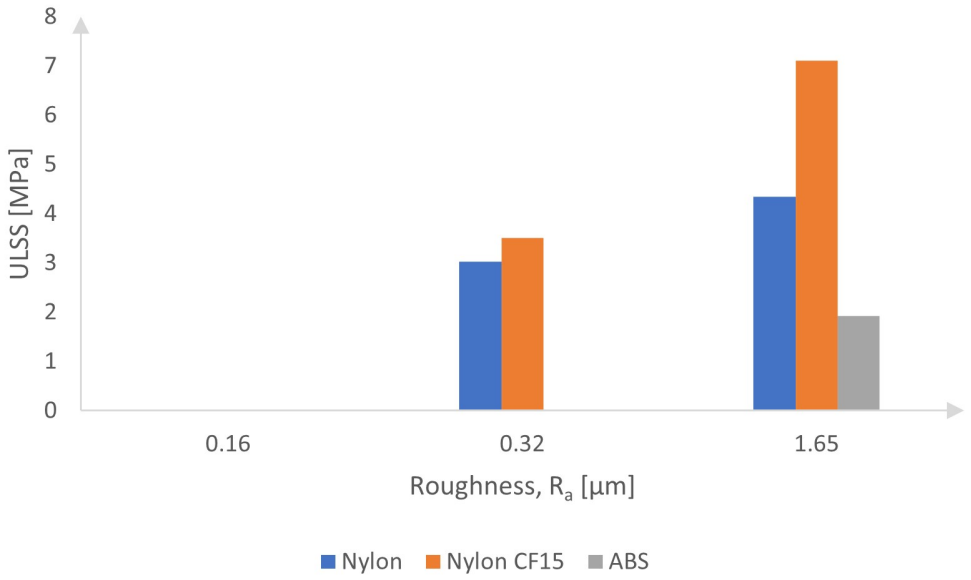

Figure 4.15: Surface's Roughness and Fiber's Content Effect on Shear Strength.

Aluminium [119].

4.4 Observation of Fracture's Surface

Observing fracture's surface, conclusions may be drawn about the quality of the corresponding joint, adding or contrasting to those obtained when analysing the mechanical test's results only. In here, each specimen's fracture surface is illustrated, along some detailed views of each fracture's type.

Figures 4.16 (a) and (b) illustrate sandpaper's abraded joints and the resulting fractured surface.

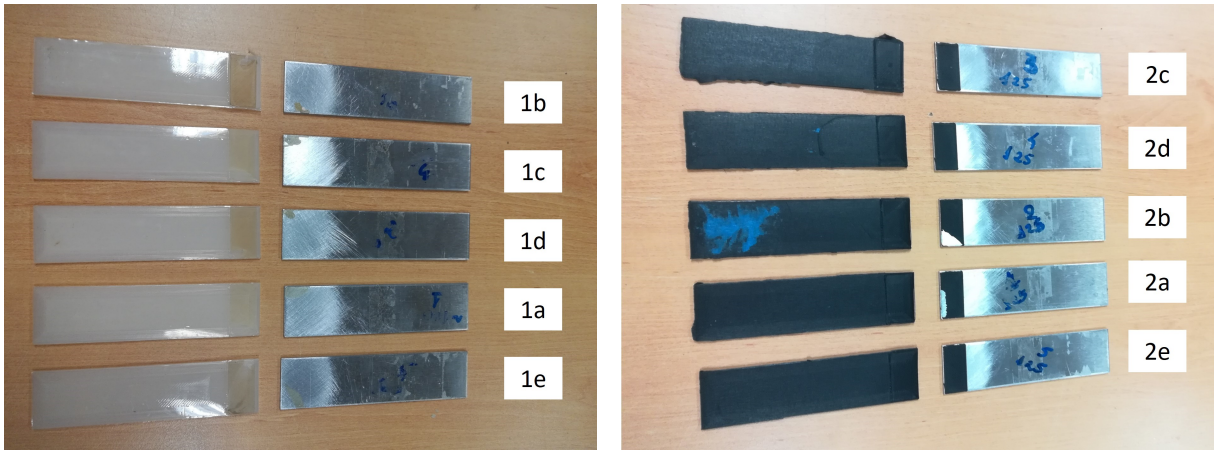

(a) (b)

Figure 4.16: Fracture's surface analysis of (a) Aluminium-Nylon and (b) Aluminium-Nylon CF15 specimens previously abraded by sandpaper.

Nylon specimens previously abraded by sandpaper show a fractured surface characteristic of a poor adhesion between both adherends. An adhesive failure mode is clearly defined, in which the adhesive is closer to the Nylon adherend. Then, the interlayer adhesion between each polymer was stronger than the polymer grip to the Aluminium's adherend, an indication of poor wetting of its surface.

Contrarily to Nylon, Figure 4.16 (b) shows the fractured surface for Nylon CF15 test specimens. A mixed adhesive/cohesive failure mode is shown in here, but mainly cohesive. Nylon CF15's coating is strongly adhered to the Aluminium's adherend, however partly joined to polymer's adherend as well. Previously described mechanical results show what is evident in here. Nylon CF15 type specimens performed better than Nylon's, mainly due to fibers' effect on adhesion to Aluminium's adherend. For these specimens' failure, the load had to be greater than the required to break the interlayer adhesion between Nylon CF15's adherend and the same material's coating. This polymer choice and manufacturing technique indicate a satisfactory adhesion quality.

Figures 4.17 and 4.18 present ABS, Nylon and Nylon CF15 specimens previously abraded by grit-blasting. Figure 4.17 (a) illustrates ABS adherend's specimens, where as Figures 4.17 (b) and 4.18 present the Nylon and Nylon CF15's ones, respectively.

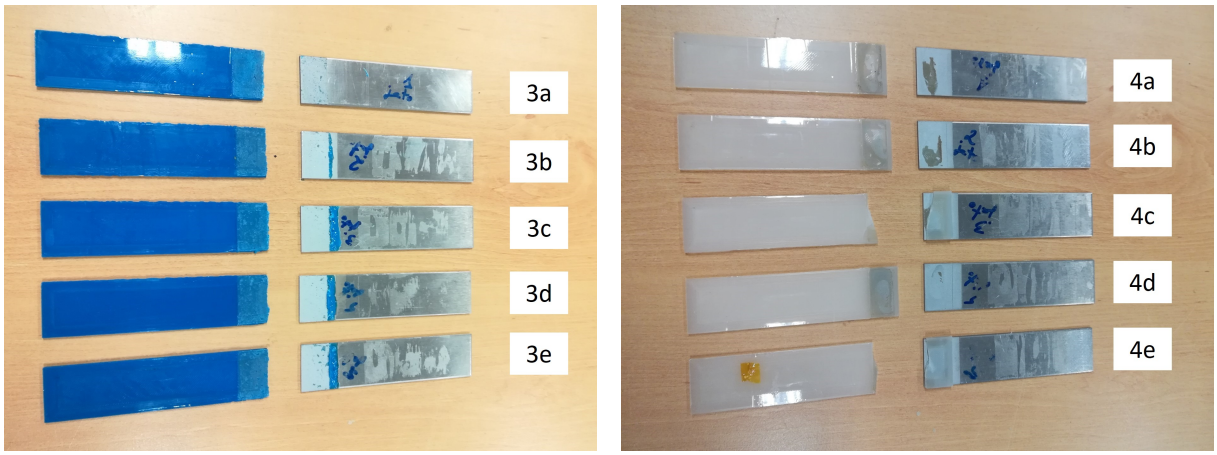

(a) (b)

Figure 4.17: Fracture's surface analysis of (a) Aluminium-ABS and (b) Aluminium-Nylon specimens previously abraded by grit-blasting.

ABS' type polymers show a characteristic adhesive failure mode, critical between ABS coating and Aluminium adherend, probably due to poor wetting of its surface. Comparing with mechanical tests, Specimen 3e was the one that exhibited the better grip between ABS and Aluminium, also explained when observing the fracture's surface of it, with little residues of ABS coating that remained interlocked with metal's surface.

Now looking at Nylon's specimens illustrated in Figure 4.17 (b), a comparison can be done about the results demonstrated by Specimens 4c and 4e in tensile loading tests and the failure mode presented in here. In fact, the maximum failure load was achieved for these. In here, a substrate failure mode is evident, which can be explained by a good adhesion between both adherends when increasing metal's surface roughness. The remelt of the polymer's coating enabled it to flow into Aluminium's surface cavities and enhance the mechanical interlocking between the two, as previously demonstrated in literature (Section 2.3). Specimens 4a and 4b show a mixed adhesive/cohesive failure mode, however pending to adhesive failure, with Specimen 4d showing a clear adhesive failure mode and, consequently, the specimen with the weaker adhesion bond. These observations correlate with the results found in tensile loading tests.

Figure 4.18 illustrates the last tested specimens, made from Nylon CF15 and Aluminium's adherends.

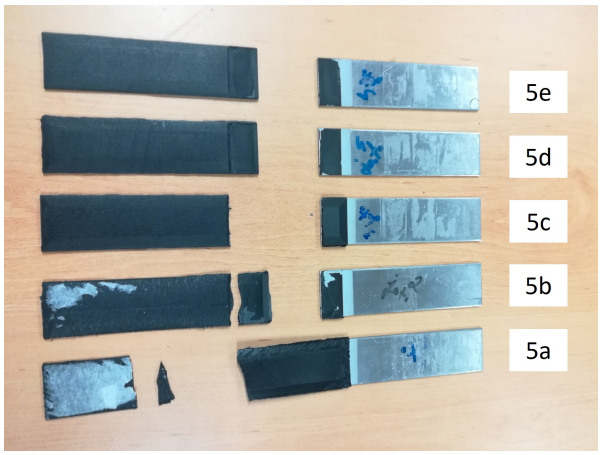

Figure 4.18: Fracture's surface analysis of Aluminium-Nylon CF15 specimens previously abraded by grit-blasting.

Analysing the fracture's surface only, Specimens 5a, 5b and 5c appear to demonstrate the better results in adhesion strength and quality of the joint. These three specimens exhibit a substrate failure mode, the most desired one when joining two substrates via an adhesive. However not in the same mode, Specimens 5d and 5e also exhibit good adhesion properties, failing cohesively. These results indicate a proper polymer's infiltration into Aluminium's cavities and consequent grip between both materials. The interlayer adhesion between the coating and polymer's adherend also indicate a satisfactory manufacturing technique (3D printing). When compared with tensile loading tests, Specimens 5b and 5c confirm the initial observational analysis, with the highest failure load values. However, the discrepancies between every specimen is very low compared with previous experiments, indicating a good adhesion technique when joining Nylon CF15 and Aluminium's substrates by FFF, for every specimen manufactured.

An example of each failure mode obtained in this experiment is illustrated in Figure 4.19, which exemplifies (a) an adhesive failure mode for Aluminium-ABS specimens, (b) a mixed adhesive/cohesive failure mode for Aluminium-Nylon specimens and (c) a substrate failure mode for Aluminium-Nylon CF15 specimens, all previously abraded by grit-blasting.

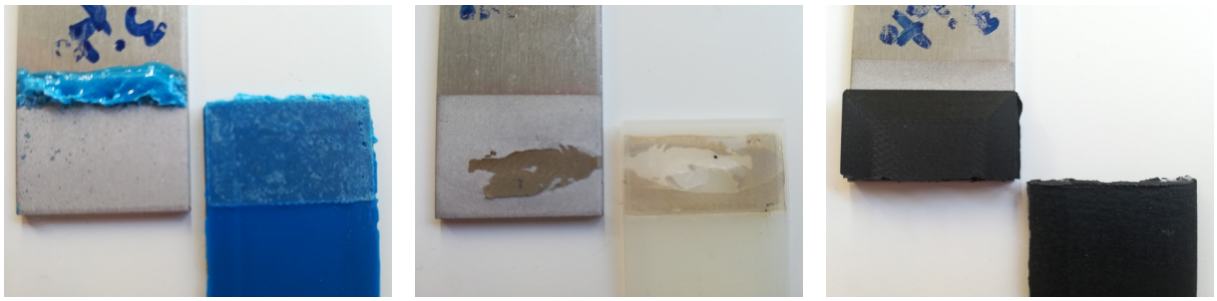

(a) (b) (c)

Figure 4.19: Illustration of each failure's mode: (a) adhesive failure mode, (b) mixed adhesive/cohesive failure mode and (c) substrate failure mode.

To sum up, Table 4.4 gathers all the relevant data determined in this work for each specimen type.

Table 4.4: Results' overview of most common failure mode for each type of joint.

Joint	**Abrasion Type**	$\mathbf{R_a}$ $[\mu\mathrm{m}]$	**ULSS** $[\mathrm{MPa}]$	**Failure Mode**
Al-ABS	SB	1.65 ± 0.46	1.18 ± 0.38	Adhesive
Al-Nylon	SP	0.32 ± 0.05	2.33 ± 0.57	Adhesive
Al-Nylon	SB	1.65 ± 0.46	3.14 ± 1.00	Cohesive/Substrate
Al-Nylon CF15	SP	0.32 ± 0.05	3.09 ± 0.30	Cohesive
Al-Nylon CF15	SB	1.65 ± 0.46	6.36 ± 0.43	Substrate

Chapter 5

Conclusions

This work laid hold of previous researches in polymer/metal adhesion mechanisms in FFF. It was studied the feasibility of adhesion among Aluminium and three polymeric substrates: ABS, Nylon and Nylon CF15. It has also been studied the effect of surface roughness and fibers content on the adhesion strength between each pair of material.

In here, FFF of single-lap joints made from Aluminium and each one of those enumerated polymers was validated and its adhesion strength measured. Advances in this subject could propel the utilization of FFF processes as the principal manufacturing technique for lighter components, such those applied in aeronautics' industry.

First, Aluminium's substrate was mechanically abraded up to three types of surface roughness' values: $0.16 \pm 0.04\ \mu m$, $0.32 \pm 0.05\ \mu m$ and $1.65 \pm 0.46\ \mu m$. Following procedures depended on polymer's choice. For ABS, a solution was manually applied on top of the Aluminium substrate, followed by a short curing time before ABS filament being deposited on top of that. For Nylon and Nylon CF15, primer's application was done by FFF, which was then remelted on top of a hot plate, a contemporary primer's fabrication process for these selected polymers. Besides the obvious difference in manufacturing's complexity and time span for each operation, further remarks are made about the effect that both primer's application and post-treatment might had on adhesion strength.

Noteworthy, the utilization of sandpaper for abrasion purposes has been extensively studied for many kinds of joints. However, its use in joints manufactured by FFF processes still lacks discussion. It was an interesting choice of abrasion technique for comparison with grit blasting's method results, which proved to be superior.

From the tests conducted and the results shown, it cannot be stated a theory of adhesion that completely explains the phenomenon of adhesion among the list of materials used in this work. However, an enhanced adhesion after abrading the surface of the Aluminium adherend is evident, which can be anticipated by mechanical interlocking theory, increased contact surface area and formation of a clean surface.

Furthermore, one can compare the primer's application method of ABS and Nylon's specimens and conclude on the adhesion improvement the last had. When applying it manually, as it was the case for ABS, the spreading of the polymer into Aluminium's surface cavities was less efficient than Nylon's. The higher temperatures of the nozzle and the contact force it exerted on Aluminium's surface might be the cause for this decrease in viscosity of Nylon's and a better adhesion promotion. Now, the effect that this method had in adhesion strength may be explained by the absorption theory, allied with the mechanical interlocking one. An original setup present in this work was the choice of primer's thickness for PMH

joints' manufacture. The value utilized was in accordance with previous researches about adhesive strength correlation with this variable. For this, the relevance of AM technology in primer's fabrication processes is shown again.

Nylon CF15's results indicate a probable dominance of mechanical interlocking theory explaining the adhesion strength demonstrated for this combination of materials. The enlargement of Aluminium's surface cavities, after grit-blasting treatment, might have enabled the anchoring of carbon fibers into Aluminium's surface valleys. This might had not been possible until this level of surface roughness was reached, due to fibers' dimensions. Previous researches had already studied the effect of anchoring by continuous fibers within AM context. The results obtained in this thesis demonstrate the suitability of milled fibers for PMH components fabricated by this technology. Milled carbon fibers might be a viable alternative for expensive continuous carbon filaments, as well as allowing a broader range of 3D machines' employment.

Although highly promising, the current manufacture technique still lacks the uniformity of classical adhesive application on single-lap joints. Operations such as remelting and removal of the component from the build plate are not optimized, which translates into a unsuitable procedure, an excessive time between each one and superior probability of failure.

Overall, this work validated a novel FFF technique for additional combination of materials, other than those previously studied. Nylon CF15 specimens exhibited the best mechanical properties, which reiterates the importance of fibers in adhesion mechanisms. Thermal post-treatment revealed extremely advantageous, an element that could be easily added to a standard FFF process, when looking for PMH component's fabrication.

Despite the work done and the conclusions mentioned above, the development of this thesis raised some questions that should be worked out in future work:

- To fully understand the failure mechanism for this type of joints manufactured by FFF, a thorough strain field analysis should be done. Also, to prevent stress concentration's locations, an adhesive fillet should be added to the end of the overlap area.

- The implementation described in this work for the removal of the printed specimens can be improved by creating a setup within the build plate that allows a stress-free removal procedure. In fact, current removal's technique might have a great impact on the disparity of results found for the weaker joints, due to the excessive force that was applied when the polymer notably adhered to the build plate's tape. More tests should be conducted to study the feasibility of experimenting other type of tape present in the market or even develop a new one more suitable for the task. Other than that, the customized build plate could also be altered to allow a removal piece under the polymeric top adherend. In this case, no force would be applied to the specimen and the joint part of the build plate could stay adhered to the polymeric top adherend and even be helpful for the alignment of the specimen during tensile loading tests.

- Additionally, current setup could also benefit from the introduction of a customized heating control system for the build plate, completely independent from the 3D printer. This device would avert the need for constant maneuvers of the printed specimens when remelting its primer and increased error probability or damage of the specimens.
- Furthermore, specimen's fractured surfaces should be thoroughly analysed, in order to evaluate the inclusions of carbon fibers within the Aluminium surface cavities. For future work, this might enlighten the theory of adhesion that better explains the phenomenon of adhesion among these combinations of materials and help coming up to a solution that would increase the tensile strength of PMH joints.

Bibliography

[1] European Commission. The European Green Deal. *European Commission*, 53(9):24, 2019. ISSN 1098-6596. doi: 10.1017/CBO9781107415324.004.

[2] E. Commission. A New Industrial Strategy for Europe. pages 1–16, 2020. URL `https://ec.europa.eu/info/sites/info/files/communication-eu-industrial-strategy-march-2020{_}en.pdf`.

[3] ISO/ASTM. Additive Manufacturing - General Principles Terminology (ASTM52900). *Rapid Manufacturing Association*, pages 10–12, 2013. ISSN 1882-675X. doi: 10.1520/F2792-12A.2.

[4] E. MacDonald and R. Wicker. Multiprocess 3D printing for increasing component functionality. *Science*, 353(6307), 2016. ISSN 10959203. doi: 10.1126/science.aaf2093.

[5] B. Berman. 3-D printing: The new industrial revolution. *Business Horizons*, 55(2):155–162, 2012. ISSN 00076813. doi: 10.1016/j.bushor.2011.11.003.

[6] G. C. Dumitrescu and I. A. Nase. 3D Printing – A New Industrial Revolution. *Knowledge Horizons. Economics*, 8(1):32–39, 2016. ISSN 2069-0932.

[7] Wohlers. Wohlers report 2020, 2020. ISBN 978-0-9913332-6-4.

[8] A. M. Lewis, J. C. Kelly, and G. A. Keoleian. Vehicle lightweighting vs. electrification: Life cycle energy and GHG emissions results for diverse powertrain vehicles. *Applied Energy*, 126:13–20, 2014. ISSN 03062619. doi: 10.1016/j.apenergy.2014.03.023.

[9] K. Martinsen, S. J. Hu, and B. E. Carlson. Joining of dissimilar materials. *CIRP Annals - Manufacturing Technology*, 64(2):679–699, 2015. ISSN 17260604. doi: 10.1016/j.cirp.2015.05.006.

[10] P. Kah, R. Suoranta, J. Martikainen, and C. Magnus. Techniques for joining dissimilar materials: Metals and polymers. *Reviews on Advanced Materials Science*, 36(2):152–164, 2014. ISSN 16058127.

[11] M. Vaezi, S. Chianrabutra, B. Mellor, and S. Yang. Multiple material additive manufacturing – part 1: A review. *Virtual and Physical Prototyping*, 8, 03 2013. doi: 10.1080/17452759.2013.778175.

[12] D. S. Gonzales and A. G. Alvarez. Additive Manufacturing Feasibility study and technology demonstration. *EDA AM State of the Art & Strategic Report*, pages 1–187, 2018.

[13] R. Falck, S. M. Goushegir, J. F. dos Santos, and S. T. Amancio-Filho. AddJoining: A novel additive manufacturing approach for layered metal-polymer hybrid structures. *Materials Letters*, 217:211–214, 2018. ISSN 18734979. doi: 10.1016/j.matlet.2018.01.021.

[14] F. P. W. Melchels, J. Feijen, and D. W. Grijpma. Biomaterials A review on stereolithography and its applications in biomedical engineering. *Biomaterials*, 31(24):6121–6130, 2010. ISSN 0142-9612. doi: 10.1016/j.biomaterials.2010.04.050.

[15] J. P. Kruth, X. Wang, T. Laoui, and L. Froyen. Lasers and materials in selective laser sintering. 23 (4):357–371, 2003.

[16] T. Gornet. History of additive manufacturing non-SL systems Introduction of low-cost 3D printers. pages 1–38, 2016.

[17] A. Savini, S. Member, and G. G. Savini. A Short History of 3D Printing , a Technological Revolution Just Started.

[18] P. Xu, J. Li, A. Meda, F. Osei-Yeboah, M. L. Peterson, M. Repka, and X. Zhan. Development of a quantitative method to evaluate the printability of filaments for fused deposition modeling 3D printing. *International Journal of Pharmaceutics*, 588(May):119760, 2020. ISSN 18733476. doi: 10.1016/j.ijpharm.2020.119760.

[19] DGH. Edition 2018. *Annuaire des statistiques des hydrocarbures en Côte d'Ivoire*, pages 1–40, 2018. URL `http://dghstatistiques.ci/assets/documents/annuaire/Annuaire-DGH-2018-v3.pdf`.

[20] K. V. Wong and A. Hernandez. A Review of Additive Manufacturing. *ISRN Mechanical Engineering*, 2012:1–10, 2012. ISSN 2090-5130. doi: 10.5402/2012/208760.

[21] M. Y. Zhou. STEP-based approach for direct slicing of CAD models for layered manufacturing. *International Journal of Production Research*, 43(15):3273–3285, 2005. ISSN 00207543. doi: 10.1080/00207540500097809.

[22] B. N. Turner, R. Strong, and S. A. Gold. A review of melt extrusion additive manufacturing processes: I. Process design and modeling. *Rapid Prototyping Journal*, 20(3):192–204, 2014. ISSN 13552546. doi: 10.1108/RPJ-01-2013-0012.

[23] A. Shrivastava. Introduction to Plastics Engineering. *Introduction to Plastics Engineering*, pages 1–16, 2018. doi: 10.1016/b978-0-323-39500-7.00001-0.

[24] W. K. Langford and T. Paper. ACHIEVING PRECISE FLOW IN FUSED DEPOSITION MODELING EXTRUDERS. 2012.

[25] B. N. Turner and S. A. Gold. A review of melt extrusion additive manufacturing processes : II . Materials , dimensional accuracy , and surface roughness. 3(December 2013):250–261, 2015. doi: 10.1108/RPJ-02-2013-0017.

[26] O. S. Carneiro, A. F. Silva, and R. Gomes. Fused deposition modeling with polypropylene. *Materials and Design*, 83:768–776, 2015. ISSN 18734197. doi: 10.1016/j.matdes.2015.06.053.

[27] J. Stringer, J. Jiang, J. Stringer, X. Xu, and R. Y. Zhong. Investigation of Printable Threshold Overhang Angle in Extrusion-based Additive Manufacturing for Reducing Support Waste International Journal of Computer Integrated Investigation of printable threshold overhang angle in extrusion-based additive manufacturing for reducing support waste. *International Journal of Computer Integrated Manufacturing*, 31(10):961–969, 2018. ISSN 0951-192X. doi: 10.1080/0951192X.2018.1466398.

[28] A. C. D. Bruijn, G. Gómez-gras, and M. A. Pérez. Jou rna lP pro of. *Polymer Testing*, page 106433, 2020. ISSN 0142-9418. doi: 10.1016/j.polymertesting.2020.106433.

[29] D. Espalin, J. A. Ramirez, F. Medina, and R. Wicker. exploring build process variations. 3(February 2013):236–244, 2014. doi: 10.1108/RPJ-12-2012-0112.

[30] F. Górski, W. Kuczko, R. Wichniarek, A. Dudziak, M. Kowalski, and P. Zawadzki. Choosing optimal rapid manufacturing process for thin-walled products using expert algorithm. 3(2):408–420, 2013. doi: 10.3926/jiem.2010.v3n2.p408-420.

[31] R. Anitha, S. Arunachalam, and P. Radhakrishnan. Critical parameters influencing the quality of prototypes in fused deposition modelling. 118:2–5, 2001.

[32] V. E. Kuznetsov, A. Solonin, O. D. Urzhumtsev, and R. Schilling. Strength of PLA Components Fabricated with Fused Deposition Technology Using a Desktop 3D Printer as a Function of Geometrical Parameters of the Process. (September), 2018. doi: 10.3390/polym10030313.

[33] Testing of Materials for Rapid Prototyping Fused Deposition Modelling Technology. 6(10):2082–2085, 2012.

[34] Q. Sun. Effect of processing conditions on the bonding quality of FDM polymer filaments. 2 (October 2007):72–80, 2008. doi: 10.1108/13552540810862028.

[35] A. Kumar, R. K. Ohdar, and S. S. Mahapatra. Improving dimensional accuracy of Fused Deposition Modelling processed part using grey Taguchi method. *Materials and Design*, 30(10):4243–4252, 2009. ISSN 0261-3069. doi: 10.1016/j.matdes.2009.04.030.

[36] R. V. Weeren, M. Agarwala, V. R. Jamalabad, and A. Bandyophadyay. Quality of Parts Processed by Fused Deposition. pages 314–321.

[37] R. Falck, J. F. dos Santos, and S. T. Amancio-Filho. Microstructure and mechanical performance of additively manufactured aluminum 2024-t3/acrylonitrile butadiene styrene hybrid joints using an addjoining technique. *Materials*, 16(6), 2019. ISSN 19961944. doi: 10.3390/ma12060864.

[38] M. K. Agarwala. Structural quality of parts processed by fused deposition. Rapid Prototyping Journal. pages 4–19, 1996.

[39] A. Dey and N. Yodo. A Systematic Survey of FDM Process Parameter Optimization and Their Influence on Part Characteristics. 2019.

[40] S. E. E. Profile. Mechanical properties of fused deposition modeling parts manufactured with ULTEM & z . ast ; 9085 MECHANICAL PROPERTIES OF FUSED DEPOSITION MODELING PARTS MANUFACTURED WITH ULTEM * 9085. (February), 2019.

[41] C. Bellehumeur and P. E. E-mail. Modeling of Bond Formation Between Polymer Filaments in the Fused Deposition Modeling Process. 2004.

[42] R. A. Mendelson. A Generalized Melt Viscosity-Temperature Dependence for Styrene and Styrene-Acrylonitrile Based Polymers. 16(10), 1976.

[43] N. Rosenzweig and M. Narkis. Sintering Rheology of Amorphous Polymers. 21(17):1167–1170, 1981.

[44] A. C. S. Davis, K. E. Hillgartner, H. Han, and J. E. Seppala. extrusion additive manufacturing †. *Additive Manufacturing*, 2017. ISSN 2214-8604. doi: 10.1016/j.addma.2017.06.006.

[45] A. Kumar, R. K. Ohdar, and S. S. Mahapatra. Parametric appraisal of mechanical property of fused deposition modelling processed parts. *Materials and Design*, 31(1):287–295, 2010. ISSN 0261-3069. doi: 10.1016/j.matdes.2009.06.016.

[46] W. Wu, P. Geng, G. Li, D. Zhao, H. Zhang, and J. Zhao. Influence of Layer Thickness and Raster Angle on the Mechanical Properties of 3D-Printed PEEK and a Comparative Mechanical Study between PEEK and ABS. pages 5834–5846, 2015. doi: 10.3390/ma8095271.

[47] M. Montero, S. Roundy, D. Odell, S.-h. Ahn, and P. K. Wright. Material Characterization of Fused Deposition Modeling (FDM) ABS by Designed Experiments. pages 1–21.

[48] S. H. Ahn, C. Baek, S. Lee, and I. S. Ahn. Anisotropic tensile failure model of rapid prototyping parts - Fused Deposition Modeling (FDM). *International Journal of Modern Physics B*, 17(8-9 I): 1510–1516, 2003. ISSN 02179792. doi: 10.1142/s0217979203019241.

[49] A. W. Fatimatuzahraa, B. Farahaina, and W. A. Y. Yusoff. The effect of employing different raster orientations on the mechanical properties and microstructure of Fused Deposition Modeling parts. pages 22–27, 2011.

[50] A. W. Gebisa and H. G. Lemu. Investigating Effects of Fused-Deposition Modeling (FDM) Processing Parameters on Flexural Properties of ULTEM 9085 using Designed Experiment. pages 1–23, 2018. doi: 10.3390/ma11040500.

[51] O. A. Mohamed, S. H. Masood, and J. L. Bhowmik. Experimental investigation of creep deformation of part processed by fused deposition modeling using definitive screening design. *Additive Manufacturing*, 18:164–170, 2017. ISSN 22148604. doi: 10.1016/j.addma.2017.10.013.

[52] D. Płaczek. Adhesion between the bed and component manufactured in FDM technology using selected types of intermediary materials. 2:1–9, 2019.

[53] X. Peng, M. Zhang, Z. Guo, L. Sang, and W. Hou. Investigation of processing parameters on tensile performance for FDM-printed carbon fiber reinforced polyamide 6 composites. *Composites Communications*, 22(September):100478, 2020. ISSN 2452-2139. doi: 10.1016/j.coco.2020.100478.

[54] A. Allison and R. Scudamore. Joining Sub-Platform SRA. 2014.

[55] R. Sankaranarayanan and N. R. J. Hynes. Prospects of Joining Multi-Material Structures. 130021: 10–15, 2018. doi: 10.1063/1.5033165.

[56] S. H. Zhang, Z. R. Wang, Z. T. Wang, Y. Xu, and K. B. Chen. Some new features in the development of metal forming technology. 151:39–47, 2004. doi: 10.1016/j.jmatprotec.2004.04.098.

[57] M. Haghshenas and A. P. Gerlich. Engineering Science and Technology , an International Journal Joining of automotive sheet materials by friction-based welding methods : A review. *Engineering Science and Technology, an International Journal*, 2018. ISSN 2215-0986. doi: 10.1016/j.jestch.2018.02.008.

[58] H. Wargnier, F. X. Kromm, M. Danis, and Y. Brechet. Proposal for a multi-material design procedure. *JOURNAL OF MATERIALS&DESIGN*, 56:44–49, 2014. ISSN 0261-3069. doi: 10.1016/j.matdes.2013.11.004. URL `http://dx.doi.org/10.1016/j.matdes.2013.11.004`.

[59] H. Shim, E. A. Mccullough, and B. W. Jones. Textile Research Journal. 2001. doi: 10.1177/004051750107100605.

[60] J. Pflug. Sandwich Materials Selection Charts. (September), 2006. doi: 10.1177/1099636206065521.

[61] G. N. Levy and R. Schindel. MANUFACTURING TECHNOLOGIES, STATE OF THE ART AND FUTURE. 2(Lm).

[62] M. Bahraminasab, B. B. Sahari, K. L. Edwards, F. Farahmand, T. Sai, M. Arumugam, and A. Jahan. Multi-objective design optimization of functionally graded material for the femoral component of a total knee replacement. *JOURNAL OF MATERIALS&DESIGN*, 53:159–173, 2014. ISSN 0261-3069. doi: 10.1016/j.matdes.2013.06.050.

[63] C. Magnus. Feasibility study of metal to polymer hybrid joining. 2012.

[64] A. Baldan. Adhesively-bonded joints and repairs in metallic alloys, polymers and composite materials: Adhesives, adhesion theories and surface pretreatment, jan 2004. ISSN 00222461.

[65] A. Society. *3 Plastic Properties and Testing 3.1*. 2018. ISBN 9780323395007. doi: 10.1016/B978-0-323-39500-7.00003-4.

[66] W. Brockmann. Adhesive Bonding as a Joining Technique. pages 1–4, 2009.

[67] C. Weimer. Composites in aerospace - future challenges, needs and opportunities. *Proceedings of the Institute for Carbon Composites symposium*, 2014.

[68] Y. Suzuki. Adhesive bonding for railway application. *Handbook of Adhesion Technology: Second Edition*, 2-2:1367–1390, 2018. doi: 10.1007/978-3-319-55411-2_47.

[69] T. Nishihara. *Automotive Industry*, volume 31. 1989. ISBN 9783319554112. doi: 10.1539/joh1959.31.533.

[70] C. Creton. 15 Materials Science of Pressure-Sensitive Adhesives.

[71] B. Duncan and L. Crocker. Project MMS8 Report No1 Review of Tests for Adhesion Strength. (December), 2001.

[72] J. Comyn. Chapter 1 Theories of adhesion. *Handbook of Adhesives and Sealants*, 2(BSc 1964): 1–50, 2006. ISSN 18745695. doi: 10.1016/S1874-5695(06)80012-6.

[73] A. Al-kawaz. Theories of Adhesion.

[74] D. Bonn, J. Eggers, J. Indekeu, and J. Meunier. Wetting and spreading. *Reviews of Modern Physics*, 81(2):739–805, 2009. ISSN 15390756. doi: 10.1103/RevModPhys.81.739.

[75] M. Dawood. *Durability of steel components strengthened with fiber-reinforced polymer (FRP) composites*. Woodhead Publishing Limited, 2014. ISBN 9780857096531. doi: 10.1533/9780857096654.1.96.

[76] E. M. Petrie. *Adhesive bonding of textiles: Principles, types of adhesive and methods of use*. 2013. ISBN 9781845696276. doi: 10.1533/9780857093967.2.225.

[77] K. K. Chawla. *Composite Materials*. ISBN 9780387743646.

[78] C. Core. The interface region. (May 2018).

[79] S. A. Nenakhov. Basic Terms and Definitions in Adhesion. 1(1):19–22, 2008. doi: 10.1134/S1995421208010085.

[80] S. Ebnesajjad. Theories of Adhesion. pages 77–91, 2014. doi: 10.1016/B978-0-323-26435-8.00005-8.

[81] I. Journal, M. Sciences, and W. John. Surface Activation of High Impact Polystyrene Substrate Using Dynamic Atmospheric Pressure Plasma. (August), 2019. doi: 10.21791/IJEMS.2019.1.11. Surface.

[82] T. Young. An essay on the cohesion of fluids. 1804.

[83] A. W. Neumann and R. Good. Techniques of Measuring Contact Angles. 1979.

[84] R. S. Hebbar, A. M. Isloor, and A. F. Ismail. *Chapter 12 - Contact Angle Measurements*. Elsevier B.V., 2017. ISBN 9780444637765. doi: 10.1016/B978-0-444-63776-5.00012-7.

[85] B. V. Derjaguin and V. P. Smilga. Electronic Theory of Adhesion Theory of adhesion : Role of surface roughness Theory of Adhesion of Small Particles. 4609(1967), 2014. doi: 10.1063/1.1709192.

[86] W. Possart. Experimental and theoretical description of the electrostatic component of adhesion at polymer / metal contacts. 8(2):77–83, 1988.

[87] D. A. Hays. Role of Electrostatics in Adhesion. pages 249–278, 1991.

[88] H. Search, C. Journals, A. Contact, M. Iopscience, and I. P. Address. Surface charge contribution in rubber adhesion and friction. 1801, 1801.

[89] A. Ghanem and Y. Lang. Introduction to polymer adhesion. (August), 2017.

[90] A. R. Ã. Hutchinson and S. Iglauer. Adhesion of construction sealants to polymer foam backer rod used in building construction. 26:555–566, 2006. doi: 10.1016/j.ijadhadh.2005.09.001.

[91] F. Awaja, M. Gilbert, G. Kelly, B. Fox, and P. J. Pigram. Progress in Polymer Science Adhesion of polymers. 34:948–968, 2009. doi: 10.1016/j.progpolymsci.2009.04.007.

[92] W. Abbey. Review The science of adhesion. 15:2141–2166.

[93] A. Baldan. International Journal of Adhesion & Adhesives Adhesion phenomena in bonded joints. *International Journal of Adhesion and Adhesives*, 38:95–116, 2012. ISSN 0143-7496. doi: 10.1016/j.ijadhadh.2012.04.007.

[94] A. J. Kinloch. *Adhesion and Adhesives*. 1987. ISBN 9789048140039.

[95] J. W. McBain and D. G. Hopkins. ADHESIVES AND ADHESIVE ACTION. 1924.

[96] G. Fourche and P. France. An Overview of the Basic Aspects of Polymer Adhesion . Part I : Fundamentals. 35(12), 1995.

[97] H. Wang. Improving the Adhesion of Polyethylene by UV Grafting. (October 2014):37–41, 2007. doi: 10.1080/00218460600775815.

[98] H. T. D. C. Martin. Microstructural studies of interfacial deformation in painted thermoplastic polyolefins (TPOs). 7:4783–4791, 2002.

[99] B. M. C. V. D. Leeden and G. Frens. Surface Properties of Plastic Materials in Relation to Their Adhering Performance. (5):280–289, 2002.

[100] E. Maeva, I. Severina, S. Bondarenko, B. O. Neill, F. Severin, and R. G. Maev. REVIEW / SYNTHÈSE Acoustical methods for the investigation of adhesively bonded structures : A review. 1025:981–1025, 2004. doi: 10.1139/P04-056.

[101] S. S. Voyutskii and V. L. Vakula. The role of diffusion phenomena in polymer-to-polymer adhesion. *Journal of Applied Polymer Science*, 7(2):475–491, 1963. ISSN 10974628. doi: 10.1002/app.1963.070070207.

[102] J. J. Bikerman. Causes of Poor Adhesion: Weak Boundary Layers. *Industrial & Engineering Chemistry*, 59(9):40–44, 1967. ISSN 0019-7866. doi: 10.1021/ie51403a010.

[103] R. E. Robertson. The Strength of an Adhesive Weak Boundary Layer. *The Journal of Adhesion*, 7(2):121–136, 1975. ISSN 15455823. doi: 10.1080/00218467508075044.

[104] D. M. Brewis. Adhesion to polymers: how important are weak boundary layers? *International Journal of Adhesion and Adhesives*, 13(4):251–256, 1993. ISSN 01437496. doi: 10.1016/0143-7496(93)90028-8.

[105] S. Yang, L. Gu, and R. F. Gibson. Nondestructive detection of weak joints in adhesively bonded composite structures. *Composite Structures*, 51(1):63–71, 2001. ISSN 02638223. doi: 10.1016/S0263-8223(00)00125-2.

[106] C. O. Putman and U. K. Vaidya. Interfacial shear strength in a metal-thermoplastic composite. *Polymers and Polymer Composites*, 18(7):369–380, 2010. ISSN 14782391. doi: 10.1177/096739111001800703.

[107] J. Li, L. Xia, P. Li, Y. Zhu, Y. Sun, and D. Zuo. Relationship between coefficient of friction and surface roughness of wafer in nanomachining process. *Fourth International Conference on Smart Materials and Nanotechnology in Engineering*, 8793:87931Y, 2013. ISSN 0277786X. doi: 10.1117/12.2027965.

[108] C. Ochoa-Putman and U. K. Vaidya. Composites : Part A Mechanisms of interfacial adhesion in metal – polymer composites – Effect of chemical treatment. *Composites Part A*, 42(8):906–915, 2011. ISSN 1359-835X. doi: 10.1016/j.compositesa.2011.03.019.

[109] Y. H. Chueh, C. Wei, X. Zhang, and L. Li. Integrated laser-based powder bed fusion and fused filament fabrication for three-dimensional printing of hybrid metal/polymer objects. *Additive Manufacturing*, 31(November 2019):100928, 2020. ISSN 22148604. doi: 10.1016/j.addma.2019.100928.

[110] D. E. Packham. Surface energy, surface topography and adhesion. *International Journal of Adhesion and Adhesives*, 23(6):437–448, jan 2003. ISSN 01437496. doi: 10.1016/S0143-7496(03)00068-X.

[111] M. S. Islam, L. Tong, and P. J. Falzon. Influence of metal surface preparation on its surface profile, contact angle, surface energy and adhesion with glass fibre prepreg. *International Journal of Adhesion and Adhesives*, 51:32–41, jun 2014. ISSN 01437496. doi: 10.1016/j.ijadhadh.2014.02.006.

[112] A. F. Harris and A. Beevers. Effects of grit-blasting on surface properties for adhesion. *International Journal of Adhesion and Adhesives*, 19(6):445–452, dec 1999. ISSN 01437496. doi: 10.1016/S0143-7496(98)00061-X.

[113] S. Ebnesajjad. *Material surface preparation techniques*. Elsevier Inc., 2011. ISBN 9781437744613. doi: 10.1016/B978-1-4377-4461-3.10005-7.

[114] E. M. Petrie. Hanbook of Adhesives and Sealants.

[115] A. Objois and Y. Gilibert. Theoretical and Experimental Analysis of the Scarf Joint Bonded Structure : Influence of the Adhesive Thickness on the Micro-mechanical Behavior. (January 2015):37–41. doi: 10.1080/00218469908010485.

[116] J. Cham, B. Pruitt, M. Cutkosky, M. Binnard, L. E. Weiss, and G. Neplotnik. Layered manufacturing with embedded components: process planning considerations, 1999.

[117] S. Fafenrot, N. Grimmelsmann, M. Wortmann, and A. Ehrmann. Three-dimensional (3D) printing of polymer-metal hybrid materials by fused deposition modeling. *Materials*, 10(10), 2017. ISSN 19961944. doi: 10.3390/ma10101199.

[118] M. Mieszala, M. Hasegawa, G. Guillonneau, J. Bauer, R. Raghavan, C. Frantz, O. Kraft, S. Mischler, J. Michler, and L. Philippe. Micromechanics of Amorphous Metal/Polymer Hybrid Structures with 3D Cellular Architectures: Size Effects, Buckling Behavior, and Energy Absorption Capability. *Small*, 13(8):1–13, 2017. ISSN 16136829. doi: 10.1002/smll.201602514.

[119] G. Lucchetta, F. Marinello, and P. F. Bariani. Aluminum sheet surface roughness correlation with adhesion in polymer metal hybrid overmolding Aluminum sheet surface roughness correlation with adhesion in polymer metal hybrid overmolding. (October 2017), 2011. doi: 10.1016/j.cirp.2011.03.073.

[120] N. G. Barbosa, R. D. Campilho, F. J. Silva, and R. D. Moreira. Comparison of different adhesively-bonded joint types for mechanical structures. *Applied Adhesion Science*, 6(1):1–19, 2018. ISSN 21964351. doi: 10.1186/s40563-018-0116-1.

[121] A. Çaik. Effect of adherend shape on stress concentration reduction of adhesively bonded single lap joint. *Engineering Review*, 36(1):29–34, 2016. ISSN 13309587.

[122] J. Ahn, S. Stapleton, and A. Waas. *Advanced modeling of the behavior of bonded composite joints in aerospace applications*. Woodhead Publishing Limited, 2011. doi: 10.1533/9780857094926.2.423.

[123] H. Özer. Introductory Chapter : Structural Adhesive Bonded Joints Joints. doi: 10.5772/intechopen.74229.

[124] F. M. Lucas, J. C. Paulo, R. D. Adams, and J. K. Spelt. International Journal of Adhesion & Adhesives Analytical models of adhesively bonded joints — Part I : Literature survey. 29:319–330, 2009. doi: 10.1016/j.ijadhadh.2008.06.005.

[125] O. Volkersen. Die nietkraftverteilung in zugbeanspruchten nietverbindungen mit konstanten laschenquerschnitten. *Luftfahrtfor schung*, 15:41–47, 1938. URL `https://ci.nii.ac.jp/naid/20000179510/en/`.

[126] M. Goland and E. Reissner. *Journal of Applied Mechanics*, 66:A17, 1944.

[127] R. M. Jones. Mechanics Of Composite Materials, 1998.

[128] I. M. Daniel and O. Ishai. *ENGINEERING MECHANICS OF COMPOSITE MATERIALS*. 2006. ISBN 9780195150971.

[129] Adhesive Bonding and integrally Cocured Structure : A Way to Reduce Assembly Costs through Parts integration. doi: 10.1016/B978-1-85617-415-2.50009-5.

[130] ASTM. ASTM D3163-01 Standard Test Method for Determining Strength of Adhesively Bonded Rigid Plastic Lap-Shear Joints in Shear by Tension Loading. 15(May):2–4, 2001.

[131] S. Olivera, H. B. Muralidhara, K. Venkatesh, K. Gopalakrishna, and C. S. Vivek. Plating on acrylonitrile–butadiene–styrene (abs) plastic: a review. *Journal of Materials Science*, 51:3657–3674, 4 2016. ISSN 15734803. doi: 10.1007/s10853-015-9668-7.

[132] J. R. Arnold. Plating & Surface Finishing. 2004.

[133] M. Sardinha, C. M. S. Vicente, N. Frutuoso, R. Ribeiro, L. Reis, and M. Leite. Effect of the ironing process on ABS parts produced by FDM. (January):1–7, 2020. doi: 10.1002/mdp2.151.

[134] O. L. A. Cle. A model research for prototype warp deformation in the FDM process. pages 1087–1096, 2007. doi: 10.1007/s00170-006-0556-9.

[135] Abs properties, March 2020. https://dielectricmfg.com/knowledge-base/abs/.

[136] M. Dawoud, I. Taha, and S. J. Ebeid. Mechanical behaviour of ABS: An experimental study using FDM and injection moulding techniques. *Journal of Manufacturing Processes*, 21:39–45, 2016. ISSN 15266125. doi: 10.1016/j.jmapro.2015.11.002.

[137] J. Cantrell, S. Rohde, D. Damiani, R. Gurnani, L. Di Sandro, J. Anton, A. Young, A. Jerez, D. Steinbach, C. Kroese, and P. Ifju. Experimental characterization of the mechanical properties of 3D printed ABS and polycarbonate parts. *Conference Proceedings of the Society for Experimental Mechanics Series*, 3:89–105, 2017. ISSN 21915652. doi: 10.1007/978-3-319-41600-7_11.

[138] E. C. Botelho, J. C. Bravim Júnior, M. L. Costa, and M. C. M. de Faria. Environmental effects on thermal properties of PEI/Glass fiber composite materials. *Journal of Aerospace Technology and Management*, 5(2):241–254, 2013. ISSN 21759146. doi: 10.5028/jatm.v5i2.193.

[139] M. Gilbert. *Aliphatic Polyamides*, pages 487–511. Elsevier Inc., 2017. ISBN 9780323358248. doi: 10.1016/B978-0-323-35824-8.00018-9.

[140] Material Datasheet Composites. URL `http://static.markforged.com/downloads/composites-data-sheet.pdf`.

[141] Nylon CF15 Carbon 3D printing guide. URL `http://www.fillamentumautomotive.com/wp-content/uploads/2020/10/FI_Printing_Guide_Nylon_CF15_Carbon.pdf`.

[142] M. Spoerk, J. Gonzalez-Gutierrez, J. Sapkota, S. Schuschnigg, and C. Holzer. Effect of the printing bed temperature on the adhesion of parts produced by fused filament fabrication. *Plastics, Rubber and Composites*, 47(1):17–24, 2018. ISSN 17432898. doi: 10.1080/14658011.2017.1399531.

[143] Kapton Tape Data Sheet. URL `https://www.emsdiasum.com/microscopy/technical/datasheet/77708.aspx`.

[144] A. Ghumatkar, S. Budhe, R. Sekhar, M. D. Banea, and S. De Barros. Influence of adherend surface roughness on the adhesive bond strength. *Latin American Journal of Solids and Structures*, 13 (13):2356–2370, 2016. ISSN 16797825. doi: 10.1590/1679-78253066.

[145] Scotch Masking Tape 2800 Blue. 2019. URL `https://3m.citrination.com/pif/000814?locale=en-US`.

[146] ASTM E8. ASTM E8/E8M standard test methods for tension testing of metallic materials 1. *Annual Book of ASTM Standards 4*, (C):1–27, 2010. doi: 10.1520/E0008.

[147] ASTM Standard. Standard Test Method for Microindentation Hardness of Materials. *ASTM International*, E384:1–40, 2017. doi: 10.1520/E0384-17.

[148] Eurocode 9: Design of aluminium structures. General structural rules, 2007. ISBN: 978 0 580 86081 2.

[149] Y. Boutar, S. Naïmi, S. Mezlini, and M. B. S. Ali. Effect of surface treatment on the shear strength of aluminium adhesive single-lap joints for automotive applications. *International Journal of Adhesion and Adhesives*, 67(June 2018):38–43, 2016. ISSN 01437496. doi: 10.1016/j.ijadhadh.2015.12.023.

Appendix A

Technical Drawings

Seção A-A

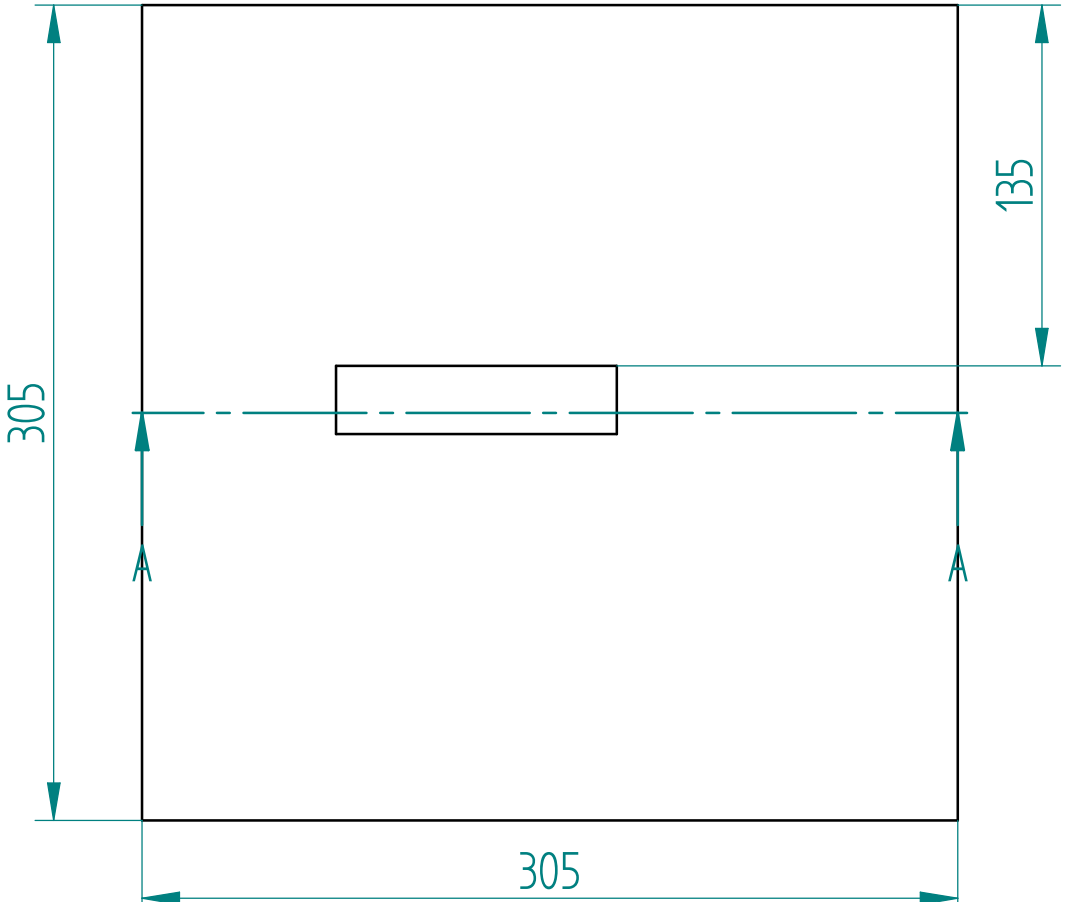

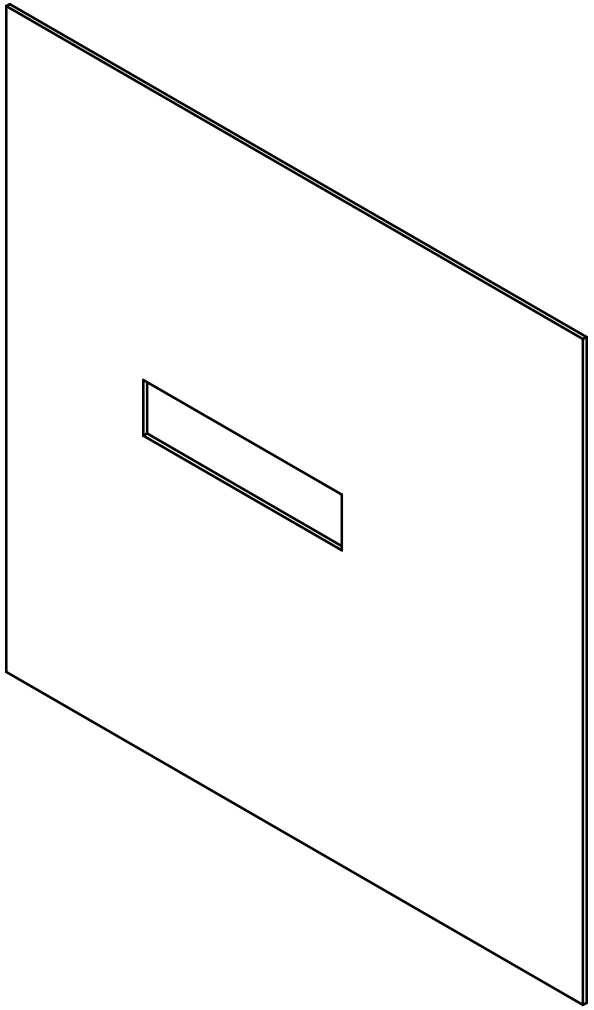

	NAME	DATE
DRAWN	Guilherme	20/07/2021
CHECKED		
ENG APPR		
MGR APPR		

Finishing: P120 Sandpaper

Instituto Superior Técnico

TITLE

Name: Guilherme Martins
Nr.: 80786

SIZE	DWG NO	REV
A3	Thesis 1	0

Customized Build Plate

SCALE: 1:2	WEIGHT:	SHEET 1 OF 1

Appendix B

Single-Lap Joints' Mechanical Analysis

Table B.1: Single-Lap Joints' mechanical analysis.

Specimen ID	**ULSS** $[\mathbf{MPa}]$
1a	2.45
1b	2.15
1c	3.02
1d	1.33
1e	2.69
Average	2.33 ± 0.57
2a	0.40
2b	3.51
2c	2.87
2d	0.60
2e	2.88
Average	3.09 ± 0.30
3a	1.01
3b	0.95
3c	0.90
3d	1.11
3e	1.92
Average	1.18 ± 0.38
4a	3.11
4b	2.42
4c	4.34
4d	1.69
4e	4.14
Average	3.14 ± 1.00
5a	6.12
5b	6.37
5c	7.10
5d	5.78
5e	6.41
Average	6.36 ± 0.43